Constraining the Evolution of Cataclysmic Variables via the Masses and Accretion Rates of their Underlying White Dwarfs

A. F. Pala[1,2]★, B. T. Gänsicke[3], D. Belloni[4], S. G. Parsons[5], T. R. Marsh[3], M. R. Schreiber[6,7],
E. Breedt[8], C. Knigge[9], E. M. Sion[10], P. Szkody[11], D. Townsley[12], L. Bildsten[13,14], D. Boyd[15],
M. J. Cook[16,17], D. De Martino[18], P. Godon[10], S. Kafka[16], V. Kouprianov[19], K. S. Long[20,21],
B. Monard[22], G. Myers[16], P. Nelson[16], D. Nogami[23], A. Oksanen[24], R. Pickard[25], G. Poyner[25],
D. E. Reichart[19], D. Rodriguez Perez[16], J. Shears[25], R. Stubbings[16] and O. Toloza[6]

[1]*European Space Agency, European Space Astronomy Centre, Camino Bajo del Castillo s/n, 28692 Villanueva de la Cañada, Madrid, Spain*
[2]*European Southern Observatory, Karl Schwarzschild Straße 2, Garching, 85748, Germany*
[3]*Department of Physics, University of Warwick, Coventry, CV4 7AL, UK*
[4]*National Institute for Space Research, Av. dos Astronautas, 1758, 12227-010 São José dos Campos, SP, Brazil*
[5]*Department of Physics and Astronomy, University of Sheffield, Sheffield S3 7RH, UK*
[6]*Departamento de Física, Universidad Técnica Federico Santa María, A. España 1680, Valparaíso, Chile*
[7]*Instituto de Física y Astronomía, Millennium Nucleus for Planet Formation (NPF), Universidad de Valparaíso, 2360102 Valparaíso, Chile*
[8]*Institute of Astronomy, University of Cambridge, Cambridge, CB3 0HA, UK*
[9]*School of Physics and Astronomy, University of Southampton, Southampton, SO17 1BJ, UK*
[10]*Astronomy & Astrophysics, Villanova University, Villanova, PA 19085, USA*
[11]*Department of Astronomy, University of Washington, Seattle, WA 98195–1580, USA*
[12]*Department of Physics and Astronomy, University of Alabama, Tuscaloosa, AL 35405, USA*
[13]*Department of Physics, University of California, Santa Barbara, CA 93106, USA*
[14]*Kavli Institute for Theoretical Physics, University of California, Santa Barbara, CA 93106, USA*
[15]*British Astronomical Association, Variable Star Section, West Challow Observatory, OX12 9TX, UK*
[16]*American Association of Variable Star Observers, Cambridge, MA 02138, USA*
[17]*Newcastle Observatory, Newcastle, Ontario, Canada*
[18]*INAF - Osservatorio Astronomico di Capodimonte, Napoli, I–80131, Italy*
[19]*Department of Physics and Astronomy, University of North Carolina at Chapel Hill, Chapel Hill, NC 27599-3255*
[20]*Space Telescope Science Institute, 3700 San Martin Drive, Baltimore, MD 21218, USA*
[21]*Eureka Scientific, Inc. 2452 Delmer Street, Suite 100, Oakland, CA 94602–3017, USA*
[22]*CBA Kleinkaroo, Calitzdorp, South Africa*
[23]*Department of Astronomy, Graduate School of Science, Kyoto University, Oiwakecho, Kitashirakawa, Sakyo-ku, Kyoto 606-8502, Japan*
[24]*Hankasalmi observatory, Verkkoniementie 30, 40950 Muurame, Finland*
[25]*British Astronomical Association, Variable Star Section, Burlington House, Piccadilly, London, W1J 0DU, UK*

ABSTRACT

We report on the masses (M_{WD}), effective temperatures (T_{eff}) and secular mean accretion rates ($\langle \dot{M} \rangle$) of 43 cataclysmic variable (CV) white dwarfs, 42 of which were obtained from the combined analysis of their *Hubble Space Telescope* ultraviolet data with the parallaxes provided by the Early Third Data Release of the *Gaia* space mission, and one from the white dwarf gravitational redshift. Our results double the number of CV white dwarfs with an accurate mass measurement, bringing the total census to 89 systems. From the study of the mass distribution, we derive $\langle M_{WD} \rangle = 0.81^{+0.16}_{-0.20} \, M_\odot$, in perfect agreement with previous results, and find no evidence of any evolution of the mass with orbital period. Moreover, we identify five systems with $M_{WD} < 0.5 M_\odot$, which are most likely representative of helium-core white dwarfs, showing that these CVs are present in the overall population. We reveal the presence of an anti-correlation between the average accretion rates and the white dwarf masses for the systems below the $2-3$ h period gap. Since $\langle \dot{M} \rangle$ reflects the rate of system angular momentum loss, this correlation suggests the presence of an additional mechanism of angular momentum loss that is more efficient at low white dwarf masses. This is the fundamental concept of the recently proposed empirical prescription of consequential angular momentum loss (eCAML) and our results provide observational support for it, although we also highlight how its current recipe needs to be refined to better reproduce the observed scatter in T_{eff} and $\langle \dot{M} \rangle$, and the presence of helium-core white dwarfs.

Key words: stars: white dwarfs – cataclysmic variables – evolution – fundamental parameters

★ E-mail: anna.pala@esa.int

1 INTRODUCTION

Cataclysmic variables (CVs) are compact interacting binaries in which a white dwarf is accreting mass from a low-mass star via Roche lobe overflow (e.g. Warner 1995). CVs descend from main-sequence binaries in which the more massive star (the primary) evolves first and leaves the main sequence. Following its expansion, the primary star fills its Roche lobe and starts unstable mass transfer on its less massive companion (the secondary), leading to the formation of a common envelope, i.e. a shared photosphere engulfing both stars (e.g. Paczynski 1976; Ivanova et al. 2013). The two stars transfer orbital energy to the envelope, which is rapidly expelled, leaving behind a post common envelope binary composed of the core of the giant primary, which evolves into a white dwarf, and a low-mass secondary star. Owing to subsequent orbital angular momentum losses, mainly via magnetic braking (which arises from a stellar wind associated with the magnetic activity of the secondary, e.g. Mestel 1968; Verbunt & Zwaan 1981) and gravitational wave radiation (e.g. Paczyński 1967), the post common envelope binary evolves into a semi-detached configuration, becoming a CV.

During the CV phase, the white dwarf response to the mass accretion process is the subject of a long-standing debate. Many binary population studies predict an average mass of CV white dwarfs of $\langle M_{WD} \rangle \simeq 0.5\,M_{\odot}$ (e.g. de Kool 1992; Politano 1996), which is lower than that of single white dwarfs ($\langle M_{WD} \rangle \simeq 0.6\,M_{\odot}$, Koester et al. 1979; Liebert et al. 2005; Kepler et al. 2007). This is because it is expected that the core growth of the primary is halted by the onset of the common envelope phase. Moreover, once a CV is formed, the material piled up at the white dwarf surface is compressed by the strong gravitational field of the star, leading periodically (typically on time-scale of ten/hundred thousands of years) to the occurrence of classical nova eruptions. These are the result of the thermonuclear ignition of the accreted material on the white dwarf surface and, during these explosions, different theoretical models predict that the accreted material (e.g. Yaron et al. 2005) and part of the underlying core of the white dwarf (Gehrz et al. 1998; Epelstain et al. 2007) should be ejected in the surrounding space, thus preventing the white dwarf from growing in mass. However, white dwarfs in CVs have been found to be significantly more massive than binary population models predicted (e.g. de Kool 1992; Politano 1996), with early work showing the average mass of CV white dwarfs to lie in the range $\langle M_{WD} \rangle \simeq 0.8 - 1.2\,M_{\odot}$ (Warner 1973; Ritter 1987). This result was originally interpreted as an observational bias because (i) the higher the mass of the white dwarf, the larger the accretion energy released per accreted unit mass, and (ii) for a fixed donor mass, more massive white dwarfs have larger Roche lobes that can accommodate larger, and hence brighter (especially at optically wavelengths) accretion discs. Therefore, CVs hosting massive white dwarfs were expected to be more easily discovered in magnitude limited samples (Ritter & Burkert 1986). Later on, Zorotovic et al. (2011) reviewed the masses of CV white dwarfs available in the literature, showing that the average mass of CV white dwarfs is $\langle M_{WD} \rangle = 0.83 \pm 0.23\,M_{\odot}$. Using the large and homogeneous sample of systems (Szkody et al. 2011, and references therein) discovered by the Sloan Digital Sky Survey (SDSS, York et al. 2000), the authors also demonstrated that there is a clear trend in disfavouring the detection of massive white dwarfs (which are smaller and less luminous than low mass white dwarfs for the same T_{eff}) and therefore the high average mass of CV white dwarfs cannot be ascribed to an observational bias.

Following this result, several authors investigated the possibility that CV white dwarfs could efficiently retain the accreted material and grow in mass, either by ejecting less material than they accrete, via

quasi-steady helium burning after several nova cycles (Hillman et al. 2016), or through a phase of thermal time-scale mass transfer during the pre-CV phase (Schenker et al. 2002). Wijnen et al. (2015) argued that mass growth during nova cycles cannot reproduce the observed distribution. In addition, these authors found that, even though the white dwarf mass could increase during thermal time-scale mass transfer, the resulting CV population would harbour a much higher fraction of nuclear evolved donor stars than observed, and thus they concluded that mass growth does not seem to be the reason behind the high masses of CV white dwarfs. A general consensus on the ability of the white dwarf to retain the accreted mass has not been reached yet (Hillman et al. 2020; Starrfield et al. 2020). Moreover, neither mechanism is able to explain the observed CV white dwarf mass distribution without creating conflicts with other observational constraints.

A promising alternative solution proposed throughout the last couple of years assumes that the standard CV evolution model is incomplete. Schreiber et al. (2016) suggested that consequential angular momentum loss (CAML) is the key missing ingredient. This sort of angular momentum loss arises from the mass transfer process itself and acts in addition to magnetic braking and gravitational wave radiation. Schreiber et al. (2016) developed an empirical model (eCAML) in which the strength of CAML is inversely proportional to the white dwarf mass, leading to dynamically unstable mass transfer in most CVs hosting low-mass white dwarfs ($M_{WD} \lesssim 0.6\,M_{\odot}$). The majority of these systems would not survive as semi-detached binaries but the two stellar components would instead merge into a single object (see also Nelemans et al. 2016). The main strength of the eCAML model is that it can also solve other disagreements between theory and observations, such as the observed CV space density and orbital period distribution (Zorotovic & Schreiber 2017; Belloni et al. 2018, 2020; Pala et al. 2020), without the requirement of additional fine tuning. However, the exact physical mechanism behind this additional source of angular momentum loss and the reason for its dependence on the white dwarf mass are still unclear.

Finally, it has to be considered that, while observational biases can be ruled out, it is more difficult to assess the presence of systematics affecting Zorotovic et al. (2011)'s results, which were based on a sample of only 32 systems with accurate mass measurements, 22 of which were derived from the analysis of their eclipse light curves. Given that the previous results were mainly based on one methodology, it is necessary to increase the number of systems with an accurate mass measurement and diversify the methods employed in order to confirm the inferred high masses of CV white dwarfs, which remains one of the biggest and unresolved issues for the theoretical modelling of CV evolution.

An alternative method to measure CV white dwarf masses consists of the analysis of their ultraviolet spectra. The ultraviolet waveband is optimal for studying the underlying white dwarfs as they are relatively hot ($T_{eff} \geq 10\,000\,K$, Sion 1999; Pala et al. 2017) and dominate the emission at these wavelengths, while the optical waveband is contaminated by the emission from the accretion flow and the companion star. From the knowledge of the distance to the system, the white dwarf radius (R_{WD}) can be derived from the scaling factor between the best-fitting model and the ultraviolet spectrum. Under the assumption of a mass-radius relationship, it is then possible to measure the white dwarf mass. Another possibility is to perform a dynamical study. The radial velocities of the white dwarf and the donor allow to infer the white dwarf gravitational redshift that, combined with a mass-radius relationship, provides the mass of the white dwarf.

Over the last 30 years, the *Hubble Space Telescope* (*HST*) has proven to be essential for the study of CVs, delivering ultraviolet

Table 1. Log of the *HST* ultraviolet observations of the 43 CV white dwarfs studied in this work along with the corresponding *Gaia* EDR3 parallaxes (corrected for the zero point, see Section 2.1.1), sorted by increasing orbital period. The distances have been computed following the method described in Pala et al. (2020), assuming the reported scale height h. The colour excess $E(B-V)$ have been derived using the STructuring by Inversion the Local Interstellar Medium (Stilism) reddening map (Lallement et al. 2018). Systems highlighted with a star symbol are known to be eclipsing.

System	$P_{\rm orb}$ (min)	h (pc)	$E(B-V)$ (mag)	Instrument	Grating	Central λ (Å)	Total exposure time (s)	Observation date	*Gaia* EDR3 ID	ϖ (mas)	d (pc)
SDSS J150722.30+523039.8*	66.61	260	$0.018^{+0.006}_{-0.018}$	COS STIS	G140L G230LB	1230 2375	9762 5226	2010 Feb 18	1593140224924964864	4.73 ± 0.09	211 ± 4
SDSS J074531.91+453829.5	76.0	260	0.027 ± 0.017	COS	G140L	1105	5486	2012 Mar 13	927255749553754880	3.2 ± 0.2	310^{+23}_{-20}
GW Lib	76.78	260	0.022 ± 0.018	COS	G140L	1105	7417	2013 May 30	6226943645600487552	8.88 ± 0.06	112.6 ± 0.8
SDSS J143544.02+233638.7	78.0	260	0.02 ± 0.02	COS	G140L	1105	7123	2013 Mar 09	1242828982729309952	4.8 ± 0.2	208^{+9}_{-8}
OT J213806.6+261957	78.1	260	0.017 ± 0.015	COS	G140L	1105	4760	2013 Jul 25	1800384942558699008	10.11 ± 0.04	98.9 ± 0.4
BW Scl	78.23	260	$0.002^{+0.015}_{-0.002}$	STIS	E140M	1425	1977	2006 Dec 27	2307289214897332480	10.71 ± 0.05	93.4 ± 0.5
LL And	79.28	260	$0.06^{+0}_{-0.02}$	STIS	G140L	1425	4499	2000 Dec 07	2809168096329043712	1.6 ± 0.6	609^{+343}_{-205}
AL Com	81.6	260	0.045 ± 0.018	STIS	G140L	1425	4380	2000 Nov 27	3932951035266314496	1.9 ± 0.6	523^{+252}_{-149}
WZ Sge	81.63	260	$0.003^{+0.015}_{-0.003}$	FOS	G130H	1600	3000	1992 Oct 08	1809844934461976832	22.14 ± 0.03	45.17 ± 0.06
SW UMa	81.81	260	$0.008^{+0.017}_{-0.008}$	STIS	G140L	1425	4933	2000 Mar 26	1030279027003254784	6.23 ± 0.06	160.6 ± 1.6
V1108 Her	81.87	260	0.046 ± 0.019	COS	G140L	1105	7327	2013 Jun 06	4538504384210935424	6.8 ± 0.1	148 ± 2
ASAS J002511+1217.2	82.0	260	$0.009^{+0.016}_{-0.009}$	COS	G140L	1105	7183	2012 Nov 15	2754909740118313344	6.4 ± 0.1	157 ± 3
HV Vir	82.18	260	$0.024^{+0.012}_{-0.021}$	STIS	G140L	1425	4535	2000 Jun 10	3688359000015020800	3.2 ± 0.3	317^{+29}_{-25}
SDSS J103533.02+055158.4*	82.22	260	$0.017^{+0.018}_{-0.017}$	COS	G140L	1105	12282	2013 Mar 08	3859020040917830400	5.1 ± 0.3	195^{+12}_{-11}
WX Cet	83.90	260	$0.013^{+0.016}_{-0.013}$	STIS	E140M	1425	7299	2000 Oct 30	2355217815809560192	3.97 ± 0.13	252^{+9}_{-8}
SDSS J075507.70+143547.6	84.76	260	$0.011^{+0.015}_{-0.011}$	COS	G140L	1105	7183	2012 Dec 14	654539826068054400	4.2 ± 0.2	239^{+12}_{-11}
SDSS J080434.20+510349.2	84.97	260	$0.007^{+0.016}_{-0.007}$	COS	G140L	1105	5415	2011 Nov 03	935056333580267392	7.03 ± 0.11	142 ± 2
EG Cnc	86.36	260	$0.008^{+0.017}_{-0.008}$	STIS	G140L	1425	4579	2006 Dec 20	703580960947960576	5.4 ± 0.2	186 ± 7
EK TrA	86.36	260	0.034 ± 0.019	STIS	E140M	1425	4302	1999 Jul 25	5825198967486003072	6.61 ± 0.04	151.4 ± 0.8
1RXS J105010.8–140431	88.56	450	$0.005^{+0.015}_{-0.005}$	COS	G140L	1105	7363	2013 May 10	3750072904055666176	9.19 ± 0.09	109 ± 1
BC UMa	90.16	260	$0.017^{+0}_{-0.017}$	STIS	G140L	1425	12998	2000 Jul 18	787683052032971904	3.41 ± 0.13	293^{+11}_{-10}
VY Aqr	90.85	260	$0.008^{+0.016}_{-0.008}$	STIS	E140M	1425	7250	2000 Jul 10	6896767366186700416	7.08 ± 0.09	$141.3^{+1.9}_{-1.8}$
QZ Lib	92.36	450	0.10 ± 0.03	COS	G140L	1105	7512	2013 Apr 26	6318149711371454464	5.0 ± 0.2	199^{+11}_{-10}
SDSS J153817.35+512338.0	93.11	260	0.027 ± 0.018	COS	G140L	1105	4704	2013 May 16	1595085299649674240	1.64 ± 0.12	607^{+47}_{-40}
UV Per	93.44	260	0.07 ± 0.04	STIS	G140L	1425	900	2002 Oct 11	457106501671769472	4.04 ± 0.11	248^{+7}_{-6}
1RXS J023238.8–371812	95.04	450	$0.005^{+0.014}_{-0.005}$	COS	G140L	1105	12556	2012 Nov 01	4953766320874344704	4.68 ± 0.16	214^{+8}_{-7}
RZ Sge	98.32	260	0.03 ± 0.3	STIS	G140L	1425	900	2003 Jun 13	1820209309025797888	3.40 ± 0.08	294 ± 7
CY UMa	100.18	260	$0.018^{+0}_{-0.015}$	STIS	G140L	1425	830	2002 Dec 27	832942871937909632	3.27 ± 0.07	306 ± 6
GD 552	102.73	450	$0.007^{+0.015}_{-0.007}$	STIS	G140L G230LB	1425 2375	14580 4230	2002 Oct 24 2002 Aug 31	2208124536065383424	12.41 ± 0.04	80.6 ± 0.2
IY UMa*	106.43	260	$0.015^{+0}_{-0.015}$	COS	G140L	1105	4195	2013 Mar 30	855516540988615296	5.52 ± 0.07	181 ± 2
SDSS J100515.38+191107.9	107.6	260	$0.021^{+0.011}_{-0.014}$	COS	G140L	1105	7093	2013 Jan 31	626719772406892288	2.95 ± 0.17	339^{+21}_{-19}
RZ Leo	110.17	260	$0.023^{+0.015}_{-0.023}$	COS	G140L	1105	10505	2013 Apr 11	3799290858445023488	3.59 ± 0.15	279^{+12}_{-11}
AX For	113.04	260	0.018 ± 0.018	COS	G140L	1105	7483	2013 Jul 11	5067753236787919232	2.86 ± 0.08	349 ± 10
CU Vel	113.04	260	$0.007^{+0.015}_{-0.007}$	COS	G140L	1105	4634	2013 Jan 18	5524430207364715520	6.31 ± 0.04	158 ± 1
EF Peg	120.53	120	0.048 ± 0.019	STIS	E140M	1425	6883	2000 Jun 18	1759321791033449472	3.5 ± 0.2	288^{+21}_{-18}
DV UMa*	123.62	120	$0.02^{+0}_{-0.012}$	STIS	G140L	1425	900	2004 Feb 08	820959638305816448	2.60 ± 0.15	382^{+24}_{-21}
IR Com*	125.34	120	$0.019^{+0.021}_{-0.019}$	COS	G140L	1105	6866	2013 Jul 11	3955313418148878080	4.63 ± 0.06	216 ± 3
AM Her	185.65	120	0.017 ± 0.016	STIS	G140L	1425	10980	2002 Jul 11/12	2123837555230207744	11.37 ± 0.03	87.9 ± 0.2
DW UMa*	196.71	120	$0.009^{+0.018}_{-0.009}$	STIS	G140L	1425	26144	1999 Jan 25	855119196836523008	1.73 ± 0.02	579^{+7}_{-6}
U Gem	254.74	120	$0.003^{+0.015}_{-0.003}$	FOS	G130H	1600	360	1992 Sep 28	674214551557961984	10.75 ± 0.03	93.0 ± 0.3
SS Aur	263.23	120	0.047 ± 0.033	STIS	G140L	1425	600	2003 Mar 20	968824328534823936	4.02 ± 0.03	249 ± 2
RX And	302.25	120	0.02 ± 0.02	GHRS	G140L	1425	1425	1996 Dec 22	374510294830244992	5.08 ± 0.03	197 ± 1
V442 Cen	662.4	120	0.048 ± 0.015	STIS	G140L	1425	700	2002 Dec 29	5398867830598349952	2.92 ± 0.04	343 ± 5

Notes. For several systems in our sample, *IUE* spectroscopic observations covering the wavelength range $1800 - 3200$ Å are available. These data allow to estimate the interstellar reddening due to dust absorption from the bump at $\simeq 2175$ Å and their analysis is available in the literature (CU Vel, Pala et al. 2017; DW UMa, Szkody 1987; AM Her, Raymond et al. 1979; UV Per, Szkody 1985; SW UMa, WZ Sge, U Gem, RX And, VY Aqr and SS Aur, La Dous 1991). The $E(B-V)$ literature measurements from *IUE* are all in agreement with those from Stilism. However, since the former do not have associated uncertainties, we decided to adopt the latter in our analysis, since Stilism provides the corresponding uncertainties and allows us to properly account for them when evaluating those associate with the white dwarf parameters.

Table 2. Characteristics of the gratings and setup of the *HST* observations used in this work.

Instrument	Aperture	Grating	Central wavelength[e]	Wavelength coverage	Resolution
COS	PSA[a]	G140L	1105 Å	1105 − 1730 Å	≃ 3000
FOS	1"	G130H	1600 Å	1150 − 1610 Å	≃ 1200
GHRS	LSA[b]	G140L	1425 Å	1149 − 1435 Å	≃ 2000
STIS	0.2" × 0.2"	E140M[c]	1425 Å	1125 − 1710 Å	≃ 90 000
	52" × 0.2"	G140L	1425 Å	1150 − 1700 Å	≃ 1000
		G230L[d]	2375 Å	1650 − 3150 Å	≃ 800

Notes. *(a)* Primary Science Aperture (2.5"); *(b)* Large Science Aperture (2.0"), *(c)* We re-bin the data obtained with the E140M grating to match the resolution of the G140L observations in order to increase the signal-to-noise ratio. *(d)* Only used in the cases of SDSS J150722.30+523039.8 and GD 552 to complement the G140L data, which provide the full coverage of Lyα from the white dwarf photosphere. *(e)* The central wavelength is defined as the shortest wavelength recorded on the Segment A of the detector.

observations[1] for 193 systems. Nonetheless, in the past, only a handful of objects had mass measurements derived from the analysis of their ultraviolet data because of the lack of accurate CV distances. In this respect, the *Gaia* space mission represents a milestone for CV research, delivering accurate parallaxes for a large number of these interacting binaries, finally enabling a quantitative analysis of the ultraviolet data obtained over the past decades.

We here analyse the *HST* observations of 43 CVs for which the white dwarf is the dominant source of emission in the ultraviolet wavelength range, and for which *Gaia* parallaxes from the Third Early Data release (EDR3) are available. To provide an additional independent determination to test our results and assess the presence of systematics, we complement this data set with optical phase-resolved observations obtained with X-shooter mounted on the Very Large Telescope (VLT), which provides independent dynamical mass measurements. We present this large CV sample, which doubles the number of objects with accurate $M_{\rm WD}$ measurements, providing new constraints on the response of the white dwarf to the mass accretion process, and for the further development of models for CV evolution.

2 SAMPLE SELECTION AND OBSERVATIONS

2.1 Ultraviolet observations

Among the 193 systems in the *HST* ultraviolet archive, 191 have a *Gaia* EDR3 parallax (Table E1) and have been observed with either the Goddard High Resolution Spectrograph (GHRS), the Faint Object Spectrograph (FOS), the Space Telescope Imaging Spectrograph (STIS) or the Cosmic Origin Spectrograph (COS) with a setup suitable for our analysis, i.e. (at least) the full coverage of the Lyα (1100 − 1600 Å) from the white dwarf photosphere with a resolution

---

[1] It is worth mentioning that also the *Far Ultraviolet Spectroscopic Explorer (FUSE)* and the *International Ultraviolet Explorer (IUE)* provided a plethora of CV ultraviolet spectra. However, the wavelength range ($\simeq 920 - 1180$ Å) of the *FUSE* observations is too limited for an accurate spectral fit with atmosphere models for white dwarfs with $T_{\rm eff} \lesssim 20\,000$ K. This is because their spectra are characterised by a low flux level due to the broad absorption lines from the higher orders of the Lyman series and, possibly, are complicated by heavy contamination from interstellar H_2. In *IUE*, the 45 cm diameter mirror only allowed good signal-to-noise ratio observations of the brightest CVs.
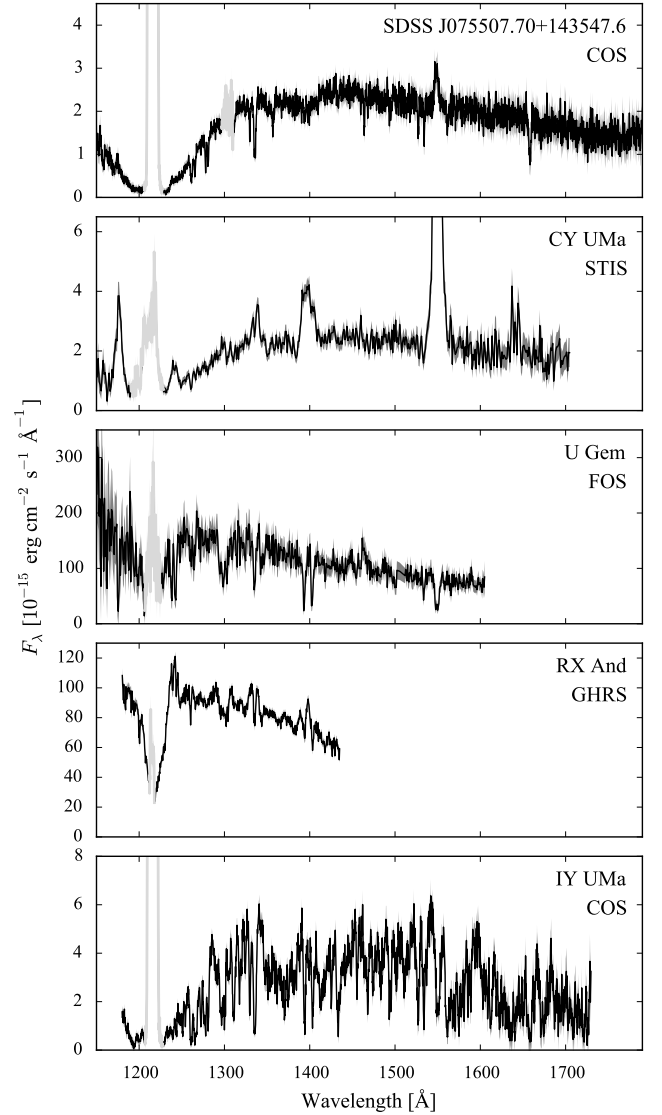
Figure 1. Sample *HST* spectra showing, from top to bottom, four typical quiescent CVs (SDSS J075507.70+143547.6, CY UMa, U Gem and RX And) observed with different *HST* instruments, and one eclipsing system (IY UMa) whose spectrum is characterised by the presence of the iron-curtain. The geocoronal emission lines of Lyα (1216 Å) and O I (1302 Å, not always detected) are plotted in grey.

of $R \simeq 1000 - 3000$. Together with a signal-to-noise ratio (SNR) of at least $\simeq 10$ and the knowledge of the distance to the systems, this setup allows an accurate determination of the white dwarf effective temperatures, chemical abundances and masses (Gänsicke et al. 2005).

CVs are characterised by an intrinsic variable behaviour that can affect the analysis of their ultraviolet data. A large fraction of CVs spend most of their time in a quiescent state, in which the accretion rate onto the white dwarf is very low, though the mass buffered in the accretion disc is slowly built up. During this phase, the white dwarf dominates the spectral appearance of the system and, at ultraviolet wavelengths, is recognisable from broad Lyα absorption centred on 1216 Å. The profile of Lyα changes with $T_{\rm eff}$, becoming more defined and narrower in the hotter white dwarfs, while the continuum slope of the spectrum becomes steeper (Figure 1). Periods of quiescence are
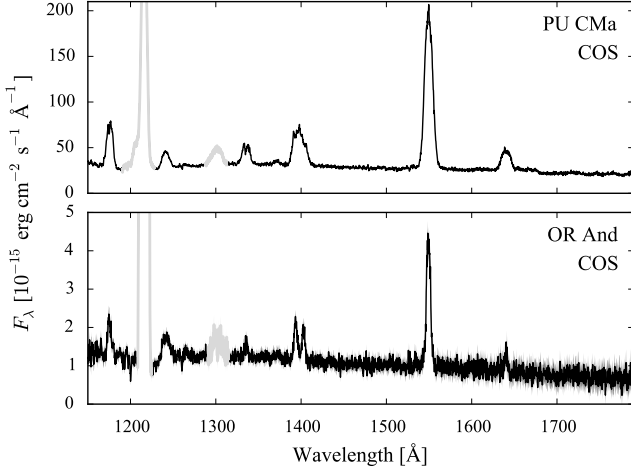
Figure 2. Sample *HST* spectra of a dwarf nova observed four days after a disc outburst (PU CMa, top panel) and a nova-like star observed in its normal high state (OR And, bottom panel). The spectra are dominated by the disc emission rather than the white dwarf. The geocoronal emission lines of Ly α (1216 Å) and O I (1302 Å) are plotted in grey.

Figure 3. Comparison between the distances to our targets computed as the inverse of the parallax (ϖ^{-1}) and using a statistical approach via the assumption of an exponentially decreasing volume density prior. The data are colour coded according to the parallax fractional error. The fractional difference, defined as $(D - \varpi^{-1})/\varpi^{-1}$, between the two methods is typically less than one per cent (red dashed lines in the bottom panel).

interrupted by sudden brightenings with amplitudes of 2–5 mag and, occasionally up to 9 mag (Warner 1995; Maza & Gonzalez 1983; Templeton 2007), called dwarf nova outbursts, when a fraction of the disc mass is rapidly drained onto the white dwarf. These outbursts arise from thermal-viscous instabilities in their accretion discs, causing a variation in the mass transfer rate through them (Osaki 1974; Hameury et al. 1998; Meyer & Meyer-Hofmeister 1984). Immediately after the occurrence of an outburst, the disc is hot and while it cools down it can partially or totally outshine the emission of the white dwarf even in the ultraviolet (top panel of Figure 2).

Following an outburst, the white dwarf is heated as a consequence of the increased infall of material, and this can possibly give rise to a non-homogeneous distribution of the temperature across its visible surface. Heated accretion belts or hot spots can dominate the overall ultraviolet emission of the system and the resulting temperature gradient results in the white dwarf radius being underestimated (e.g Toloza et al. 2016; Pala et al. 2019). The presence of a hot spot can be easily unveiled thanks to the modulation it introduces in the light curve of the system. In contrast, an equatorial accretion belt (Kippenhahn & Thomas 1978) can be difficult to detect since, being symmetric with respect to the rotation axis of the white dwarf, it does not cause variability on the white dwarf spin period (e.g GW Lib, Toloza et al. 2016). Therefore, the analysis of the ultraviolet data obtained after a disc outburst provides only an upper limit on the white dwarf effective temperature and radius and, in turn, only a lower limit on its mass.

Additionally, members of a sub-class of CVs, known as nova-like systems, are characterised by high mean mass-transfer rates which usually keep the discs in a stable hot state, equivalent to a dwarf nova in permanent outburst. In this high state, the disc dominates the spectral appearance even in the far ultraviolet, preventing a direct detection of the white dwarf (bottom panel of Figure 2). However, occasionally, it is thought that as a consequence of starspots appearing in, or migrating into the tip of the donor star at the first Lagrangian point (Livio & Pringle 1994), the mass transfer rate drops (low state) and unveils the white dwarf (e.g. Gänsicke & Koester 1999; Knigge et al. 2000; Hoard et al. 2004). These low states typically last for days up to years (e.g Rodríguez-Gil et al. 2007) and provide a window in
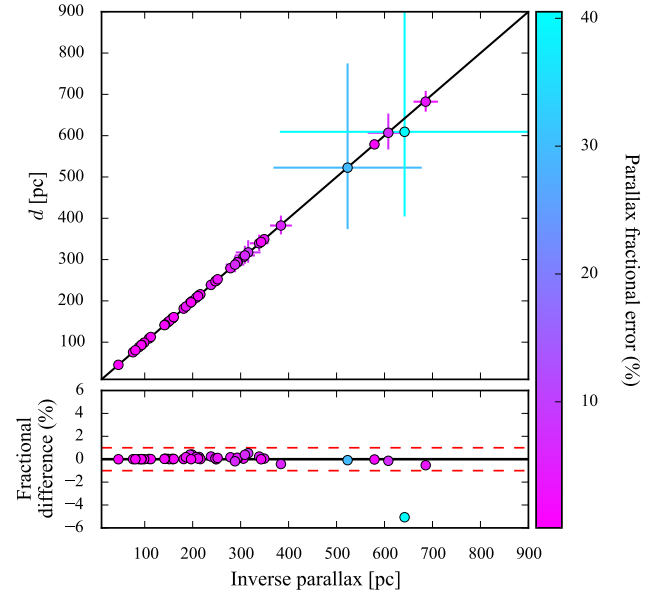
which the white dwarf parameters can be measured (e.g. Gänsicke et al. 1999; Knigge et al. 2000; Hoard et al. 2004)

While some nova-likes can be magnetic, similar behaviour is observed in highly magnetic CVs. A significant number (28 per cent, Pala et al. 2020) of CVs contain strongly ($B \gtrsim 10\,\mathrm{MG}$) magnetic white dwarfs, whose magnetism suppresses the formation of an accretion disc and forces the accretion flow to follow the field lines. The strong field of the white dwarf may have a deep impact on the evolution of the system (Schreiber et al. 2021). Similar to nova-likes, magnetic CVs are also characterised by alternating between high and low states, on time-scales of months to years. During high states, mass accretion is stable and the ultraviolet emission is dominated by a hot polar cap close to one (or both) the magnetic pole(s) of the white dwarf. During low states, the hot-caps emission is greatly weakened and the white dwarf dominates the spectral appearance of the system. Possibly, low states in magnetic CVs are also triggered by a donor stellar spot passing around the first Lagrangian point region (Hessman et al. 2000). In low states, time-resolved observations are required in order to account for the possible contribution from the accretion cap and to obtain accurate white dwarf parameters.

Finally, CVs experience (at least once in their life) powerful classical nova eruptions due to thermonuclear runaways at their surface. CVs that have been observed to undergo these eruptions are known as novae and their ultraviolet spectra are dominated by the emission from a hot highly variable component (e.g. Cassatella et al. 2005), whose origin is still not clear, that prevents the direct detection of the white dwarf.

To account for the high variable nature of CVs, we inspected the archival ultraviolet *HST* data and discarded (i) dwarf novae observed during or immediately after a disc outburst; (ii) nova-likes in high state and novae and (iii) polars lacking time-resolved observations with sufficient orbital phase coverage, necessary to determine a spectrum of the underlying white dwarf (see e.g. Gänsicke et al. 2006).

Table 3. Log of the optical observations of the three CVs observed with X-shooter in which the signatures of both the white dwarf and the secondary star were identified in their spectra. We obtained time-series of N spectra with T exposure time each.

		UVB			VIS			NIR		
System	Observation date (YYYY-MM-DD)	Exposure time N×T(s)	Slit width (″)	Resolution (Å)	Exposure time N×T(s)	Slit width (″)	Resolution (Å)	Exposure time N×T(s)	Slit width (″)	Resolution (Å)
AX For	2013-10-25	7 × 606	1.0	0.99	13 × 294	0.9	0.90	22 × 200	0.9	2.11
	2015-09-24	12 × 610	1.3	1.10	12 × 592	1.2	0.90	12 × 642	1.2	2.06
IR Com	2014-03-05	29 × 270	1.0	1.01	21 × 412	0.9	0.89	31 × 300	0.9	2.02
V1108 Her	2015-05-12	12 × 480	1.0	1.04	10 × 587	0.9	0.92	12 × 520	0.9	2.07

In addition, we also discarded systems hosting a nuclear evolved donor. These CVs descend from binaries that underwent a thermal-time-scale mass transfer phase (Schenker et al. 2002) and can be easily identified from their enhanced N v/C iv line flux ratios (Gänsicke et al. 2003). In these systems, the white dwarf accretes helium rich material from its companion and this anomalously large helium abundance can cause an asymmetrical broadening of the blue wing of the Lyα (Gänsicke et al. 2018), thus affecting the estimates of the white dwarf surface gravity and temperature (Toloza et al., in preparation).

The final sample consists of 43 systems[2] and a log of their spectroscopic observations is presented in Table 1, while the different observational setups are listed in Table 2. Finally, the full list of CVs observed with *HST* is provided in Appendix E.

2.1.1 Quality of the Gaia data

Gaia astrometric solutions, and thereby parallaxes, are known to be affected by systematics arising from imperfections in the instrument and data processing methods (Lindegren et al. 2020). The mean value of the systematic error, the so-called parallax zero point ϖ_{zp}, can be modelled according to the ecliptic latitude, magnitude and colour of each *Gaia* EDR3 source. We employed the python code provided by the *Gaia* consortium[3] to compute ϖ_{zp} for our targets, and corrected their parallaxes by subtracting the estimated zero point to the quoted *Gaia* EDR3 parallaxes. This correction ranges from 0.5μas, in the case of V1108 Her, to -43μas for U Gem.

Together with the main kinematic parameters (positions, proper motions and magnitudes), which are used to derive the astrometric solution for each source, *Gaia* EDR3 also provides a series of ancillary parameters that can be used to evaluate the accuracy of this solution. Among the most relevant ones is the `astrometric_excess_noise`, which represents the error associated with the astrometric modelling (see Lindegren et al. 2012) and that, ideally, should be zero. Following Pala et al. (2020), we verified that the sources in our sample have reliable parallaxes by satisfying the condition `astrometric_excess_noise < 2`.

Converting parallaxes into distances is not always trivial as the mere inversion of the parallax can introduce some biases in the distance estimate, especially when the fractional error on the parallax is larger than 20 per cent (see e.g. Bailer-Jones 2015; Luri et al.

2018), which is the case for two systems in our sample, AL Com and LL And. Their large uncertainties are most likely related to their intrinsic faintness ($G = 19.7$, $G = 20.1$, respectively) since the other *Gaia* parameters that flag possible issues with the astrometric solution (`astrometric_excess_noise` and RUWE, described below) are within the range expected for well-behaved sources. We therefore computed the distance to each CV using a statistical approach, in which we assumed an exponentially decreasing volume density prior and a scale height h following the method[4] described in Pala et al. (2020). Typically, the distances computed with the two methods differ by less than one per cent, the only exception being LL And with a difference of five per cent (Figure 3).

Another important parameter to assess the reliability of the parallaxes is the renormalised unit weight error (RUWE). This represents the square root of the normalised chi-square of the astrometric fit, scaled according to the source magnitude G, its effective wavenumber v_{eff} and its pseudocolour $\hat{v}_{\text{eff}}$ (see Lindegren et al. 2020 for more details). Ideally, for well-behaved sources[5], RUWE < 1.4. However, we noticed that for the system in our sample with the largest RUWE, AM Her (RUWE = 2.8), the distance derived from its *Gaia* parallax (88.1 ± 0.4 pc) is consistent with the distance estimated by Thorstensen (2003), 79^{+9}_{-6} pc. Similarly, in the case of U Gem, another system with high weight error (RUWE = 2.4), its *Gaia* parallax ($\varpi = 10.75 \pm 0.03$ mas) and corresponding distance (93.4 ± 0.5 pc) are in good agreement, respectively, with the parallax measurements obtained using the *HST* Fine Guidance Sensors by Harrison et al. (2000) ($\varpi = 10.30 \pm 0.50$ mas) and Harrison et al. (2004) ($\varpi = 9.96 \pm 0.37$ mas), and with the distance estimated by Beuermann (2006), 97 ± 7 pc. These large values of RUWE are most likely related to colour variations of the systems during different *Gaia* observations, caused either by the occurrence of low and high states in AM Her (Gänsicke et al. 2006), and disc outbursts in U Gem. Nonetheless, since their *Gaia* astrometry still provides reliable distances, we decided to not apply any cut on this parameter for the remaining systems, which all have lower RUWE values.

---

[2] Pala et al. (2017) reported that AX For went into outburst five days before the *HST* observations. The analysis of the ultraviolet data provides only a lower limit on the white dwarf mass. Nonetheless, we included this system in our sample since we measured its mass from additional optical phase-resolved observations.

[3] https://gitlab.com/icc-ub/public/gaiadr3_zeropoint

[4] The distance to the targets in our sample have also been computed from their *Gaia* EDR3 parallaxes by Bailer-Jones et al. (2021), with a method which also employs an exponentially decreasing volume density prior and a scale height calibrated against the stellar distribution at different Galactic latitudes. Nonetheless, we preferred to recompute the distances to our targets following the method described in Pala et al. (2020), since it employs a scale height that accounts for the age of the systems (as described in Pretorius et al. 2007) and is therefore more representative of the properties of the CV population.

[5] See the document "Re-normalising the astrometric chi-square in Gaia DR2", which can be downloaded from: https://www.cosmos.esa.int/web/gaia/public-dpac-documents
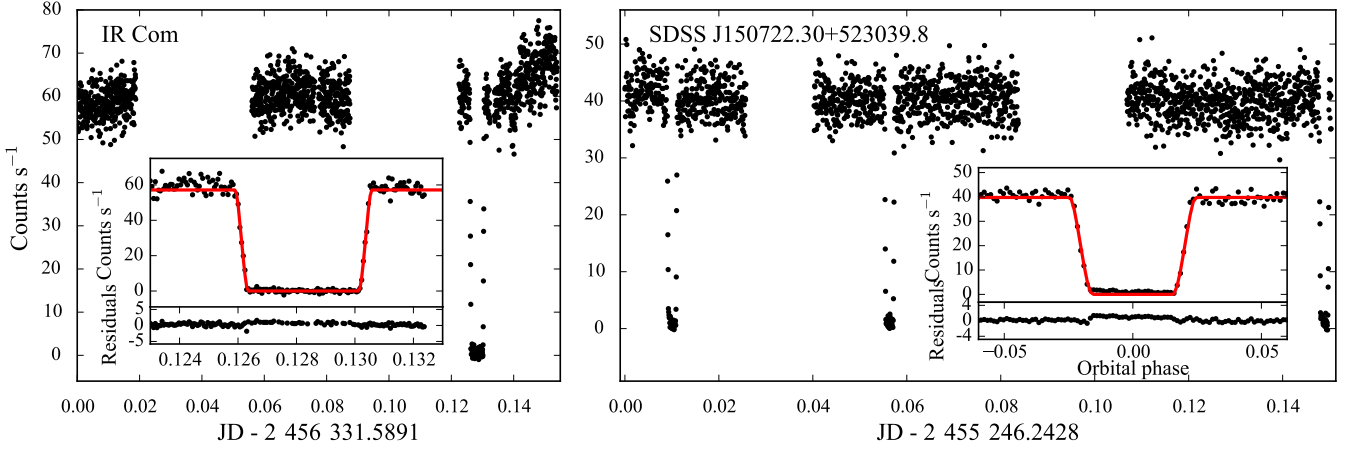
Figure 4. *HST*/COS light curves of IR Com (left) and SDSS J150722.30+523039.8 (right). The absence of any contamination from the bright spot allows us to fit the the eclipse light curve and measure the mass of the white dwarf in these systems. The insets show a close-up of the eclipse of IR Com and of the average phase-folded eclipse light curve of SDSS J150722.30+523039.8, along with the best-fitting models (red).

2.2 Optical spectroscopy

We obtained complementary phase-resolved spectroscopy with X-shooter (Vernet et al. 2011) of the 22 targets from the *HST* sample that are visible from the Southern hemisphere and in which (i) the white dwarf dominates the of emission in the ultraviolet and (ii) for which no dynamical study has been carried out before.

X-shooter is an échelle spectrograph located at the Cassegrain focus of UT2 of the VLT at the European Southern Observatory (ESO) in Cerro Paranal (Chile). It is equipped with three arms: blue (UVB, $\lambda \simeq 3000 - 5595$ Å), visual (VIS, $\lambda \simeq 5595 - 10\,240$ Å) and near-infrared (NIR, $\lambda \simeq 10\,240 - 24\,800$ Å), with a medium spectral resolution ($R \simeq 5000 - 10\,000$). For each arm, the slit width was chosen to best match the seeing and the exposure times were set with the aim to optimise the SNR and, at the same time, to minimise the orbital smearing. At the time of the observations the atmospheric dispersion correctors of X-shooter were broken and hence the slit angle was reset to the parallactic angle position after one hour of exposures. The data were reduced using the Reflex pipeline (Freudling et al. 2013). To account for the well-documented wavelength shift between the three arms[6], we used theoretical templates of sky emission lines to calculate the shift of each spectrum with respect to the expected position. We then applied this shift together with the barycentric radial velocity correction to the data. Finally, a telluric correction was performed using `molecfit` (Smette et al. 2015; Kausch et al. 2015).

In the spectra of three (AX For, IR Com and V1108 Her) of the 22 CVs observed with X-shooter, we identified the Mg II absorption line at 4481 Å that originates in the white dwarf photosphere, and several absorption features arising from the secondary photosphere, including Na I (11 381/11 403 Å), K I (11 690/11 769 Å and 12 432/12 522 Å). The K I and Mg II lines, were used to track the motion of the two stellar components and to reconstruct their radial velocity curves from which the mass of the white dwarf can be determined. A log of the spectroscopic observations is presented in Table 3.

In the remaining 19 systems, we identified only signatures of either the white dwarf or the secondary, and in some cases of neither of them, and the analysis of these objects will be presented elsewhere.

3 METHODS

3.1 Light curve analysis

Throughout the duration of the individual *HST* observations (typically a few hours), CVs can show different types of variability, such as eclipses, modulations due to the white dwarf rotation, white dwarf pulsations, double humps and brightenings (e.g. Szkody et al. 2002b; Araujo-Betancor et al. 2003; Szkody et al. 2017; Toloza et al. 2016; Pala et al. 2019). Eclipses are particularly important since they allow a white dwarf mass measurement based only on geometrical assumptions to be obtained. In contrast, pulsations and brightenings reflect the presence of hot spots and, more generally, of a gradient in temperature over the visible white dwarf surface. When in view, the emission of the hot spots can dominate the overall ultraviolet emission of the system making the white dwarf look hotter and affecting both the temperature and mass estimates (Toloza et al. 2016; Pala et al. 2019). Therefore, it is important to remove the contribution of these spurious sources in order to obtain an accurate mass measurement.

The *HST* TIME–TAG data allow us to reconstruct a 2D image of the detector, where the dispersion direction runs along one axis and the spatial direction along the other, which can be used to reconstruct the light curve of the observed system. For each CV, we masked the geocoronal emission lines from Lyα (centred at 1216 Å) and O I (centred at 1300 Å) as well as all the most prominent emission features from the accretion disc, which are not representative of the white dwarf. Using five-second bins and following the method described in Pala et al. (2019), we then extracted the light curve of each target in counts per second.

For the objects that did not exhibit any significant variability during their *HST* observations, the data from all the orbits were summed to produce an average ultraviolet spectrum. We discuss, in what follows, the eclipsing systems while the remaining six CVs that showed some level of variability within the time-scale of the *HST* observations are discussed in Appendix A.

---

[6] A report on the wavelength shift can be found at https://www.eso.org/sci/facilities/paranal/instruments/xshooter/doc/XS_wlc_shift_150615.pdf

3.1.1 Eclipsing systems

In eclipsing CVs, where the white dwarf is periodically obscured by its stellar companion, the duration of the ingress of the white dwarf, as well as the duration of the whole eclipse, can be used to derive the radius of both stars (R_{WD} and R_{donor} for the white dwarf and the donor, respectively) scaled by the orbital separation a:

$$\frac{R_{WD}}{a} = \frac{1}{2}\left(\sqrt{\cos^2 i + \sin^2 i \cos^2 \Phi_1} + \sqrt{\cos^2 i + \sin^2 i \cos^2 \Phi_2}\right) \quad (1)$$

$$\frac{R_{donor}}{a} = \frac{1}{2}\left(\sqrt{\cos^2 i + \sin^2 i \cos^2 \Phi_1} - \sqrt{\cos^2 i + \sin^2 i \cos^2 \Phi_2}\right) \quad (2)$$

In the above equations, Φ_1 and Φ_2 are the phases of the first and second contacts and are directly measured from the light curve, while i is the inclination of the system and is an additional unknown. Since the same eclipse profile can be reproduced by different inclinations and assuming different radii for the two stellar components, additional constraints are required to lift the degeneracy between these three parameters (R_{WD}, R_{donor} and i).

To this end, one of the most direct method consists in measuring the radial velocity amplitudes (K_{WD} and K_{donor}) of the two stellar components from phase-resolved spectroscopic observations. These quantities provide the system mass ratio $q = K_{WD}/K_{donor} = M_{donor}/M_{WD}$, which allows constraining the size of the Roche-lobe of the companion star (Eggleton 1983). Under the assumption that the donor is Roche-lobe filling, the degeneracy in the three quantities can be lifted. In this case, a fit to the eclipse light curve provides R_{WD}/a which, combined with a mass radius relationship and Kepler's third law, provides a measurement of the white dwarf mass (see e.g. Littlefair et al. 2006; Feline et al. 2005; Savoury et al. 2011; McAllister et al. 2019).

We detected the white dwarf eclipse in the COS light curves of four CVs, IR Com, IY UMa, SDSS J103533.02+055158.4 and SDSS J150722.30+523039.8. However, the data quality and orbital coverage allowed us to perform a fit to the eclipse light curve only in the cases of IR Com and SDSS J150722.30+523039.8. The remaining eclipsing systems are discussed in Appendix A0.1.

We used the `lcurve` tool[7] (see Copperwheat et al. 2010, for a detailed description of the code) to perform the light curve modelling and define the binary star model that best reproduces the observed eclipse. For IR Com we assumed the mass ratios derived from the radial velocity amplitudes from Section 3.3, $q = 0.016 \pm 0.001$. For SDSS J150722.30+523039.8 we used the mass ratio from Savoury et al. (2011), $q = 0.0647 \pm 0.0018$, which has been derived from the analysis of the optical light curve of the system. For both CVs, we assumed the white dwarf effective temperatures derived in Section 3.2, which are used by `lcurve` to estimate the flux contribution from the white dwarf. We kept the inclination i, R_{WD}/a and the time of middle eclipse T_0 as free parameters. The best-fitting models are shown in the insets in Figure 4 and returned $i = 80.5 \pm 0.3$ and $R_{WD}/a = 0.00956 \pm 0.0002$ for IR Com and $i = 83.5 \pm 0.3$ and $R_{WD}/a = 0.0185 \pm 0.0006$ for SDSS J150722.30+523039.8 respectively. The R_{WD}/a ratios, combined with the white dwarf mass radius relationship[8] (Holberg & Bergeron 2006; Tremblay et al. 2011) and Kepler's third law, provide $M_{WD} = 0.989 \pm 0.003$ M$_\odot$ for IR Com and $M_{WD} = 0.83^{+0.19}_{-0.15}$ M$_\odot$ for SDSS J150722.30+523039.8 (Table 6).

It is worth mentioning at this point that the eclipse of the white dwarf in DW UMa was detected in the STIS TIME–TAG data. This light

curve has already been analysed by Araujo-Betancor et al. (2003), which derived a white dwarf mass of $M_{WD} = 0.77 \pm 0.07$ M$_\odot$. Finally, DV UMa is also eclipsing but, since the data were acquired as snapshot, the lightcurve of the eclipse is not available.

3.2 Ultraviolet spectral fitting

To perform the spectral fit to the ultraviolet data, we generated a grid of white dwarf synthetic atmosphere models using TLUSTY and SYNSPEC (Hubeny 1988; Hubeny & Lanz 1995), covering the effective temperature range $T_{eff} = 9\,000 - 70\,000$ K in steps of 100 K, and the surface gravity range $\log(g) = 6.4 - 9.5$ in steps of 0.1 (where g is expressed in cgs units). As discussed by Pala et al. (2017), using a single metallicity is sufficient to account for the presence of the metal lines and possible deviations of single element abundances from the overall scaling with respect to the solar values do not affect the results of the fitting procedure. We therefore fixed the metal abundances to the values derived from the analysis of the same *HST* data by previous works (see Table 5 and references therein).

The white dwarf effective temperature correlates with its surface gravity: strong gravitational fields translate into pressure broadening of the lines; this effect can be balanced by higher temperatures that increase the fraction of ionised hydrogen, resulting in narrower absorption lines. It is not possible to break this degeneracy from the sole analysis of the *HST* data since they only provide the Lyα absorption profile which, in the case of cool CV white dwarfs, is limited to only the red wing of the line. Therefore, in the past, the analysis of CV ultraviolet *HST* data has been limited mainly to accurate measurements of the white dwarf effective temperatures, obtained for a fixed $\log(g)$ for the white dwarfs. Nowadays, thanks to the parallaxes provided by *Gaia* EDR3, the knowledge of the distance d to the system finally allows us to constrain the radius of the white dwarf. Under the assumption of a mass-radius relationship, the white dwarf mass can be derived from the scaling factor between the *HST* data and the best-fitting model, according to the equation:

$$S = \left(\frac{R_{WD}}{d}\right)^2 \quad (3)$$

By breaking this degeneracy, we can simultaneously measure both the white dwarf effective temperature and mass.

The *HST* ultraviolet spectra are contaminated by geocoronal emission of Lyα and O I (1302 Å). The first is always detected and we masked the corresponding wavelength range for our spectral analysis. In the case of O I, the related wavelength range was masked only when the emission was detected in the spectrum. Moreover, CV ultraviolet spectra show the presence of an additional continuum component, which contributes $\simeq 10 - 30$ per cent of the observed flux. The origin of this additional emission source is unclear and it has been suggested that it could arise from either (i) the disc, or (ii) the hot spot where the ballistic stream intersects with the disc or (iii) the interface region between the disc and the white dwarf surface (e.g. Long et al. 1993; Godon et al. 2004; Gänsicke et al. 2005). In the literature, different approximations have been used to model the emission of this additional component, such as a blackbody, a power law or a constant flux (in F_λ). As discussed by Pala et al. (2017), these assumptions represent a very simplified model of the additional continuum contribution and it is likely that none of them provides a realistic physical description of this emission component. These authors also showed that, when only a limited wavelength coverage ($1105 - 1800$ Å) is available, it is not possible to statistically discriminate among the three of them, and they all result in fits of similar quality for the white dwarf. We therefore decided to use a blackbody,

---

[7] https://github.com/trmrsh/cpp-lcurve
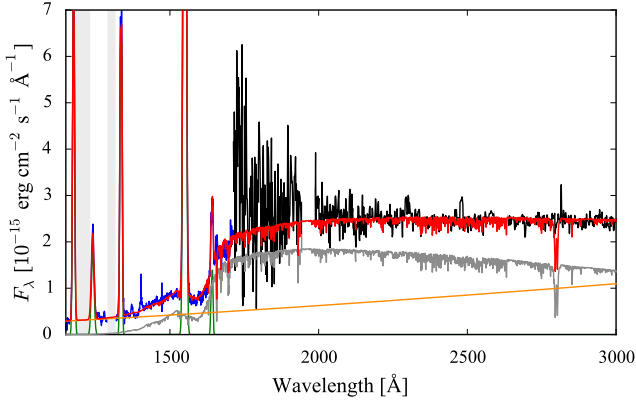[8] http://www.astro.umontreal.ca/~bergeron/CoolingModels

Figure 5. *HST* spectrum of GD 552 obtained from the combination of the STIS/G140L far-ultraviolet (blue) and STIS/G230L (black) data (the grey bands mask the geocoronal emission lines of Lyα at 1216 Å and of O I at 1302 Å, while the gaps at $\simeq$ 1950 Å and $\simeq$ 2600 Å correspond to data with bad quality flags). The best fitting model (red) is composed of the sum of the white dwarf emission (grey), the emission lines approximated as Gaussian profiles (green), and an additional second component (orange) which shows a clear dependence on wavelength. This suggests that this additional emission component in the system is either an optically thin emission region, or an optically thick accretion disc, or a bright spot. These cases are expected to display a power-law distribution and, in our fitting procedure, we assumed a power law to model the emission of this additional component in GD 552.

Table 4. Summary of the fit parameters employed in the analysis of the ultraviolet spectra described in Section 3.2.

System component		Parameter	Free?	Range of variation
		Distance	✗	–
		$E(B-V)$	✗	–
White dwarf		$T_{\rm eff}$ (K)	✓	9000 - 70 000
		$\log(g)$	✓	6.4 - 9.5
Emission lines		$f_{\rm em}$	✓	> 0
		$\lambda_{\rm em}$	✓	> 0
		$\sigma_{\rm em}$	✓	> 0
Second components	BB	$T_{\rm eff}$ (K)	✓	> 0
		scaling factor	✓	> 0
	PL	Exponent	✓	$\mathbb{R}$
		scaling factor	✓	> 0
	constant		✓	> 0
Slabs	Cold	$T_{\rm curtain}$ (K)	✓	5000 - 25 000
		$\log(n_{\rm e} \cdot {\rm cm}^3)$	✓	9 - 21
		$\log(N_{\rm H} \cdot {\rm cm}^2)$	✓	17 - 23
		$V_{\rm t}$ (km s^{-1})	✓	0 - 500
	Hot	$T_{\rm curtain}$ (K)	✓	25 000 - 120 000
		$\log(n_{\rm e} \cdot {\rm cm}^3)$	✓	9 - 21
		$\log(N_{\rm H} \cdot {\rm cm}^2)$	✓	17 - 23
		$V_{\rm t}$ (km s^{-1})	✓	0 - 500

which is described by two free parameters (a temperature and a scaling factor), because, in the limited wavelength here considered, its tail approximates both the power law and the constant flux cases.

The only exceptions are the eclipsing systems (discussed below) and GD 552. For the latter, additional data obtained with the G230L grating, covering the wavelength range $1650 - 3150$ Å, are available. As already noticed by Unda-Sanzana et al. (2008), the additional second component in the near-ultraviolet flux of GD 552 shows a clear dependence on wavelength (orange line in Figure 5). The observed slope could arise from either an optically thin emission region, or an optically thick accretion disc, or a bright spot. All cases are expected to display a power-law distribution (which, for the optically thick disc and the bight spot, results from the approximation with a sum of blackbodies) and, given the wide wavelength coverage available for this object, a single black body would represent a poor approximation for the additional emission component. Therefore, in the case of GD 552, we assumed a power law, which is described by two free parameters (a power law index and a scaling factor).

The analysis of the eclipsing systems is complicated by the presence of the so–called "iron curtain", i.e. a layer of absorbing material extending above the disc which gives rise to strong absorption features (see, for example, the spectrum of IY UMa in Figure 1), mainly a forest of blended Fe II absorption lines (Horne et al. 1994). These veil the white dwarf emission, making it difficult to establish the actual flux level (necessary to constrain the white dwarf radius). In addition, these lines modify the overall slope of the spectrum as well as the shape of the core of the Lyα line, which are the tracers for the white dwarf $T_{\rm eff}$. Out of the six eclipsing systems in our sample, two are strongly affected by the veiling gas: IY UMa and DV UMa. Following the consideration by Pala et al. (2017), in the spectral fitting of these CVs, we included two homogeneous slabs, one cold ($T_{\rm curtain} \simeq 10\,000$ K) and one hot ($T_{\rm curtain} \simeq 80\,000$ K). We generated two grids of monochromatic opacity of the slabs using SYNSPEC, one covering the effective

temperature range $T_{\rm eff} = 5\,000 - 25\,000$ K and the other the range $T_{\rm eff} = 25\,000 - 120\,000$ K, both in steps of 5000 K. Both grids covered the electron density range $n_{\rm e} = 10^9 - 10^{21} {\rm cm}^{-3}$ in steps of $10^3 {\rm cm}^{-3}$ and the turbulence velocity range $V_{\rm t} = 0 - 500$ km s^{-1} in steps of 100 km s^{-1}. These models, combined with the column densities ($N_{\rm H}$, for which we assumed a flat prior in the range $10^{17} - 10^{23}$ cm^{-2}), return the absorption due to the curtain. Given the large number of free parameters involved in the spectral fitting of the eclipsing systems, we chose to use a constant flux (in F_λ) to approximate the additional continuum component, as this is the simplest approximation and introduces only one more additional free parameter in the fitting procedure.

Finally, for all systems, whenever detected, we included the emission lines arising from the accretion disc as Gaussian profiles, allowing three free parameters: amplitude ($f_{\rm em}$), wavelength ($\lambda_{\rm em}$) and width ($\sigma_{\rm em}$). As shown by Pala et al. (2017), by including or masking the disc lines has no influence on the result but their inclusion allowed us to use as much of the data as possible.

We performed the spectral fit using the Markov chain Monte Carlo (MCMC) implementation for Python, EMCEE (Foreman-Mackey et al. 2013).

We scaled the models according to the distance to the system, computed as described in Section 2.1.1, and reddened them according to the extinction values reported in Table 1. We used the STructuring by Inversion the Local Interstellar Medium (Stilism) reddening map (Lallement et al. 2018) to derive the $E(B-V)$. For those objects not included in the Stilism reddening maps, we used instead the three-dimensional map of interstellar dust reddening based on Pan-STARRS 1 and 2MASS photometry (Green et al. 2019).

The free parameters of the fit and their allowed range of variations are listed in Table 4, and we assumed a flat prior in the ranges covered by the corresponding grid of models. We assumed the mass-radius relation of Holberg & Bergeron (2006); Tremblay et al. (2011) and constrained the parameters describing the black body (BB) and constant additional second components to be positive. In the case of the
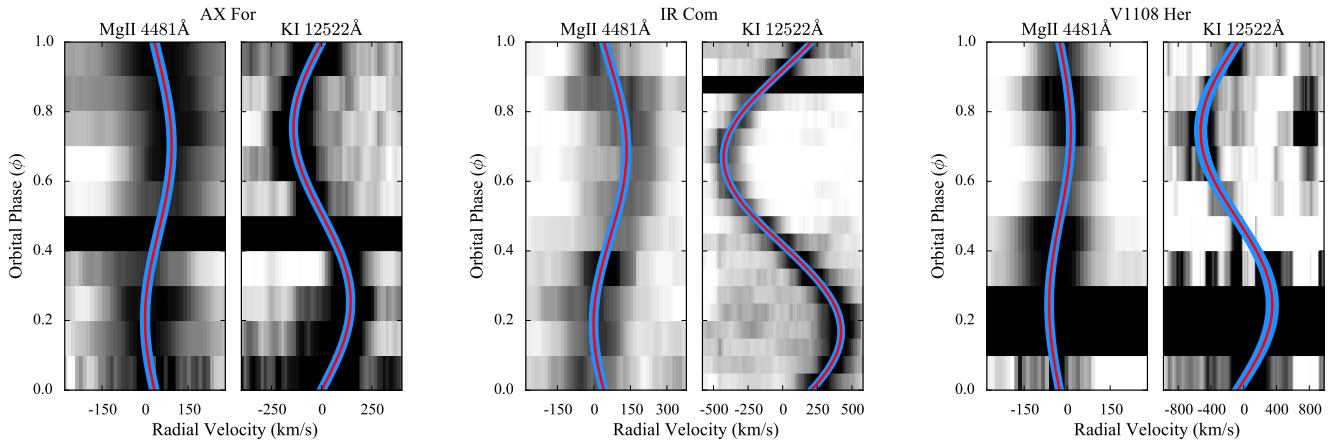
Figure 6. For each system, the trailed spectra for the Mg II line (4481 Å, left panel) and the K I line (12 522 Å, right panel) are shown. Overplotted are the best fitting models (red) along with their uncertainties (light blue).

power-law (PL) additional second component, we only constrained its scaling factor to be positive.

The accuracy derived from the statistical uncertainties are typically two and four per cent for $T_{\rm eff}$ and $R_{\rm WD}$, respectively. These uncertainties together provide an accuracy on the white dwarf masses of typically 0.03 $M_\odot$. However, the real uncertainties are dominated by systematic effects, which are discussed in the following Section.

3.2.1 Uncertainty estimate

As discussed by Pala et al. (2017), we can rule out the presence of systematics arising from instrument flux calibration issues as well as any noticeable contamination from additional Lyα absorption from the second emission component and/or interstellar gas along the line of sight. Moreover, the uncertainties related to the unknown nature of the second component are smaller than the statistical errors from the fitting procedure (Pala et al. 2017), therefore their effect is already accounted for in the error balance from the previous Section.

The remaining sources of uncertainties are hence those related to the precision on the *Gaia* parallaxes and the reddening measurements. The reddening due to interstellar dust along the line of sight affects the overall slope and flux level of the observed spectrum, thus influencing both the radius and $T_{\rm eff}$ measurements. Similarly, the precision on the *Gaia* parallax directly reflects that in the radius and hence in the white dwarf mass.

Allowing a 3σ variation for both the parallax and the reddening, the observed flux level of a system could be reproduced by a combination of high reddening (i.e. more absorption along the line of sight) and a large parallax (i.e. moving the object closer to the observer) and vice versa. This degeneracy cannot be broken from the sole analysis of the *HST* data since they do not extend to the wavelength range where the signature of interstellar dust absorption could be detected as a bump at $\simeq 2175$ Å, from which the colour excess can be estimated.

Ideally, the spectroscopic fitting procedure described in the previous section could account for this correlation by allowing both the distance and the reddening to vary according to suitable priors. In practice, this approach would require including in our fitting procedure the probability density function we used to compute the distance to each system in Section 2.1.1. Since this is not straightforward, we preferred to use an alternative method and estimate the systematic uncertainty on our mass measurements employing a Monte Carlo ap-

proach. We used a χ^2 minimisation routine to fit each spectrum 5000 times. During each execution, the models were scaled assuming a distance drawn randomly from the probability density function used to compute the distance to each system in Section 2.1.1. Similarly, the models were also corrected for the reddening, assuming a colour excess drawn randomly from a normal distribution, centred on the $E(B-V)$ reported in Table 1 and weighted according to its uncertainty. Keeping the distance and the reddening fixed to the values drawn from these distributions, we allowed as free parameters the white dwarf $T_{\rm eff}$ and $\log(g)$ and the second continuum component (as defined in the previous Section). To speed up the calculation, we masked the emission lines.

From the best-fitting parameters obtained from each of the 5000 executions, we derived the posterior distribution of $T_{\rm eff}$ and $\log(g)$, which provided the estimates of the systematic uncertainties related to the accuracy on the distance and the reddening. We compared these systematics with the statistical uncertainties derived in the previous Section and assumed as final value the maximum of the two.

In the next few years, the upcoming *Gaia* data releases will improve the accuracy on the parallaxes, and thereby that on the distances to CVs, and will allow reconstruction of more detailed three-dimensional reddening maps. Eventually, these will make it possible to reduce the uncertainties on the white dwarf parameters to the level of the statistical ones.

3.3 Radial velocity measurements from optical spectra

Among the different lines arising from the secondary photosphere listed in Section 2.2, the K I (12 432/12 522 Å) lines are the strongest and the only ones visible in the spectra of all three systems. The Na I doublet is only visible in the spectra of IR Com but it is contaminated by the residual of the telluric line removal. Therefore, we decided not to include it in the following analysis. We used the Mg II absorption feature and the K I lines to track the reflex motion of the white dwarf and the donor, respectively. Our data were characterised by a relatively low SNR ($\simeq 10 - 20$ in the UVB and $\simeq 5$ in the NIR) and, moreover, the NIR spectra showed strong contamination from the residuals from the sky lines subtraction. Therefore, to achieve more robust radial velocity measurements, we fit all the spectra of each object simultaneously (as done, for example, by Parsons et al. 2012 and Pala et al. 2019).

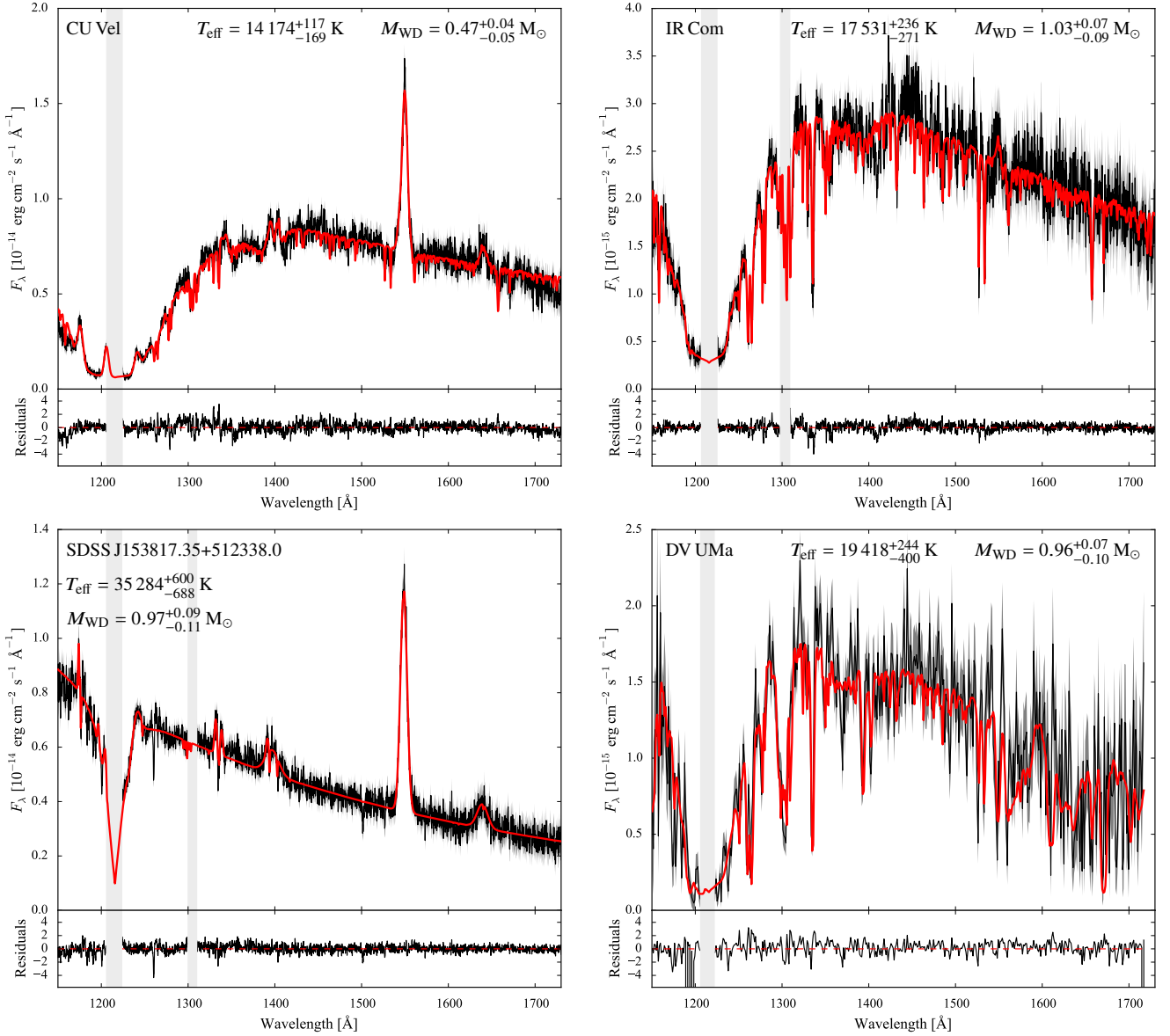We first fitted the K I absorption lines using a combination of a

Figure 7. Ultraviolet spectra (black) of sample CV white dwarfs along with the best-fitting model (red), representative of cool (top left panel), warm (top right pane), hot (bottom left panel) and eclipsing (bottom right panel) systems. The best-fitting models are composed of the sum of a white dwarf synthetic atmosphere model, a second continuum emission component in the form of a blackbody, and the emission lines from the disc modelled with a Gaussian profile. In addition, the model for the eclipsing system DV UMa (bottom right) includes an "absorption curtain" component (see Section 3.2). The grey bands mask the geocoronal emission lines of Ly α (1216 Å) and, whenever present, of O I (1302 Å).

constant and a double Gaussian of fixed separation. We allowed the wavelength of the Gaussians to change according to the following Equation:

$$V = \gamma + K \sin[2\pi(\phi - \phi_0)] \qquad (4)$$

where V is the radial velocity, γ is the systemic velocity, K is the velocity amplitude, ϕ is the orbital phase and ϕ_0 is the zero point of the ephemeris. We fitted the Mg II absorption lines using a combination of a constant and a single Gaussian. From these fitting procedures, we derived the systemic velocities of the white dwarf and the donor ($\gamma_{\rm WD}$ and $\gamma_{\rm donor}$, Figure 6). Their difference provides a direct measurement of the gravitational redshift of the white dwarf and thereby

of its surface gravity (Greenstein & Trimble 1967):

$$v_{\rm grav}({\rm WD}) = \gamma_{\rm WD} - \gamma_{\rm donor} = 0.635 \frac{M_{\rm WD}}{M_\odot} \frac{R_\odot}{R_{\rm WD}} \, {\rm km \, s^{-1}} \qquad (5)$$

At the surface of both the white dwarf and the secondary, a contribution from the gravitational field of the other star is present. For $P_{\rm orb} < 5\,{\rm h}$, CV secondary stars have typically $M_{\rm donor} \lesssim 0.6\,{\rm M_\odot}$ and $\log(g)_{\rm donor} \lesssim 5$ (e.g. Knigge et al. 2011), therefore their contribution only introduces a small correction near the white dwarf surface, $\simeq 0.1\,{\rm km\,s^{-1}}$. Similarly, the influence of the gravitational potential of the white dwarf introduces a correction of $\simeq 1\,{\rm km\,s^{-1}}$ near the donor star surface. Both these effects are negligible compared to the typical uncertainties ($\simeq 5 - 10\,{\rm km\,s^{-1}}$) on $v_{\rm grav}({\rm WD})$ and can be safely ignored.

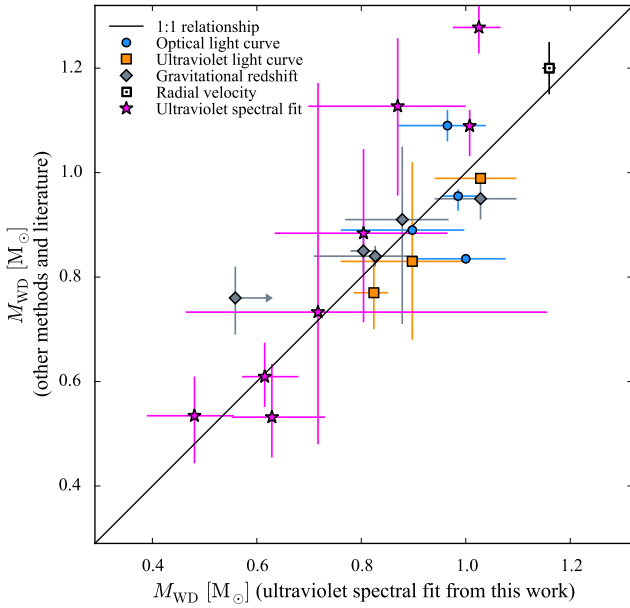By assuming the same mass-radius relationship as in Section 3.1.1

Figure 8. Comparison between the CV white dwarf masses derived in this work from the analysis of the ultraviolet *HST* spectra and those obtained employing other methods and from the analysis of the same ultraviolet data in the literature. The error bars show the corresponding 1σ uncertainties.

and using Equation 5, we measured the masses of the three CV white dwarfs, which result in $0.76^{+0.06}_{-0.07}\,M_\odot$, $0.95 \pm 0.04\,M_\odot$ and $0.91^{+0.14}_{-0.20}\,M_\odot$, for AX For, IR Com and V1108 Her, respectively (Table 6). In Section 4.1.3, we discuss these results in comparison with the masses obtained from the analysis of the ultraviolet spectra.

The accuracy we achieved on these measurements is directly related to the quality of the data. An optimal sampling of the orbital period is crucial to precisely measure radial velocities. This can be seen by comparing the results for IR Com with those for AX For and V1108 Her. The data of the former are almost evenly distributed along the orbital period and allow us to obtain accuracy of the order $\simeq 7$ per cent. However, the observations of AX For were affected by clouds while those of V1108 Her were contaminated by the presence of a close background star. In both cases, we were forced to reject some spectra, resulting in poor orbital sampling and larger uncertainties.

3.4 Summary on the mass measurements

The results of our fitting procedures are summarised in Table 5. In the case of the white dwarf in AX For, from the analysis of the ultraviolet data, we derived a smaller radius ($\simeq 0.0142\,R_\odot$) than the one estimated from the gravitational redshift ($\simeq 0.0190\,R_\odot$). We can thus roughly estimate that at the time of the *HST* observations $\simeq 77$ per cent of the white dwarf surface was still heated by the recent outburst and, therefore, we assumed as final measurements for its mass and radius those obtained from the gravitational redshift in Section 3.3.

We show in Figure 7 some examples of best-fitting models for three non-eclipsing systems in different temperature regimes, and for an eclipsing CV. All spectra, along with their best-fitting models, are available in Appendix B.

4 DISCUSSION

4.1 Comparison with previous mass measurements and different techniques

4.1.1 Eclipsing systems

Previous mass measurements from the analysis of the eclipse light curve of the white dwarf were obtained from optical observations for DV UMa, IY UMa, SDSS J103533.02+055158.4 and SDSS J150722.30+523039.8 (Savoury et al. 2011; McAllister et al. 2019), and from ultraviolet observations for DW UMa (Araujo-Betancor et al. 2003). Moreover, we here derived a mass measurement for IR Com and SDSS J150722.30+523039.8 from the analysis of their ultraviolet light curves (Section 3.1.1). We find a good agreement (within 3σ, Table 6 and Figure 8) between the masses derived employing the two different methods (ultraviolet spectral fit vs. analysis of the white dwarf eclipse).

4.1.2 Systems with previous mass measurements from ultraviolet analysis

For several systems in our sample (AM Her, BC UMa, BW Scl, EF Peg, EG Cnc, HV Vir, LL And and SW UMa), a mass estimate derived from the analysis of their ultraviolet *HST* data is available in the literature. However these studies lacked the knowledge of the distance to the systems and therefore did not provide a single mass estimate but a range of possible values, computed assuming different distances. The method employed is described in detail by Gänsicke et al. (2005) and consists of fitting the ultraviolet data by stepping through a grid of atmosphere models with fixed values for $\log(g)$, leaving the temperature and scaling factor free. In this way, it is possible to investigate the correlation between the assumed $\log(g)$ (i.e. the white dwarf mass under the assumption of a mass-radius relationship) and the best-fit value for $T_{\rm eff}$ (see e.g. figure 3 from Gänsicke et al. 2005) for different distances.

We retrieved the $\log(g)$-distance correlations for AM Her, BC UMa, BW Scl, EF Peg, EG Cnc, HV Vir, LL And and SW UMa from the works by Howell et al. (2002); Szkody et al. (2002a); Gänsicke et al. (2005, 2006). We applied a correction to account for the dependency of the mass-radius relationship on the white dwarf $T_{\rm eff}$ and for the reddening (see Appendix C for the details), which were not accounted for by these studies, and estimated the mass of the white dwarf assuming their distances from *Gaia* EDR3 (as described in Section 2.1.1). We computed the associated error bars by assuming a typical statistical uncertainty on the white dwarf temperature (for a fixed $\log(g)$) of $\simeq 200\,K$ (B.T. Gänsicke, private communications). For each object, we compared them with the systematic uncertainties derived in Section 3.2.1 (which are representative of the typical uncertainties related to the accuracy of the reddening and distance) and assumed as final uncertainties the larger between the two values. The final results are listed in Table 6 and shown in Figure 8.

With the exception of EG Cnc, the results from the literature are in good agreement with ours within the uncertainties. The origin of the disagreement in the case of EG Cnc is not easy to unveil and could possibly be related to the different atmosphere models used by Szkody et al. (2002a), which were generated with an older version of TLUSTY (# 195) than the one that we used (# 204n). The most relevant differences between the two versions are an improved treatment of H_2^+ quasi-molecular absorption lines (dominant in this cool CV) and of the Stark-broadening profiles using the calculation by Tremblay & Bergeron (2009). Therefore, we consider our results more reliable and representative of the observed flux emission of EG Cnc.

Table 5. White dwarf parameters and mass accretion rates for the 42 CVs observed with *HST* during their quiescent state and for AX For, whose radius and mass have been obtained from the white dwarf gravitational redshift.

| System	$P_{\rm orb}$ (min)	d (pc)	Z $Z_\odot$	References	$T_{\rm eff}$ (K)	$R_{\rm WD}$ (0.01 $R_\odot$)	$M_{\rm WD}$ ($M_\odot$)	$\log(g)$	$\langle \dot{M} \rangle$ ($10^{-10}\,M_\odot\,{\rm yr}^{-1}$)	White dwarf contribution (%)
SDSS J150722.30+523039.8	66.61	211 ± 4	0.1	1	$14\,207^{+356}_{-403}$	$0.93^{+0.17}_{-0.12}$	$0.90^{+0.10}_{-0.14}$	$8.45^{+0.16}_{-0.22}$	$0.53^{+0.18}_{-0.11}$	78
SDSS J074531.91+453829.5	76.0	310^{+23}_{-20}	0.1	2	$15\,447^{+556}_{-654}$	$1.1^{+0.3}_{-0.2}$	$0.75^{+0.18}_{-0.20}$	$8.2^{+0.3}_{-0.4}$	$1.2^{+0.7}_{-0.4}$	88
GW Lib	76.78	112.6 ± 0.8	0.2	3	$16\,166^{+253}_{-350}$	$1.03^{+0.15}_{-0.1}$	$0.83^{+0.08}_{-0.12}$	$8.33^{+0.13}_{-0.18}$	$1.12^{+0.32}_{-0.19}$	86
SDSS J143544.02+233638.7	78.0	208^{+9}_{-8}	0.01	3	$11\,997^{+99}_{-160}$	$1.00^{+0.08}_{-0.09}$	$0.84^{+0.07}_{-0.06}$	$8.36^{+0.11}_{-0.1}$	$0.32^{+0.08}_{-0.05}$	90
OT J213806.6+261957	78.1	98.9 ± 0.4	0.2	3	$15\,317^{+216}_{-228}$	$1.39^{+0.15}_{-0.12}$	$0.57^{+0.06}_{-0.07}$	$7.91^{+0.12}_{-0.15}$	$1.9^{+0.4}_{-0.3}$	73
BW Scl	78.23	93.4 ± 0.5	0.5	4	$15\,145^{+51}_{-57}$	$0.8^{+0.014}_{-0.011}$	$1.007^{+0.010}_{-0.012}$	$8.635^{+0.017}_{-0.02}$	$0.483^{+0.014}_{-0.012}$	87
LL And	79.28	609^{+343}_{-205}	1.0	5	$14\,353^{+1210}_{-743}$	$1.2^{+0.8}_{-0.6}$	$0.7^{+0.4}_{-0.3}$	8.2 ± 0.7	$0.9^{+2.4}_{-0.9}$	80
AL Com	81.6	523^{+252}_{-149}	0.2	6	$15\,840^{+1453}_{-1243}$	$1.0^{+0.9}_{-0.6}$	$0.9^{+0.5}_{-0.3}$	8.4 ± 0.8	$0.9^{+3.1}_{-1.0}$	79
WZ Sge	81.63	45.17 ± 0.06	0.01	7	$13\,190^{+115}_{-105}$	1.05 ± 0.03	0.8 ± 0.02	8.3 ± 0.04	$0.52^{+0.014}_{-0.01}$	78
SW UMa	81.81	$160.6^{+1.6}_{-1.5}$	0.2	4	$13\,854^{+189}_{-131}$	$1.29^{+0.09}_{-0.10}$	$0.61^{+0.06}_{-0.04}$	$8.01^{+0.11}_{-0.09}$	$1.07^{+0.15}_{-0.14}$	61
V1108 Her	81.87	148 ± 2	1.0	3	$13\,943^{+185}_{-226}$	$0.95^{+0.14}_{-0.11}$	$0.88^{+0.09}_{-0.11}$	$8.42^{+0.15}_{-0.17}$	$0.52^{+0.15}_{-0.11}$	75
ASAS J002511+1217.2	82.0	157 ± 3	0.1	3	$13\,208^{+154}_{-112}$	0.78 ± 0.04	1.02 ± 0.04	8.66 ± 0.07	$0.27^{+0.03}_{-0.02}$	74
HV Vir	82.18	317^{+29}_{-25}	0.2	8	$12\,958^{+257}_{-291}$	$0.96^{+0.21}_{-0.16}$	$0.87^{+0.13}_{-0.17}$	$8.4^{+0.2}_{-0.3}$	$0.4^{+0.2}_{-0.12}$	93
SDSS J103533.02+055158.4	82.22	195^{+12}_{-10}	0.01	3	$11\,876^{+108}_{-115}$	$0.8^{+0.11}_{-0.09}$	$1.00^{+0.08}_{-0.10}$	$8.63^{+0.14}_{-0.16}$	$0.18^{+0.06}_{-0.04}$	91
WX Cet	83.9	252^{+9}_{-8}	0.1	9	$15\,186^{+1460}_{-1468}$	$0.63^{+0.28}_{-0.18}$	$1.10^{+0.17}_{-0.21}$	8.8 ± 0.4	$0.3^{+0.07}_{-0.06}$	24
SDSS J075507.70+143547.6	84.76	239^{+12}_{-11}	0.5	3	$16\,193^{+280}_{-357}$	$0.92^{+0.15}_{-0.11}$	$0.91^{+0.09}_{-0.12}$	$8.47^{+0.15}_{-0.19}$	$0.87^{+0.27}_{-0.18}$	87
SDSS J080434.20+510349.2	84.97	142 ± 2	0.5	10	$13\,715^{+55}_{-79}$	$0.80^{+0.04}_{-0.03}$	$1.01^{+0.03}_{-0.04}$	$8.64^{+0.05}_{-0.06}$	0.32 ± 0.03	87
EK TrA	86.36	151.4 ± 0.8	0.5	11	$17\,608^{+269}_{-481}$	$0.97^{+0.17}_{-0.11}$	$0.87^{+0.09}_{-0.13}$	$8.4^{+0.14}_{-0.21}$	$1.4^{+0.4}_{-0.3}$	58
EG Cnc	86.36	186 ± 7	0.2	8	$12\,295^{+56}_{-57}$	$0.77^{+0.06}_{-0.05}$	$1.03^{+0.04}_{-0.05}$	$8.67^{+0.07}_{-0.08}$	$0.2^{+0.03}_{-0.02}$	100
1RXS J105010.8–140431	88.56	$108.9^{+1.1}_{-1.0}$	0.1	3	$11\,523^{+29}_{-47}$	$1.08^{+0.04}_{-0.03}$	$0.77^{+0.02}_{-0.03}$	$8.25^{+0.04}_{-0.05}$	$0.332^{+0.028}_{-0.018}$	87
BC UMa	90.16	293^{+11}_{-10}	0.2	4	$14\,378^{+272}_{-327}$	$1.57^{+0.19}_{-0.16}$	$0.48^{+0.08}_{-0.09}$	$7.73^{+0.15}_{-0.19}$	$2.0^{+0.5}_{-0.3}$	85
VY Aqr	90.85	$141.3^{+1.9}_{-1.8}$	0.5	9	$14\,453^{+316}_{-366}$	$0.74^{+0.07}_{-0.06}$	1.06 ± 0.06	$8.73^{+0.12}_{-0.11}$	$0.33^{+0.04}_{-0.03}$	45
QZ Lib	92.36	199^{+11}_{-10}	0.01	3	$11\,419^{+175}_{-229}$	$1.01^{+0.23}_{-0.18}$	$0.82^{+0.14}_{-0.19}$	$8.3^{+0.2}_{-0.3}$	$0.27^{+0.15}_{-0.09}$	74
SDSS J153817.35+512338.0	93.11	607^{+47}_{-40}	0.01	3	$35\,284^{+600}_{-688}$	$0.89^{+0.16}_{-0.12}$	$0.97^{+0.09}_{-0.11}$	$8.53^{+0.17}_{-0.2}$	$18.0^{+7.0}_{-4.0}$	100
UV Per	93.44	248^{+7}_{-6}	0.2	3	$14\,040^{+539}_{-645}$	$1.2^{+0.4}_{-0.3}$	0.7 ± 0.2	8.1 ± 0.4	$0.9^{+0.7}_{-0.4}$	69
1RXS J023238.8–371812	95.04	214^{+8}_{-7}	0.2	3	$14\,457^{+118}_{-135}$	$0.63^{+0.05}_{-0.04}$	1.15 ± 0.04	$8.9^{+0.07}_{-0.08}$	0.23 ± 0.03	71
RZ Sge	98.32	294 ± 7	0.5	3	$15\,197^{+419}_{-507}$	$1.09^{+0.27}_{-0.17}$	$0.78^{+0.13}_{-0.18}$	$8.3^{+0.2}_{-0.3}$	$1.0^{+0.5}_{-0.3}$	51
CY UMa	100.18	306 ± 6	0.1	3	$14\,692^{+471}_{-394}$	1.40 ± 0.13	$0.57^{+0.08}_{-0.06}$	$7.91^{+0.14}_{-0.13}$	1.6 ± 0.2	63
GD 552	102.73	80.6 ± 0.2	0.1	12	$10\,761^{+37}_{-43}$	$1.07^{+0.05}_{-0.04}$	$0.78^{+0.03}_{-0.04}$	$8.27^{+0.05}_{-0.06}$	$0.243^{+0.023}_{-0.018}$	55
IY UMa*	106.43	181 ± 2	1.0	3	$17\,057^{+179}_{-79}$	$0.83^{+0.04}_{-0.05}$	$0.99^{+0.04}_{-0.03}$	$8.59^{+0.07}_{-0.05}$	0.85 ± 0.07	79
SDSS J100515.38+191107.9	107.6	339^{+21}_{-19}	0.2	3	$14\,483^{+520}_{-430}$	$1.7^{+0.4}_{-0.3}$	$0.44^{+0.15}_{-0.09}$	7.6 ± 0.3	$2.4^{+1.2}_{-0.8}$	76
RZ Leo	110.17	279^{+12}_{-11}	0.5	3	$15\,573^{+437}_{-424}$	$0.85^{+0.2}_{-0.16}$	$0.97^{+0.13}_{-0.16}$	$8.6^{+0.2}_{-0.3}$	$0.62^{+0.3}_{-0.19}$	81
CU Vel	113.04	158.5 ± 1.1	0.1	3	$14\,174^{+117}_{-169}$	$1.58^{+0.11}_{-0.08}$	$0.47^{+0.04}_{-0.05}$	$7.71^{+0.08}_{-0.11}$	$1.97^{+0.28}_{-0.19}$	90
AX For	113.04	349 ± 10	1.0	3	–	$1.09^{+0.08}_{-0.09}$	0.76 ± 0.07	8.24 ± 0.08	–	–
EF Peg	120.53	288^{+21}_{-18}	0.2	5	$16\,644^{+448}_{-570}$	1.1 ± 0.2	$0.8^{+0.16}_{-0.17}$	8.3 ± 0.3	$1.3^{+0.5}_{-0.4}$	90
DV UMa*	123.62	382^{+24}_{-21}	1.0	3	$19\,410^{+244}_{-400}$	$0.86^{+0.12}_{-0.09}$	$0.96^{+0.07}_{-0.1}$	$8.55^{+0.13}_{-0.16}$	$1.5^{+0.4}_{-0.3}$	89
IR Com	125.34	216 ± 3	1.0	3	$17\,531^{+236}_{-271}$	$0.78^{+0.11}_{-0.08}$	$1.03^{+0.07}_{-0.09}$	$8.67^{+0.12}_{-0.15}$	$0.82^{+0.21}_{-0.15}$	87
AM Her	185.65	87.9 ± 0.2	0.001	13	$19\,248^{+486}_{-450}$	$1.3^{+0.17}_{-0.14}$	$0.63^{+0.1}_{-0.08}$	$8.01^{+0.17}_{-0.16}$	$4.0^{+0.9}_{-0.7}$	92
DW UMa	196.71	579^{+7}_{-6}	0.71	14	$56\,760^{+146}_{-259}$	$1.19^{+0.07}_{-0.05}$	$0.82^{+0.03}_{-0.04}$	$8.2^{+0.05}_{-0.07}$	228.0 ± 24.0	97
U Gem	254.74	93.0 ± 0.3	1.0	15	$33\,070^{+648}_{-616}$	0.634 ± 0.016	1.160 ± 0.013	8.90 ± 0.03	$6.53^{+0.22}_{-0.17}$	100
SS Aur	263.23	$249.0^{+1.8}_{-1.7}$	0.1	16	$28\,627^{+190}_{-269}$	$0.86^{+0.15}_{-0.11}$	$0.98^{+0.09}_{-0.11}$	$8.56^{+0.16}_{-0.19}$	$7.3^{+3.0}_{-1.9}$	100
RX And	302.25	196.7 ± 1.0	0.5	17	$33\,900^{+634}_{-995}$	$1.12^{+0.12}_{-0.08}$	$0.81^{+0.06}_{-0.08}$	$8.25^{+0.1}_{-0.13}$	$26.0^{+6.0}_{-4.0}$	100
V442 Cen	662.4	343 ± 5	0.01	16	$29\,802^{+211}_{-247}$	$1.35^{+0.14}_{-0.12}$	$0.64^{+0.06}_{-0.05}$	7.98 ± 0.12	$25.0^{+5.0}_{-4.0}$	100

Notes. For each object, its orbital period and metallicity are compiled from the literature. The last five columns report the results from this work. The two systems highlighted with a star are those for which the curtain of veiling gas has been detected in their ultraviolet spectra.

References. (1) Uthas et al. (2011), (2) Mukadam et al. (2013), (3) Pala et al. (2017), (4) Gänsicke et al. (2005), (5) Howell et al. (2002), (6) Szkody et al. (2003), (7) Sion et al. (1995), (8) Szkody et al. (2002a), (9) Sion et al. (2003), (10) Szkody et al. (2013), (11) Gänsicke et al. (2001), (12) Unda-Sanzana et al. (2008), (13) Gänsicke et al. (2006), (14) Araujo-Betancor et al. (2003), (15) Cheng et al. (1997), (16) Sion et al. (2008), (17) Sion et al. (2001).

Table 6. Summary of the CV white dwarf masses derived in this work from the analysis of the ultraviolet data and those obtained employing other methods. The systems are sorted by increasing masses.

System	M_{WD} ($M_\odot$)						References
	ultraviolet spectral fit (this work)	ultraviolet spectral fit (literature[a])	ultraviolet light curve	optical light curve	gravitational redshift	radial velocities	
BC UMa	$0.48^{+0.08}_{-0.09}$	$0.53^{+0.07}_{-0.09}$	–	–	–	–	Gänsicke et al. (2005)
AX For	$0.56 \uparrow$	–	–	–	$0.76^{+0.06}_{-0.07}$	–	This work
SW UMa	$0.61^{+0.06}_{-0.04}$	0.61 ± 0.6	–	–	–	–	Gänsicke et al. (2005)
AM Her	$0.63^{+0.10}_{-0.08}$	$0.53^{+0.10}_{-0.08}$	–	–	–	–	Gänsicke et al. (2006)
LL And	$0.7^{+0.4}_{-0.3}$	$0.7^{+0.4}_{-0.3}$	–	–	–	–	Howell et al. (2002)
EF Peg	$0.80^{+0.16}_{-0.17}$	$0.88^{+0.16}_{-0.17}$	–	–	–	–	Howell et al. (2002)
WZ Sge	0.80 ± 0.02	–	–	–	0.85 ± 0.04	–	Steeghs et al. (2007)
DW UMa	$0.82^{+0.03}_{-0.04}$	–	0.77 ± 0.07	–	–	–	Araujo-Betancor et al. (2003)
GW Lib	$0.83^{+0.08}_{-0.12}$	–	–	–	0.84 ± 0.02	–	van Spaandonk et al. (2010)
J150722.30+523039.8	$0.90^{+0.10}_{-0.14}$	–	$0.83^{+0.19}_{-0.15}$	0.89 ± 0.01	–	–	Ultraviolet light curve, this work; optical light curve Savoury et al. (2011)
V1108 Her	$0.88^{+0.09}_{-0.11}$	–	–	–	$0.91^{+0.14}_{-0.20}$	–	This work
DV UMa	$0.96^{+0.07}_{-0.10}$	–	–	1.09 ± 0.03	–	–	McAllister et al. (2019)
IY UMa	$0.99^{+0.04}_{-0.03}$	–	–	$0.955^{+0.013}_{-0.028}$	–	–	McAllister et al. (2019)
SDSS J103533.02+055158.4	$1.00^{+0.08}_{-0.10}$	–	–	0.835 ± 0.009	–	–	Savoury et al. (2011)
BW Scl	$1.007^{+0.01}_{-0.012}$	$1.10^{+0.03}_{-0.06}$	–	–	–	–	Gänsicke et al. (2005)
IR Com	$1.03^{+0.07}_{-0.09}$	–	0.989 ± 0.003	–	0.95 ± 0.04	–	This work
U Gem	1.16 ± 0.013	–	–	–	–	1.2 ± 0.05	Echevarría et al. (2007)
HV Vir	$0.87^{+0.13}_{-0.17}$	$1.27^{+0.13}_{-0.17}$	–	–	–	–	Szkody et al. (2002a)
EG Cnc	$1.03^{+0.04}_{-0.05}$	$1.28^{+0.04}_{-0.05}$	–	–	–	–	Szkody et al. (2002a)

Notes. (a) The reported values have been corrected accounting for the temperature dependency of the mass-radius relationship and the reddening, as discussed in Section 4.1.2
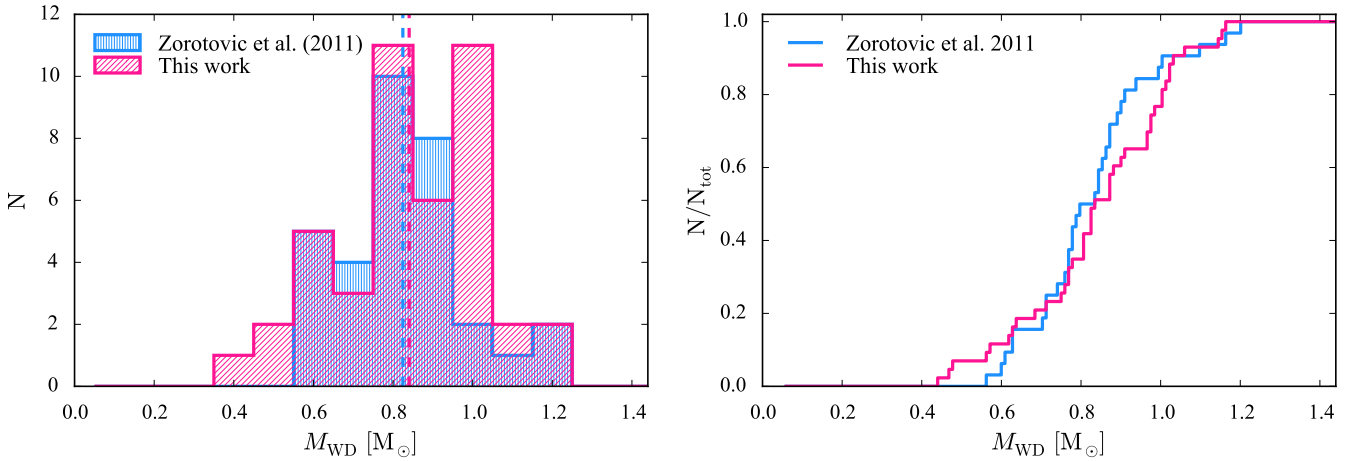
Figure 9. Comparison between the mass distributions (left) and the cumulative distributions (right) of the 43 white dwarfs from this work (pink) and the 32 measurements compiled by Zorotovic et al. (2011, blue). The dashed vertical lines correspond to the average masses. Our results show the presence of a tail extending to low masses corresponding to helium-core white dwarfs, which is not detected in the sample studied by Zorotovic et al. (2011).

4.1.3 Systems with radial velocity measurements

For three systems in our sample, AX For, IR Com and V1108 Her, we derived an independent mass measurement from the white dwarf gravitational redshift (Section 3.3). Moreover, additional mass measurements, which have been determined from the gravitational redshift of the white dwarfs in GW Lib (van Spaandonk et al. 2010)

and WZ Sge (Steeghs et al. 2007), and from the radial velocities of the two stellar components in U Gem (Echevarría et al. 2007), are available in the literature (see also Table D1 and references therein). These masses are all in good agreement with those we derived from the spectral fit to the ultraviolet data (Table 6 and Figure 8).
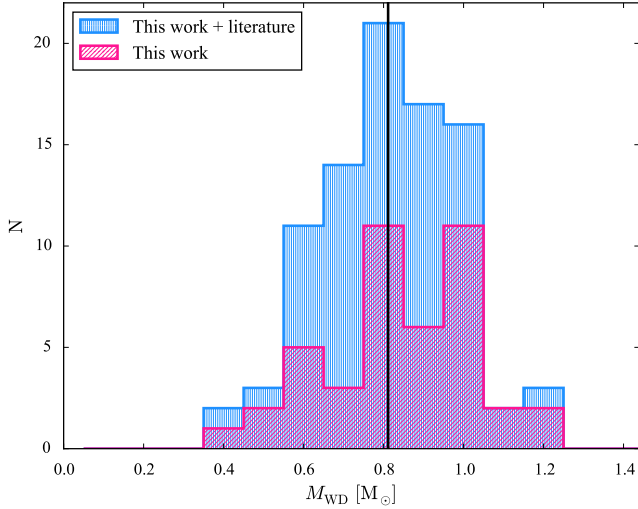
Figure 10. Mass distribution for the sample of 89 CV white dwarfs obtained combining the 43 mass measurements from this work (shown in pink) with the 46 from the literature. The black vertical line corresponds to the average mass of the total sample of 89 systems, $\langle M_{\rm WD} \rangle = 0.81^{+0.16}_{-0.20}\,{\rm M}_\odot$.

Figure 11. White dwarf masses from this work (circles) and from the literature (diamonds), as a function of their orbital periods. Long period ($P_{\rm orb} > 3\,{\rm hr}$) and short ($P_{\rm orb} < 3\,{\rm hr}$) period CVs are shown in blue and pink, respectively. The right panel shows the corresponding distributions and the corresponding average masses (dashed lines), colour coded as in the left panel. Note that long period CVs have, on average, secular mass accretion rates about one order of magnitude higher compared to those of short period CVs, as reported in the figure.

4.2 Comparison with Zorotovic et al. (2011)

Figure 9 shows the comparison between the 43 mass measurement from this work and the compilation from Zorotovic et al. (2011), which includes 22 masses derived from the analysis of the white dwarf eclipses and 10 measurements from spectroscopic studies. The two samples have eight systems in common (AM Her, DV UMa, DW UMa, IY UMa, SDSS J103533.02+055158.4, SDSS J150722.30+523039.8, U Gem and WZ Sge, see Table 6) and this partial overlap highlights possible differences associated with the different methods employed to measure the masses of the white dwarfs.

The mass distribution we derived presents a tail extending towards low masses, consisting of three systems (BC UMa, CU Vel and SDSS J100515.38+191107.9) with $M_{\rm WD} < 0.5\,{\rm M}_\odot$. Such low masses are consistent with either He core or, possibly, hybrid CO/He core white dwarfs. In contrast, the sample studied by Zorotovic et al. (2011) does not contain any white dwarf with $M_{\rm WD} < 0.5\,{\rm M}_\odot$ although, from evolutionary considerations, they estimated that CV helium-core white dwarfs should represent $\lesssim 10$ per cent of the systems.

For both distributions, we determined the average white dwarf mass $\langle M_{\rm WD} \rangle$ and the corresponding uncertainties as the 16th and the 84th percentiles, obtaining $\langle M_{\rm WD} \rangle = 0.82 \pm 0.12\,{\rm M}_\odot$ for the values from Zorotovic et al. (2011) and $\langle M_{\rm WD} \rangle = 0.84^{+0.18}_{-0.23}$ for the masses here derived. The agreement between these values allows us to rule out the presence of any systematics affecting the masses derived from the analysis of eclipse light curves.

4.3 The mass distribution of CV white dwarfs

Since the work by Zorotovic et al. (2011), more mass measurements of CV white dwarfs have been made available in the literature, mainly thanks to the systematic observations of eclipsing systems (e.g. Littlefair et al. 2006; Feline et al. 2005; Savoury et al. 2011; McAllister et al. 2019) with the fast triple-beam camera ULTRACAM (Dhillon et al. 2007). A more comprehensive and up-to-date census of masses in the litera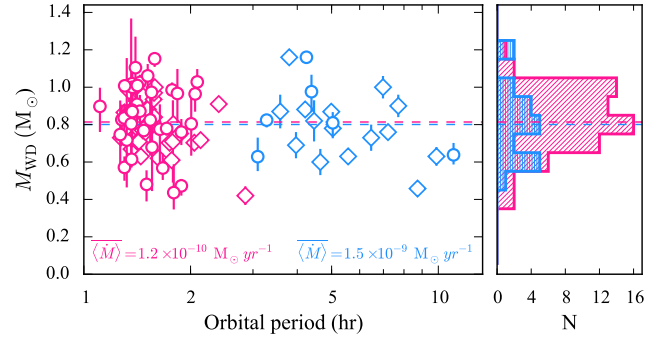ture consists of 54 measurements (see Table D1 and reference therein), eight of which (AM Her, DV UMa, DW UMa, SDSS J103533.02+055158.4, SDSS J150722.30+523039.8, U Gem WZ Sge and IY UMa, see Table 6) are in common with our sample. For these systems, we here assume the white dwarf parameters obtained in this work. Of the remaining 46 CV white dwarf masses from the literature, 34 have been derived from the analysis of the eclipse light curves of the white dwarf and 12 from spectroscopic studies.

Combining these 46 measurements with our results, we obtained a sample of 89 CV white dwarfs with an accurate mass, and the corresponding average mass results $\langle M_{\rm WD} \rangle = 0.81^{+0.16}_{-0.20}\,{\rm M}_\odot$ (Figure 10). As demonstrated by Zorotovic et al. (2011), this high average mass of CV white dwarfs cannot be ascribed to an observational bias since the detection of massive white dwarfs is disfavoured by the fact that they have smaller radii and are less luminous than low mass white dwarfs for the same $T_{\rm eff}$. This confirms the earlier results that CV white dwarfs are genuinely more massive than predicted by most models of CV evolution, which only account for orbital angular momentum losses arising from magnetic braking and gravitational wave radiation.

Among the systems from the literature, two (HY Eri and KIC 5608384) have $M_{\rm WD} < 0.5\,{\rm M}_\odot$. These, combined with the three low-mass primaries likely representative of He-core white dwarfs we have identified, bring the total census to five systems. On the one hand, compared to the standard models for CV evolution, the number of observed He-core white dwarfs is still far lower than predicted (e.g. $\simeq 53$ per cent, Politano 1996 and $\simeq 30$ per cent, Goliasch & Nelson 2015 of the present-day CV population). On the other hand, more modern scenarios that take into account a mass dependent consequential angular momentum loss and that can reproduce the overall white dwarf mass distribution in CVs do not predict any He-core white dwarfs (e.g. Schreiber et al. 2016), which is also in contrast with the observations. Our result shows that CVs hosting low mass white dwarfs contribute to the overall CV population and that their non-zero fraction should be properly taken into account in the modelling of CV evolution.
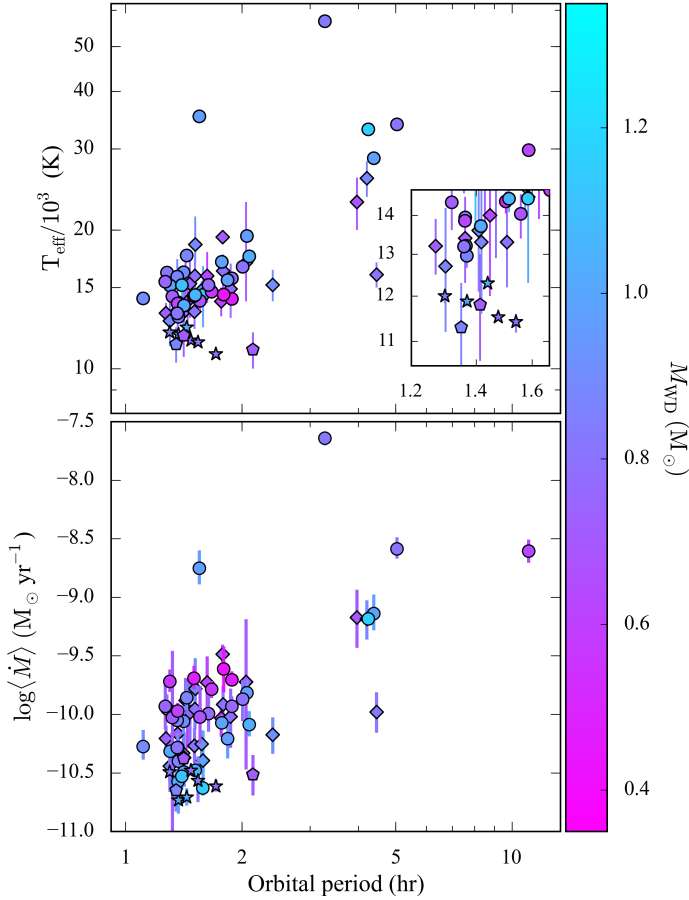
Figure 12. Effective temperatures (top) and mass accretion rates (bottom) as a function of the orbital period, for the systems in our *HST* sample (circles for pre-bounce and stars for period bounce CVs) and those from the literature (diamonds for pre-bounce and pentagons for period bounce CVs). The inset shows a closeup of the period bounce systems.

4.4 Orbital period dependecy

While losing orbital angular momentum, CVs evolve from long to short orbital periods and, by comparing the average mass of the white dwarfs in long ($P_{orb} > 3$ hr) and short ($P_{orb} < 3$ hr) period CVs, we can investigate possible overall variations (due to either mass growth or mass erosion) with time. We do not find any difference between the average white dwarfs mass of long ($\langle M_{WD} \rangle = 0.80^{+0.17}_{-0.19}$ M$_\odot$) and short ($\langle M_{WD} \rangle = 0.81^{+0.17}_{-0.16}$ M$_\odot$) period CVs. Moreover, by performing an F-test on the best linear fit to the masses as a function of the orbital period, we derive an F-statistic $F_0 = 2.22$ with p-value $= 0.23$ and therefore we do not find any evidence for a clear dependency on the white dwarf mass with the orbital period (Figure 11). Nonetheless, only 21 long period CVs have mass determinations (in contrast to the 68 systems at short orbital periods) and additional measurements at long orbital periods are required to further constrain any correlation.

4.5 Mass accretion rates and CV evolution

The evolution of CVs is dictated by orbital angular momentum losses, which continuously shrink the orbit and keep the secondary in touch with its Roche lobe, ensuring the stability of the mass transfer process. For systems with $P_{orb} \gtrsim 3$ h, the main mechanisms of angular

momentum loss are magnetic wind braking and gravitational wave radiation. As the system loses orbital angular momentum, the two stellar components spiral inwards and the system evolves towards short orbital periods, while the donor star is constantly stripped of more and more mass. At $P_{orb} \simeq 3$ h, the donor star has become fully convective and, in the frequently referenced interrupted magnetic braking scenario (Rappaport et al. 1983; Paczynski & Sienkiewicz 1983; Spruit & Ritter 1983), a re-configuration of the magnetic fields takes place on the donor, leading to a great reduction in the efficiency of magnetic braking. As a consequence, the secondary star detaches from its Roche-lobe and, in the period range 2 h $\lesssim P_{orb} \lesssim 3$ h (the so-called period gap) the system evolves as a detached binary whilst still losing angular momentum through gravitational wave radiation. Accretion then resumes at $P_{orb} \simeq 2$ h, when the orbital separation brings again the donor in contact with its Roche-lobe, and the system keep evolving towards shorter orbital periods. When the system reaches the "period minimum" at $P_{orb} \simeq 80$ min, the time-scale on which the secondary star loses mass becomes much shorter than its thermal time-scale and the secondary stops shrinking in response to the mass loss. Consequently, systems that have passed the period minimum evolve back towards longer orbital periods and, for this reason, are called "period bouncers".

The different efficiencies of magnetic braking and gravitational wave radiation in removing angular momentum from the binary orbit cause long period CVs to have $\langle \dot{M} \rangle$ about one order of magnitude higher compared to those of short period CVs. Determining the rate of angular momentum loss is therefore important in order to test the models of CV evolution. However, a direct measurement via detection of orbital period changes is impossible on human time scales. A very good proxy for the angular momentum loss rate is the white dwarf effective temperature (Townsley & Bildsten 2003), as it is determined by the compressional heating of the accreted material (Sion 1995; Townsley & Bildsten 2004). Therefore, T_{eff} provides a constraint on the mean mass-accretion rate $\langle \dot{M} \rangle$, averaged over the thermal time-scale of the white dwarf envelope ($10^3 - 10^5$ yr), which is a direct measurement of the angular momentum loss rate in the system (Townsley & Gänsicke 2009).

An accurate determination of the mass accretion rate requires the knowledge of both T_{eff} and M_{WD}:

$$L_{WD} = 4\pi R_{WD}^2 \sigma T_{eff}^4 = 6\times10^{-3} L_\odot \left(\frac{\langle \dot{M} \rangle}{10^{-10} M_\odot \text{yr}^{-1}} \right) \left(\frac{M_{WD}}{0.9 M_\odot} \right)^{0.4} \tag{6}$$

where L is the luminosity and σ is the Stefan-Boltzmann constant (eq. 1 from Townsley & Gänsicke 2009). Thanks to the accurate parallaxes provided by *Gaia*, we have been able to measure both parameters and the mass accretion rates reported in Tables 5 and D1 can then be used to test and constrain the current models of CV evolution.

Figure 12 shows the effective temperatures (top) and the mass accretion rates (bottom) as a function of the orbital period for 65 systems, 41 from our *HST* sample[9] (circles and stars) and 34 from the literature (diamonds and pentagons), for which both T_{eff} and M_{WD} are available. We find that systems above the gap are hotter

---

[9] The evolution of CVs hosting magnetic white dwarfs is different compared to that of non-magnetic CVs, as there are evidence of the reduction of magnetic braking efficiency due to the coupling of the secondary and the white dwarf magnetic fields (Belloni et al. 2020). Our *HST* sample contains one strongly magnetised CV white dwarf (AM Her) which we do not include in the discussion.
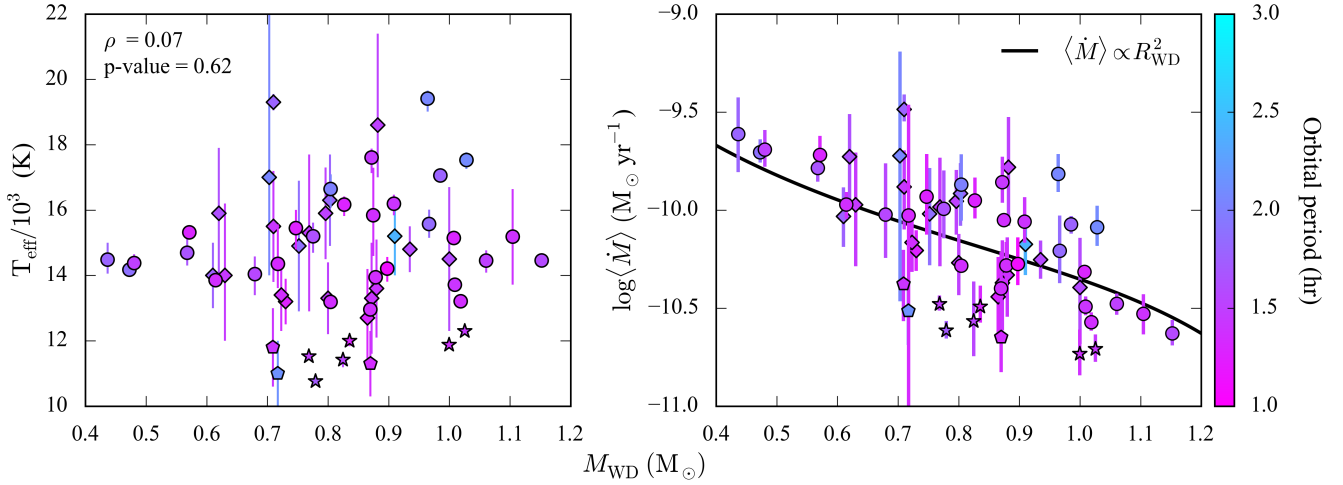
Figure 13. For systems at short orbital periods ($P_{\rm orb} < 3$ hr), the white dwarf effective temperatures show no clear dependency on the white dwarf mass (left). Consequently, the relation between the mass accretion rates and the mass of the white dwarf (right) is dominated by the mass-radius relationship ($\langle \dot{M} \rangle \propto R_{\rm WD}^2$, solid black line, arbitrarily normalised so that $\langle \dot{M} \rangle = 7 \times 10^{-11} {\rm M_\odot yr^{-1}}$ for $M_{\rm WD} = 0.8\,{\rm M_\odot}$). The data are colour-coded according to the orbital periods and the symbol convention is the same as in Figure 12.

and accrete at higher rates than systems below the gap, reflecting the different rates of angular momentum loss driving the evolution of these binaries in different orbital period regimes.

Two outliers clearly stand out: SDSS J153817.35+512338.0 ($P_{\rm orb} = 93.11$ min) and DW UMa ($P_{\rm orb} = 196.71$ min), which are both much hotter than the other CV white dwarfs at similar orbital periods. As already suggested by Pala et al. (2017), SDSS J153817.35+512338.0 could be a young CV which just formed at this orbital period and is undergoing a phase of high mass accretion rate that is expected to occur at the onset of the mass transfer (D'Antona et al. 1989). An alternative possibility is a CV that recently experienced a nova eruption and the white dwarf has not cooled down yet. DW UMa is a member of the nova-like CV subclass[10], which dominates the population of CVs in the $3-4$ hours period range. Possibly, also the high temperature and mass accretion rate of DW UMa, and those of nova-likes in general, could be related to their young ages if CVs are preferentially formed in the $3-4$ h $P_{\rm orb}$ range (Townsley & Gänsicke 2009). This could be the case if the initial mass ratio distribution of main sequence binaries peaks toward equal masses (de Kool 1992). Alternatively, nova-likes could arise naturally from systems close to the regime of unstable mass transfer (Goliasch & Nelson 2015), where the mass of the donor star is similar to the white dwarf mass. These two outliers are not considered in the following discussion since their effective temperatures possibly reflect peculiar stages of their evolution.

Below the period gap, two branches are visible. One is composed of systems with $T_{\rm eff} \geq 12\,500$ K, whose temperatures and mass accretion accretion rates decrease as the systems evolve towards the period minimum. The second branch consists of the period bounce CVs, which are evolving towards longer orbital periods and can be easily recognised as such thanks to their effective temperatures being

---

[10] Effective temperatures obtained during a low state are available for other two nova-like CVs, TT Ari ($P_{\rm orb} = 198.07$ min, $T_{\rm eff} = 39\,000$ K, Gänsicke et al. 1999) and MV Lyr ($P_{\rm orb} = 191.38$ min, $T_{\rm eff} = 47\,000$ K, Hoard et al. 2004). Similarly to DW UMa, both systems are much hotter than other CV white dwarfs at similar orbital periods. However, TT Ari and MV Lyr lack of an accurate mass measurement and therefore they have not been included in this analysis.

$\simeq 3000 - 4000$ K lower than those of the pre-bounce CVs at similar orbital periods (see the inset in the top panel of Figure 12). We identify seven previously known period bouncers (EG Cnc, Patterson 2011; GD 552, Unda-Sanzana et al. 2008; SDSS J103533.02+055158.4, Littlefair et al. 2006; SDSS J150240.98+333423.9, McAllister et al. 2017b; 1RXS J105010.8–140431, Patterson 2011; Pala et al. 2017, QZ Lib, Pala et al. 2018 and V455 And Patterson 2011) and two new period bounce CVs, SDSS J143544.02+233638.7 and CTCV J1300–3052. The fraction of period bouncers is thus (13 ± 4) per cent, consistent with that derived by Pala et al. (2020) from the analysis of a volume-limited sample of CVs ($7 - 14$ per cent).

We also noticed three additional weaker candidates (WZ Sge, SDSS J080434.20+510349.2 and SDSS J123813.73–033932.9), which are all known to host brown-dwarf companions (Howell et al. 2004; Zharikov et al. 2013; Pala et al. 2019). However, these white dwarfs are slightly hotter ($T_{\rm eff} \simeq 13\,000$ K) than other confirmed period bouncers and, since they are located right at the period minimum, it is difficult to asses whether they have already bounced back or not.

For the short period systems, we found that the white dwarf effective temperatures show a very weak dependence on the masses, i.e. systems hosting white dwarfs spanning a wide range in masses ($0.4 - 1.2\,{\rm M_\odot}$) all have very similar temperatures (left panel in Figure 13). From the statistical point of view, this is confirmed by the Pearson coefficient $\rho = 0.07$ and p-value = 0.62 of the distribution. In contrast, the mass accretion rates appear to be anti-correlated with the white dwarf mass. Note that, for a given $\langle \dot{M} \rangle$, $T_{\rm eff}$ increases as the layer of accreted material builds up to the next classical nova eruption (Townsley & Bildsten 2004). Below the period gap, the expected range of variation of $T_{\rm eff}$ is of the order of ± 1000 K and implies that the combination of $T_{\rm eff}$ and $M_{\rm WD}$ via Equation 6 does not provide a single value for $\langle \dot{M} \rangle$, but rather a range of possible mass accretion rates with a flat probability distribution. Nonetheless, this effect is not large enough (see e.g. figure 10 from Townsley & Bildsten 2004) to explain the scatter observed in the left panel of Figure 13. In contrast, the $\langle \dot{M} \rangle - M_{\rm WD}$ dependency directly descends from the white dwarf mass-radius relationship. Given that the quiescence luminosity is very weakly dependent on the white dwarf mass (Equation 6), it follows that $L \propto \langle \dot{M} \rangle \propto R_{\rm WD}^2 T_{\rm eff}^4$. Therefore $\langle \dot{M} \rangle \propto R_{\rm WD}^2$, since

$T_{\rm eff}$ is observed to have no clear dependence on the mass. For comparison, this dependency is plotted as the solid black line in the left panel in Figure 13, which has been computed using the mass-radius relationship of Holberg & Bergeron (2006); Tremblay et al. (2011) and has been arbitrarily normalised so that $\langle \dot{M} \rangle = 7 \times 10^{-11} {\rm M}_\odot {\rm yr}^{-1}$ for $M_{\rm WD} = 0.8 \, {\rm M}_\odot$.

This behaviour differs significantly from the predictions of the classical models of CV evolution, which assume that, in this period range, angular momentum is mainly removed by gravitational wave radiation. This mechanism implies higher accretion rates (and hence higher effective temperatures) for larger white dwarf masses because the (i) the rate of gravitational wave radiation is directly proportional to the masses of the two stellar components in the system, and (ii) $R_{\rm WD}$ is smaller for more massive white dwarf while the surface luminosity is not strongly dependent on $M_{\rm WD}$ and thus $T_{\rm eff} \propto R_{\rm WD}^{-2}$ (Townsley & Bildsten 2004). For comparison with this model, in the left panels of Figure 14, we show our results against various evolutionary tracks computed with MESABINARY (revision 15140) assuming magnetic wind braking and gravitational wave radiation above the period gap, and gravitational wave radiation only below the period gap, for different initial white dwarf masses. For completeness, these models also account for the loss of angular momentum associated with mass ejection following a classical nova eruption (assuming that all the accreted material is ejected), which is, however, negligible compared to magnetic wind braking and gravitational wave radiation. The models cover a much wider range in temperatures than the observations and predict a strong correlation between the white dwarf effective temperature and mass, with more massive CV white dwarfs being hotter than their less massive counterparts. They also imply lower accretion rates than observed and a direct correlation between the accretion rates and the white dwarf mass, i.e. CVs hosting more massive white dwarfs have higher accretion rates. Moreover, the evolutionary tracks underestimate the location of the period minimum and are not able to reproduce the observed temperatures of period bounce CVs. This is also the case for similar evolutionary models available in the literature (see e.g. figure 3 from Howell et al. 2001 or figure 2 from Goliasch & Nelson 2015), which in general predict that all systems, soon after the onset of mass transfer, will converge into a narrow track in the $\langle \dot{M} \rangle - P_{\rm orb}$ plane, with a very weak dependence on their masses.

These theoretical results are in contrast with our findings, which suggest that the classical recipe of CV evolution needs to be revised in order to explain the absence of a clear dependency of the effective temperature on the white dwarf mass. The effective temperature is set by the secular mass accretion rate onto the white dwarf which, in turn, reflects the rate of angular momentum loss in the system. Therefore, our results suggest that the missing ingredient of the theoretical modelling causing low mass CV white dwarfs to be hotter than predicted by the classical recipes (and to have similar effective temperature to their more massive counterparts, left panel of Figure 13) is an additional source of angular momentum loss which is more efficient the lower the mass of the white dwarf (right panel of Figure 13).

Such a dependency of the angular momentum loss rate on the white dwarf mass is the fundamental concept of the eCAML prescription developed by Schreiber et al. (2016) and Belloni et al. (2018, 2020) and already discussed in Section 1. This model includes an empirically mass-dependent additional source of angular momentum loss that better accounts for the observed dependency of the accretion rates on the white dwarf mass and better reproduces the observed temperatures and mass accretion rates (right panels in Figure 14) than the classical models. The enhanced angular momentum loss

leads to a faster erosion of the donor star, causing the systems to bounce at longer orbital periods. Consequently, the period minimum predicted by eCAML is anticipated compared to the standard prediction and agrees better with the observations. Moreover, without requiring any additional fine-tuning, eCAML is also able to solve other disagreements that, for long time, have been found between the standard model of CV evolution and the observed properties of the CV population (such as their space density, and orbital period and mass distributions Schreiber et al. 2016; Belloni et al. 2020; Pala et al. 2020).

Despite the significant progress that is provided by the eCAML prescription, our observations provide reasons for improving this model in order to account for (i) the observed scatter in the parameters, (ii) the period bounce systems, for which the models predict a steep decrease in their effective temperatures that is not observed in data (which, instead, suggest the presence of enhanced angular momentum loss also in the post-bounce regime, as previously discussed also by Pala et al. 2017, 2020), and (iii) the presence of helium-core white dwarfs. The difference between the null fraction of helium white dwarfs predicted by eCAML and the observations is not as dramatic as in the case of the former estimates from more classical evolutionary models (see also Section 4.3). Our results suggest that some low mass systems can survive (at least for some time) in a semi-detached configuration, thus providing valuable observational constraints to further refine this model and thereby help to understand the physical mechanism that is driving the additional angular momentum loss.

Different authors have suggested that an additional source of angular momentum loss that is more efficient the lower the mass of the white dwarf could arise from friction between the binary and the shell of ejected material following a nova eruptions (Schreiber et al. 2016; Nelemans et al. 2016; Sparks & Sion 2021). To further investigate this possibility, our observational and theoretical understanding of classical novae and their impact on the secular evolution of CVs need to be improved.

Finally, additional issues are observed for systems above the period gap. The 3-4 h period range is mainly populated by the unexpectedly hot nova-likes CVs (which have already been discussed in the first part of this Section) while, at $P_{\rm orb} \gtrsim 4 \, {\rm h}$, CV white dwarfs are found to be systematically colder than predicted. This is a long-standing issue in our understanding of compact binary evolution (Knigge et al. 2011; Pala et al. 2017) and, as discussed in great detail by Townsley & Gänsicke (2009) and Belloni et al. (2020), could be related to either inaccurate modelling of magnetic wind braking (the dominant angular momentum loss mechanism driving the evolution of the systems in this period range) or incomplete understanding of the heating of the white dwarf as a consequence of the mass accretion process (for example, owing to the presence of long-term mass-transfer rate fluctuations associated with the secondary, to which long period CVs would be more susceptible than short-period systems, Knigge et al. 2011). However, the limited number of available measurements (eight) severely limits any conclusions we can draw in this period range and more observations are needed to increase the number of systems with accurate parameters above the period gap.

5 CONCLUSIONS

We analysed high quality *HST* ultraviolet spectra for 42 CVs. Making use of the astrometry delivered by the ESA *Gaia* space mission in its EDR3, we accurately measured the white dwarf effective temperatures and masses. We complemented this sample with an additional
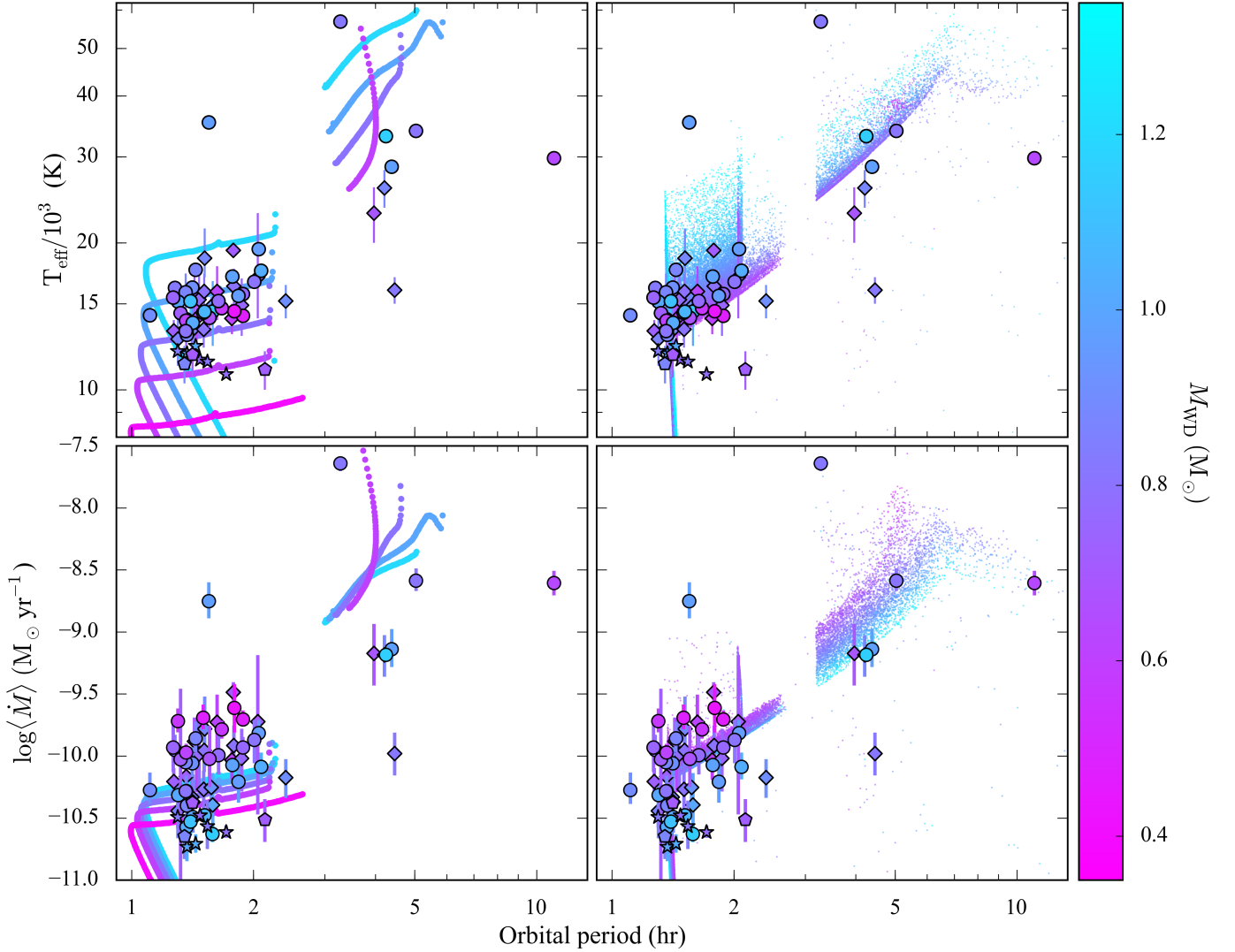
Figure 14. Effective temperatures (top) and mass accretion rates (bottom) as a function of the orbital period, for the systems in our *HST* sample (circles for pre-bounce and stars for period bounce CVs) and those from the literature (diamonds for pre-bounce and pentagons for period bounce CVs). For a comparison with the models, we show the theoretically predicted values for the classical recipe for CV evolution (left panels, see the text for more details) and for eCAML (right panels, small dots), as computed by Belloni et al. (2020). Observations and theoretical values are colour-coded according to the white dwarf mass. The MESA tracks have been computed assuming the following combination for the masses of the white dwarf and the donor (top to bottom): $M_{WD} = 1.2 \, M_\odot$ and $M_2 = 0.8 \, M_\odot$; $M_{WD} = 1.0 \, M_\odot$ and $M_2 = 0.8 \, M_\odot$; $M_{WD} = 0.8 \, M_\odot$ and $M_2 = 0.6 \, M_\odot$; $M_{WD} = 0.6 \, M_\odot$ and $M_2 = 0.5 \, M_\odot$; $M_{WD} = 0.4 \, M_\odot$ and $M_2 = 0.3 \, M_\odot$.

mass measurement for the white dwarf in AX For, obtained from its gravitational redshift. Our results are in good agreement with independent measurements obtained from analysis of the white dwarf eclipses and from radial velocity studies.

Combining our results with the effective temperatures and masses for 46 CV white dwarfs from the literature, we assembled the largest sample of systems with accurate white dwarf parameters. We derived an average white dwarf mass of $\langle M_{WD} \rangle = 0.81^{+0.16}_{-0.20} \, M_\odot$, in perfect agreement with former results, which allows us to definitively rule out any systematics affecting the masses derived from the analysis of eclipse light curves. In our mass distribution, we identify a tail extending towards low masses, consisting of five systems with $M_{WD} < 0.5 \, M_\odot$. Such low masses are consistent with either He core or, possibly, hybrid CO/He core white dwarfs.

The white dwarf response to the mass accretion process and its capability to retain the accreted mass are of key interest in the context of Type Ia Supernova (SNe Ia) progenitors. If the mass transfer

process can lead to the mass growth of the white dwarf, CVs could represent a possible channel for SN Ia explosions. By comparing the average mass of the white dwarfs in long ($P_{orb} > 3$ hr) and short ($P_{orb} < 3$ hr) period CVs, we do not find any evidence for a clear dependency on the white dwarf mass with the orbital period. However, additional measurements at long orbital periods are required to further constrain any correlation.

Thanks to the accurate parallaxes provided by *Gaia*, we have been able to measure both the white dwarf masses and temperatures. The combination of these parameters allows us to derive the secular mean of the mass accretion rates onto the white dwarf, which can be used to test and constrain the current models of CV evolution. For CVs at short orbital periods ($P_{orb} < 3$ hr), we show an anti-correlation between the mass accretion rates and the mass of the white dwarf, which implies the presence of an additional mechanism of angular momentum loss that is more efficient the lower the mass of the white dwarf. This finding is in very good agreement with the predictions

of the recently proposed eCAML prescription. Including an empirically mass-dependent additional source of angular momentum loss, eCAML is able to explain the observed high average mass of CV white dwarfs and also to solve other disagreements between theory and observations, including the CV space density and orbital period distribution. The eCAML model provides an improved understanding of the observational properties of CVs and our results provide observational support for it. Some disagreement between eCAML and the observations still need to be addressed, like the observed scatter in the parameters and the presence of helium-core white dwarfs. Nonetheless, we highlight that the difference between the null fraction predicted by eCAML and the observations is not as dramatic as in the case of the former estimates from more classical evolutionary models. Our results suggest that some low mass systems can survive (at least for some time) in a semi-detached configuration, thus providing valuable observational constraints to understand the physical mechanism that is driving the additional angular momentum loss.

Finally, an additional discrepancy between theory and observations is noticeable for the period bounce systems, for which the models predict a steep decrease in their $T_{\rm eff}$ and $\langle \dot{M} \rangle$ that is not observed in data, which, instead, suggest the presence of enhanced angular momentum loss also in the post-bounce regime.

DATA AVAILABILITY

All data underlying this article is publicly available from the relevant observatory archive or will be shared on reasonable request to the corresponding author.

REFERENCES

Araujo-Betancor S., et al., 2003, ApJ, 583, 437
Ashley R. P., et al., 2020, MNRAS,
Bailer-Jones C. A. L., 2015, PASP, 127, 994
Bailer-Jones C. A. L., Rybizki J., Fouesneau M., Demleitner M., Andrae R., 2021, AJ, 161, 147
Belloni D., Schreiber M. R., Zorotovic M., Iłkiewicz K., Hurley J. R., Giersz M., Lagos F., 2018, MNRAS, 478, 5626
Belloni D., Schreiber M. R., Pala A. F., Gänsicke B. T., Zorotovic M., Rodrigues C. V., 2020, MNRAS, 491, 5717
Beuermann K., 2006, A&A, 460, 783
Beuermann K., Burwitz V., Reinsch K., Schwope A., Thomas H. C., 2020, A&A, 634, A91
Cardelli J. A., Clayton G. C., Mathis J. S., 1989, ApJ, 345, 245
Cassatella A., Altamore A., González-Riestra R., 2005, A&A, 439, 205
Cheng F. H., Sion E. M., Horne K., Hubeny I., Huang M., Vrtilek S. D., 1997, AJ, 114, 1165
Copperwheat C. M., Marsh T. R., Dhillon V. S., Littlefair S. P., Hickman R., Gänsicke B. T., Southworth J., 2010, MNRAS, 402, 1824
D'Antona F., Mazzitelli I., Ritter H., 1989, A&A, 225, 391
Dhillon V. S., et al., 2007, MNRAS, 378, 825
Echevarría J., de la Fuente E., Costero R., 2007, AJ, 134, 262
Echevarría J., Smith R. C., Costero R., Zharikov S., Michel R., 2008, MNRAS, 387, 1563
Echevarría J., Ramírez-Torres A., Michel R., Hernández Santisteban J. V., 2016, MNRAS, 461, 1576
Eggleton P. P., 1983, ApJ, 268, 368
Epelstain N., Yaron O., Kovetz A., Prialnik D., 2007, MNRAS, 374, 1449
Feline W. J., Dhillon V. S., Marsh T. R., Watson C. A., Littlefair S. P., 2005, MNRAS, 364, 1158
Foreman-Mackey D., Hogg D. W., Lang D., Goodman J., 2013, PASP, 125, 306
Freudling W., Romaniello M., Bramich D. M., Ballester P., Forchi V., García-Dabló C. E., Moehler S., Neeser M. J., 2013, A&A, 559, A96
Fuchs J. T., et al., 2016, MNRAS, 462, 2382
Gänsicke B. T., Koester D., 1999, A&A, 346, 151
Gänsicke B. T., Sion E. M., Beuermann K., Fabian D., Cheng F. H., Krautter J., 1999, A&A, 347, 178
Gänsicke B. T., Szkody P., Sion E. M., Hoard D. W., Howell S., Cheng F. H., Hubeny I., 2001, A&A, 374, 656
Gänsicke B. T., et al., 2003, ApJ, 594, 443
Gänsicke B. T., Szkody P., Howell S. B., Sion E. M., 2005, ApJ, 629, 451
Gänsicke B. T., Long K. S., Barstow M. A., Hubeny I., 2006, ApJ, 639, 1039
Gänsicke B. T., Koester D., Farihi J., Toloza O., 2018, MNRAS, 481, 4323
Gehrz R. D., Truran J. W., Williams R. E., Starrfield S., 1998, PASP, 110, 3
Godon P., Sion E. M., Cheng F. H., Szkody P., Long K. S., Froning C. S., 2004, ApJ, 612, 429
Goliasch J., Nelson L., 2015, ApJ, 809, 80
Green G. M., Schlafly E., Zucker C., Speagle J. S., Finkbeiner D., 2019, ApJ, 887, 93
Greenstein J. L., Trimble V., 1967, AJ, 72, 301
Hameury J.-M., Menou K., Dubus G., Lasota J.-P., Hure J.-M., 1998, MNRAS, 298, 1048
Harrison T. E., McNamara B. J., Szkody P., Gilliland R. L., 2000, AJ, 120, 2649
Harrison T. E., Johnson J. J., McArthur B. E., Benedict G. F., Szkody P., Howell S. B., Gelino D. M., 2004, AJ, 127, 460
Heise J., Verbunt F., 1988, A&A, 189, 112
Hernandez M. S., Zharikov S., Neustroev V., Tovmassian G., 2017, MNRAS, 470, 1960
Hessman F. V., Gänsicke B. T., Mattei J. A., 2000, A&A, 361, 952
Hillman Y., Prialnik D., Kovetz A., Shara M. M., 2016, ApJ, 819, 168
Hillman Y., Shara M. M., Prialnik D., Kovetz A., 2020, Nature Astronomy, 4, 886
Hoard D. W., Linnell A. P., Szkody P., Fried R. E., Sion E. M., Hubeny I., Wolfe M. A., 2004, ApJ, 604, 346
Holberg J. B., Bergeron P., 2006, AJ, 132, 1221

Horne K., Welsh W. F., Wade R. A., 1993, ApJ, 410, 357
Horne K., Marsh T. R., Cheng F. H., Hubeny I., Lanz T., 1994, ApJ, 426, 294
Howell S. B., Nelson L. A., Rappaport S., 2001, ApJ, 550, 897
Howell S. B., Gänsicke B. T., Szkody P., Sion E. M., 2002, ApJ, 575, 419
Howell S. B., Harrison T. E., Szkody P., 2004, ApJ, 602, L49
Hubeny I., 1988, Computer Physics Communications, 52, 103
Hubeny I., Lanz T., 1995, ApJ, 439, 875
Ivanova N., et al., 2013, A&ARv, 21, 59
Kausch W., et al., 2015, A&A, 576, A78
Kepler S. O., Kleinman S. J., Nitta A., Koester D., Castanheira B. G., Giovannini O., Costa A. F. M., Althaus L., 2007, MNRAS, 375, 1315
Kippenhahn R., Thomas H. C., 1978, A&A, 63, 265
Knigge C., Long K. S., Hoard D. W., Szkody P., Dhillon V. S., 2000, ApJ, 539, L49
Knigge C., Baraffe I., Patterson J., 2011, ApJS, 194, 28
Koester D., Schulz H., Weidemann V., 1979, A&A, 76, 262
La Dous C., 1991, A&A, 252, 100
Lallement R., et al., 2018, A&A, 616, A132
Liebert J., et al., 2005, AJ, 129, 2376
Lindegren L., Lammers U., Hobbs D., O'Mullane W., Bastian U., Hernández J., 2012, A&A, 538, A78
Lindegren L., et al., 2020, arXiv e-prints, p. arXiv:2012.03380
Littlefair S. P., Dhillon V. S., Marsh T. R., Gänsicke B. T., Southworth J., Watson C. A., 2006, Science, 314, 1578
Littlefair S. P., Dhillon V. S., Gänsicke B. T., Bours M. C. P., Copperwheat C. M., Marsh T. R., 2014, MNRAS, 443, 718
Livio M., Pringle J. E., 1994, ApJ, 427, 956
Long K. S., Gilliland R. L., 1999, ApJ, 511, 916
Long K. S., Blair W. P., Bowers C. W., Davidsen A. F., Kriss G. A., Sion E. M., Hubeny I., 1993, ApJ, 405, 327
Long K. S., Sion E. M., Gänsicke B. T., Szkody P., 2004, ApJ, 602, 948
Long K. S., Brammer G., Froning C. S., 2006, ApJ, 648, 541
Luri X., et al., 2018, preprint, (arXiv:1804.09376)
Maza J., Gonzalez L. E., 1983, IAU Circ., 3854
McAllister M. J., et al., 2015, MNRAS, 451, 114
McAllister M. J., et al., 2017a, MNRAS, 464, 1353
McAllister M. J., et al., 2017b, MNRAS, 467, 1024
McAllister M., et al., 2019, MNRAS, 486, 5535
Mestel L., 1968, MNRAS, 138, 359
Meyer F., Meyer-Hofmeister E., 1984, A&A, 132, 143
Mukadam A. S., et al., 2013, AJ, 146, 54
Mukadam A. S., Szkody P., Gänsicke B. T., Pala A., 2017, in Tremblay P. E., Gaensicke B., Marsh T., eds, Astronomical Society of the Pacific Conference Series Vol. 509, 20th European White Dwarf Workshop. p. 341
Naylor T., Allan A., Long K. S., 2005, MNRAS, 361, 1091
Nelemans G., Siess L., Repetto S., Toonen S., Phinney E. S., 2016, ApJ, 817, 69
Osaki Y., 1974, PASJ, 26, 429
Paczyński B., 1967, Acta Astron., 17, 287
Paczynski B., 1976, in Eggleton P., Mitton S., Whelan J., eds, IAU Symposium Vol. 73, Structure and Evolution of Close Binary Systems. p. 75
Paczynski B., Sienkiewicz R., 1983, The Astrophysical Journal, 268, 825
Pala A. F., et al., 2017, MNRAS, 466, 2855
Pala A. F., Schmidtobreick L., Tappert C., Gänsicke B. T., Mehner A., 2018, MNRAS, 481, 2523
Pala A. F., et al., 2019, MNRAS, 483, 1080
Pala A. F., et al., 2020, MNRAS, 494, 3799
Parsons S. G., et al., 2012, MNRAS, 419, 304
Patterson J., 2011, MNRAS, 411, 2695
Politano M., 1996, ApJ, 465, 338
Pretorius M. L., Knigge C., O'Donoghue D., Henry J. P., Gioia I. M., Mullis C. R., 2007, MNRAS, 382, 1279
Rappaport S., Verbunt F., Joss P. C., 1983, ApJ, 275, 713
Raymond J. C., Black J. H., Davis R. J., Dupree A. K., Gursky H., Hartmann L., Matilsky T. A., 1979, ApJ, 230, L95
Ritter H., 1987, Mem. Soc. Astron. Italiana, 58, 133
Ritter H., Burkert A., 1986, A&A, 158, 161

Rodríguez-Gil P., et al., 2007, MNRAS, 377, 1747
Rodríguez-Gil P., et al., 2015, MNRAS, 452, 146
Savoury C. D. J., et al., 2011, MNRAS, 415, 2025
Schenker K., King A. R., Kolb U., Wynn G. A., Zhang Z., 2002, MNRAS, 337, 1105
Schreiber M. R., Zorotovic M., Wijnen T. P. G., 2016, MNRAS, 455, L16
Schreiber M. R., Belloni D., Gänsicke B. T., Parsons S. G., Zorotovic M., 2021, Nature Astronomy,
Sion E. M., 1995, ApJ, 438, 876
Sion E. M., 1999, PASP, 111, 532
Sion E. M., Cheng F. H., Long K. S., Szkody P., Gilliland R. L., Huang M., Hubeny I., 1995, ApJ, 439, 957
Sion E. M., Cheng F. H., Sparks W. M., Szkody P., Huang M., Hubeny I., 1997, ApJ, 480, L17
Sion E. M., Cheng F. H., Szkody P., Sparks W., Gänsicke B., Huang M., Mattei J., 1998, ApJ, 496, 449
Sion E. M., Szkody P., Gaensicke B., Cheng F. H., La Dous C., Hassall B., 2001, ApJ, 555, 834
Sion E. M., Szkody P., Cheng F., Gänsicke B. T., Howell S. B., 2003, ApJ, 583, 907
Sion E. M., Gänsicke B. T., Long K. S., Szkody P., Knigge C., Hubeny I., deMartino D., Godon P., 2008, ApJ, 681, 543
Smette A., et al., 2015, A&A, 576, A77
Smith A. J., Haswell C. A., Hynes R. I., 2006, MNRAS, 369, 1537
Sparks W. M., Sion E. M., 2021, ApJ, 914, 5
Spruit H. C., Ritter H., 1983, A&A, 124, 267
Starrfield S., Bose M., Iliadis C., Hix W. R., Woodward C. E., Wagner R. M., 2020, ApJ, 895, 70
Steeghs D., Howell S. B., Knigge C., Gänsicke B. T., Sion E. M., Welsh W. F., 2007, ApJ, 667, 442
Szkody P., 1985, AJ, 90, 1837
Szkody P., 1987, AJ, 94, 1055
Szkody P., Gänsicke B. T., Sion E. M., Howell S. B., 2002a, ApJ, 574, 950
Szkody P., Gänsicke B. T., Howell S. B., Sion E. M., 2002b, ApJ, 575, L79
Szkody P., Gänsicke B. T., Sion E. M., Howell S. B., Cheng F. H., 2003, AJ, 126, 1451
Szkody P., et al., 2011, AJ, 142, 181
Szkody P., Mukadam A. S., Sion E. M., Gänsicke B. T., Henden A., Townsley D., 2013, AJ, 145, 121
Szkody P., et al., 2017, AJ, 153, 123
Taylor M. B., 2005, TOPCAT & STIL: Starlink Table/VOTable Processing Software. p. 29
Templeton M. R., 2007, AAVSO Alert Notice, 349
Thoroughgood T. D., Dhillon V. S., Watson C. A., Buckley D. A. H., Steeghs D., Stevenson M. J., 2004, MNRAS, 353, 1135
Thoroughgood T. D., et al., 2005, MNRAS, 357, 881
Thorstensen J. R., 2003, AJ, 126, 3017
Toloza O., et al., 2016, MNRAS, 459, 3929
Townsley D. M., Bildsten L., 2003, The Astrophysical Journal, 596, L227
Townsley D. M., Bildsten L., 2004, ApJ, 600, 390
Townsley D. M., Gänsicke B. T., 2009, The Astrophysical Journal, 693, 1007
Tremblay P. E., Bergeron P., 2009, in Hubeny I., Stone J. M., MacGregor K., Werner K., eds, American Institute of Physics Conference Series Vol. 1171, Recent Directions in Astrophysical Quantitative Spectroscopy and Radiation Hydrodynamics. pp 101–108, doi:10.1063/1.3250051
Tremblay P. E., Bergeron P., Gianninas A., 2011, ApJ, 730, 128
Unda-Sanzana E., et al., 2008, MNRAS, 388, 889
Uthas H., Knigge C., Long K. S., Patterson J., Thorstensen J., 2011, MNRAS, 414, L85
Verbunt F., Zwaan C., 1981, A&A, 100, L7
Vernet J., Dekker H., D'Odorico et al., 2011, A&A, 536, A105
Warner B., 1973, MNRAS, 162, 189
Warner B., 1995, Cambridge Astrophysics Series, 28
Welsh W. F., Froning C. S., Marsh T. R., Reimer T. W., Robinson E. L., Wood P. R., 2007, in Kang Y. W., Lee H. W., Leung K. C., Cheng K. S., eds, Astronomical Society of the Pacific Conference Series Vol. 362, The Seventh Pacific Rim Conference on Stellar Astrophysics. p. 241
Wijnen T. P. G., Zorotovic M., Schreiber M. R., 2015, A&A, 577, A143

Wild J. F., et al., 2021, arXiv e-prints, p. arXiv:2107.07400

Yaron O., Prialnik D., Shara M. M., Kovetz A., 2005, ApJ, 623, 398

York D. G., et al., 2000, AJ, 120, 1579

Yu Z., et al., 2019, MNRAS, 489, 1023

Zhang E. H., Robinson E. L., 1987, ApJ, 321, 813

Zharikov S., Tovmassian G., Aviles A., Michel R., Gonzalez-Buitrago D., García-Díaz M. T., 2013, A&A, 549, A77

Zorotovic M., Schreiber M. R., 2017, MNRAS, 466, L63

Zorotovic M., Schreiber M. R., Gänsicke B. T., 2011, A&A, 536, A42

de Kool M., 1992, A&A, 261, 188

van Spaandonk L., Steeghs D., Marsh T. R., Parsons S. G., 2010, ApJ, 715, L109

Figure A2. *HST*/COS light curve of GW Lib obtained over three consecutive spacecraft orbits, the gaps result from the target being occulted by the Earth. The red dots highlights the exposures from which the spectrum of GW Lib has been extracted.
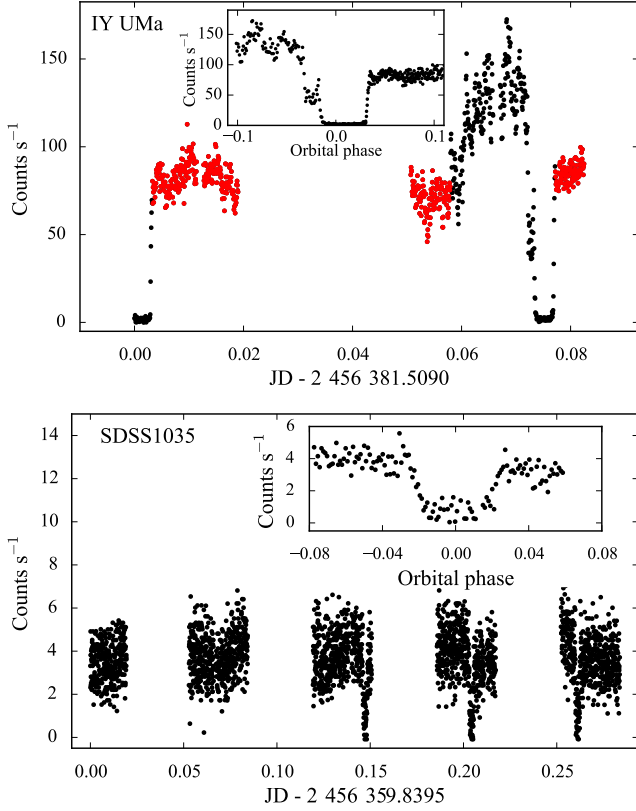
Figure A1. *HST*/COS light curves of some of the two eclipsing systems in our sample for which a fit to the eclipse light curve was not possible. In the case of IY UMa (top panel), the red dots highlight the regions that have been used to extract the spectrum of the system, when the emission was not dominated by the bright spot and the white dwarf was not eclipsed. The inset show the phase-folded light curve. Three white dwarf eclipses were detected in the light curve of SDSS J103533.02+055158.4 (bottom panel). Their average light curve is shown in the inset. However, the data quality is too poor to allow for an accurate mass determination of the white dwarf.

Figure A3. *HST*/STIS light curve of AM Her from the TIME-TAG data (top panel). The bottom panel shows the data phase-folded using the ephemeris reported by Heise & Verbunt (1988). Two cycles are plotted for clarity. The red dots highlights the exposures from which the spectrum of AM Her has been extracted.

APPENDIX A: VARIABLE SYSTEMS

A0.1 Eclipsing systems

Among the four eclipsing CVs, a fit to the eclipse light curve was only possible in the case of IR Com and SDSS J150722.30+523039.8 (Section 3.1.1). Although three eclipses of the white dwarf in SDSS J103533.02+055158.4 were observed in its COS light curve, their count level is too low (bottom panel of Figure A1) to accurately resolve the ingress and egress of the white dwarf, thus preventing an accurate mass determination.

Ideally, in systems in which the bright spot strongly contributes, multiple light curve eclipses are required in order to correctly time the ingress and egress of the white dwarf. Unfortunately, in the case of IY UMa, only one full eclipse was observed during the *HST* observations and, therefore, an accurate mass determination is not possible from the TIME–TAG data of this system. In the light curves of IY UMa, the hump observed just before the eclipse arises from the bright spot coming into view. To minimise the contamination from the bright spot emission for the analysis in Section 3.2, we extracted the spectrum out of eclipse and when the bright spot is not dominant (top panel of Figure A1).

A0.2 Brightenings

During the COS observations, GW Lib underwent a brightening event (Figure A2). This phenomenon has been studied in detailed by Toloza et al. (2016), who suggested that it could be associated with a fluctuation in the mass accretion rate. The brightening is related to the increase in temperature in a region covering up to ≃ 30 per cent of the white dwarf surface (Toloza et al. 2016). Since the presence of this hot spot could alter our mass measurement, we used the *split-corr* and *x1dcorr* routine to extract the spectrum corresponding to the first spacecraft orbit, when the hot region covers only ≃ 2 per cent of the white dwarf surface (see fig. 6 from Toloza et al. 2016). This spectrum is used later in this work to measure the mass of the white dwarf as it is the most representative of the quiescent phase of the system.

A0.3 AM Her

AM Her is the prototype for the class of CVs known as polars. The *HST*/STIS light curve of AM Her is characterised by a strong quasi-sinusoidal orbital flux modulation which, as discussed in great detail by Gänsicke et al. (2006), is associated with the hot polar cap on the rotating white dwarf coming into view (Figure A3). The flat part of the light curve corresponds to the times when the heated pole cap is self-eclipsed by the body of the white dwarf and we used the *inttag* routine from the *calstis* pipeline to split the observations into shorter exposures. Using the *calstis x1d* routine, we extracted the spectrum corresponding to the minimum of the modulation (red dots in Figure A3), which was then analysed to in Section 3.2.

A0.4 CVs hosting pulsating white dwarfs

1RXS J023238.8–371812 and SDSS J075507.70+143547.6 both contain a white dwarf pulsating with a period of $\simeq 267.5$ s (Mukadam et al. 2017). The pulsation is visible as a modulation in the COS light curve with an amplitude of $\simeq 5$ counts/s, too low to allow the extraction of a trough spectrum in a similar fashion as done for GW Lib. Therefore, we analysed their averaged ultraviolet spectrum obtained from summing the data from all orbits.

APPENDIX B: FIT RESULTS

In the following, for each object, we present a table summarising the best-fitting parameters and a plot showing the best-fitting model (red) to the corresponding *HST* data (black). The grey bands mask the geocoronal emission lines of Lyα (1216 Å) and, whenever present, of O I (1302 Å). The systems are sorted according to their orbital periods.

Table B1. Best-fitting parameters for SDSS J150722.30+523039.8.

Instrument	COS/STIS
Observation date	2010 Feb 18
$E(B-V)$ (mag)	$0.018^{+0.006}_{-0.018}$
$P_{\rm orb}$ (min)	66.61
Gaia EDR3 ID	1593140224924964864
ϖ (mas)	4.73 ± 0.09
d (pc)	211 ± 4
Z ($Z_\odot$)	0.1
$T_{\rm eff}$ (K)	14207^{+356}_{-403}
$R_{\rm WD}$ ($0.01\,R_\odot$)	$0.93^{+0.17}_{-0.12}$
$M_{\rm WD}$ ($M_\odot$)	$0.90^{+0.10}_{-0.14}$
$\log(g)$	$8.45^{+0.16}_{-0.22}$
$\langle \dot{M} \rangle$ ($10^{-10}\,M_\odot\,{\rm yr}^{-1}$)	$0.53^{+0.18}_{-0.11}$
WD contribution	78%

Figure B1. Ultraviolet *HST* spectra (black) of SDSS J150722.30+523039.8 along with the best-fitting model (red), computed as described in Section 3.2.

Table B2. Best-fitting parameters for SDSS J074531.91+453829.5.

Instrument	COS
Observation date	2012 Mar 13
$E(B-V)$ (mag)	0.027 ± 0.017
P_{orb} (min)	76.0
Gaia EDR3 ID	927255749553754880
ϖ (mas)	3.2 ± 0.2
d (pc)	310^{+23}_{-20}
Z ($Z_\odot$)	0.1
T_{eff} (K)	15447^{+556}_{-654}
R_{WD} ($0.01\,R_\odot$)	$1.1^{+0.3}_{-0.2}$
M_{WD} ($M_\odot$)	$0.75^{+0.18}_{-0.20}$
$\log(g)$	$8.2^{+0.3}_{-0.4}$
$\langle \dot{M} \rangle$ ($10^{-10}\,M_\odot\,\mathrm{yr}^{-1}$)	$1.2^{+0.7}_{-0.4}$
WD contribution	88%

Figure B2. Ultraviolet *HST* spectra (black) of SDSS J074531.91+453829.5 along with the best-fitting model (red), computed as described in Section 3.2.

Table B3. Best-fitting parameters for GW Lib.

Instrument	COS
Observation date	2013 May 30
$E(B-V)$ (mag)	0.022 ± 0.018
P_{orb} (min)	76.78
Gaia EDR3 ID	6226943645600487552
ϖ (mas)	8.88 ± 0.06
d (pc)	112.6 ± 0.8
Z ($Z_\odot$)	0.2
T_{eff} (K)	16166^{+253}_{-350}
R_{WD} ($0.01\,R_\odot$)	$1.03^{+0.15}_{-0.1}$
M_{WD} ($M_\odot$)	$0.83^{+0.08}_{-0.12}$
$\log(g)$	$8.33^{+0.13}_{-0.18}$
$\langle \dot{M} \rangle$ ($10^{-10}\,M_\odot\,\mathrm{yr}^{-1}$)	$1.12^{+0.32}_{-0.19}$
WD contribution	86%

Figure B3. Ultraviolet *HST* spectra (black) of GW Lib along with the best-fitting model (red), computed as described in Section 3.2.

Table B4. Best-fitting parameters for SDSS J143544.02+233638.7.

Instrument	COS
Observation date	2013 Mar 09
$E(B-V)$ (mag)	0.02 ± 0.02
P_{orb} (min)	78.0
Gaia EDR3 ID	1242828982729309952
ϖ (mas)	4.8 ± 0.2
d (pc)	208^{+9}_{-8}
Z ($Z_\odot$)	0.01
T_{eff} (K)	11997^{+99}_{-160}
R_{WD} ($0.01\,R_\odot$)	$1.00^{+0.08}_{-0.09}$
M_{WD} ($M_\odot$)	$0.84^{+0.07}_{-0.06}$
$\log(g)$	$8.36^{+0.11}_{-0.1}$
$\langle \dot{M} \rangle$ ($10^{-10}\,M_\odot\,yr^{-1}$)	$0.32^{+0.08}_{-0.05}$
WD contribution	90%

Figure B4. Ultraviolet *HST* spectra (black) of SDSS J143544.02+233638.7 along with the best-fitting model (red), computed as described in Section 3.2.

Table B5. Best-fitting parameters for OT J213806.6+261957.

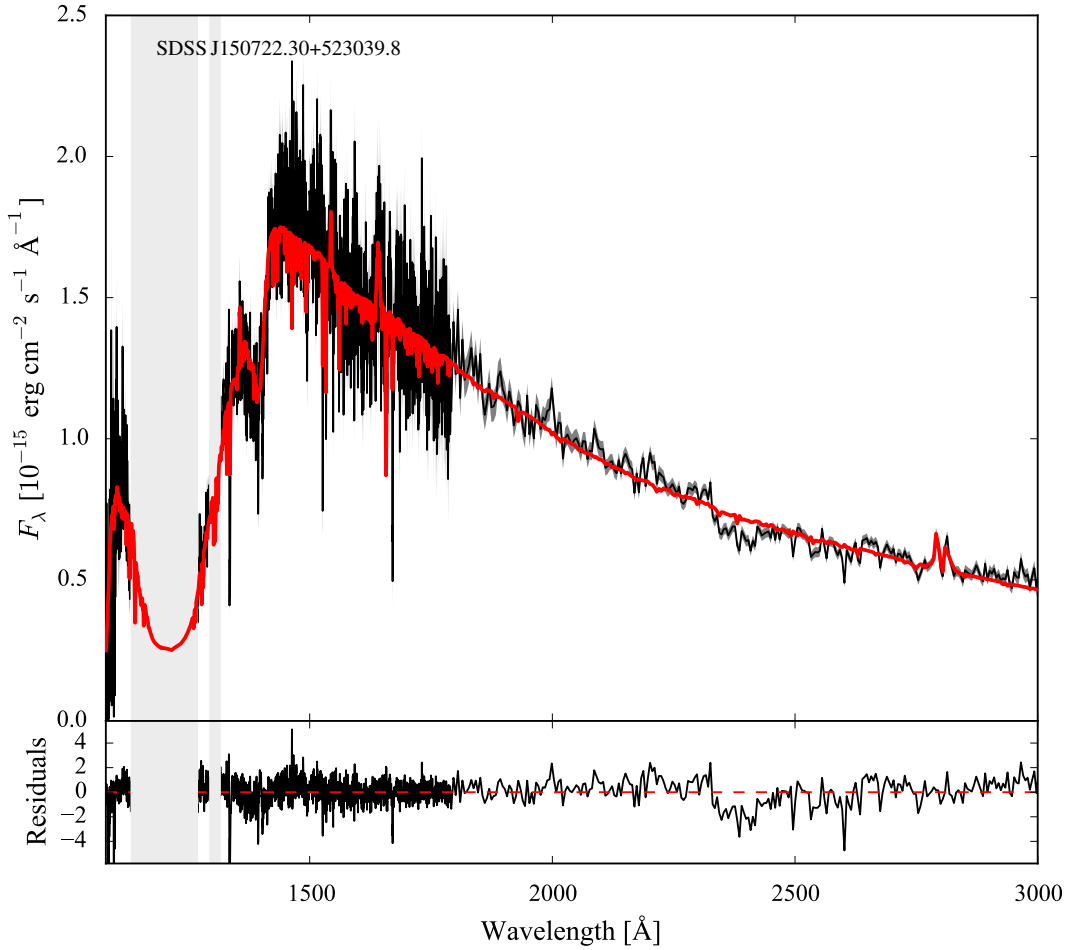| Instrument	COS
Observation date	2013 Jul 25
$E(B-V)$ (mag)	0.017 ± 0.015
$P_{\rm orb}$ (min)	78.1
Gaia EDR3 ID	1800384942558699008
ϖ (mas)	10.11 ± 0.04
d (pc)	98.9 ± 0.4
Z ($Z_\odot$)	0.2
$T_{\rm eff}$ (K)	15317^{+216}_{-228}
$R_{\rm WD}$ ($0.01\,R_\odot$)	$1.39^{+0.15}_{-0.12}$
$M_{\rm WD}$ ($M_\odot$)	$0.57^{+0.06}_{-0.07}$
$\log(g)$	$7.91^{+0.12}_{-0.15}$
$\langle \dot{M} \rangle$ ($10^{-10}\,M_\odot\,{\rm yr}^{-1}$)	$1.9^{+0.4}_{-0.3}$
WD contribution	73%

Figure B5. Ultraviolet *HST* spectra (black) of OT J213806.6+261957 along with the best-fitting model (red), computed as described in Section 3.2.

Table B6. Best-fitting parameters for BW Scl.

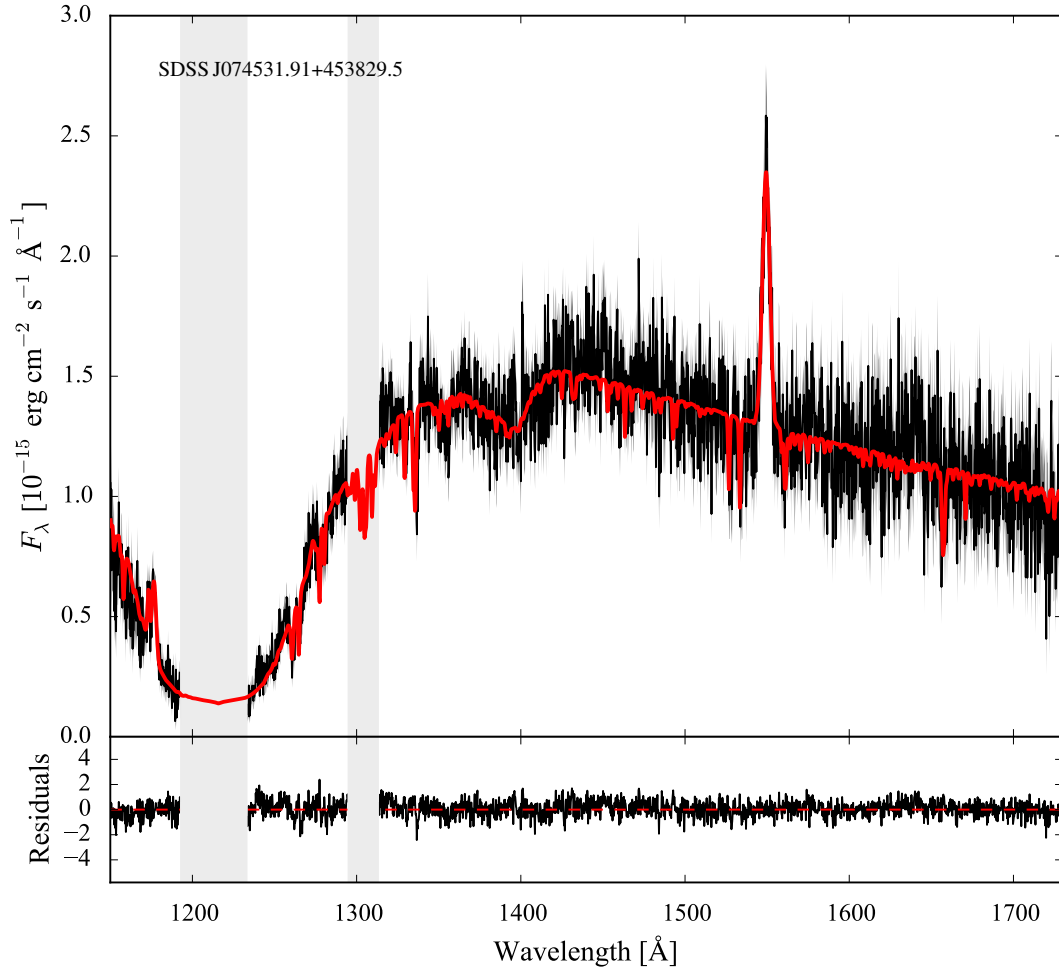| Instrument	STIS
Observation date	2006 Dec 27
$E(B-V)$ (mag)	$0.002^{+0.015}_{-0.002}$
P_{orb} (min)	78.23
Gaia EDR3 ID	2307289214897332480
ϖ (mas)	10.71 ± 0.05
d (pc)	93.4 ± 0.5
Z ($Z_\odot$)	0.5
T_{eff} (K)	15145^{+51}_{-57}
R_{WD} ($0.01\,R_\odot$)	$0.8^{+0.014}_{-0.011}$
M_{WD} ($M_\odot$)	$1.007^{+0.010}_{-0.012}$
$\log(g)$	$8.635^{+0.017}_{-0.02}$
$\langle \dot{M} \rangle$ ($10^{-10}\,M_\odot\,yr^{-1}$)	$0.483^{+0.014}_{-0.012}$
WD contribution	87%

Figure B6. Ultraviolet *HST* spectra (black) of BW Scl along with the best-fitting model (red), computed as described in Section 3.2.

Table B7. Best-fitting parameters for LL And.

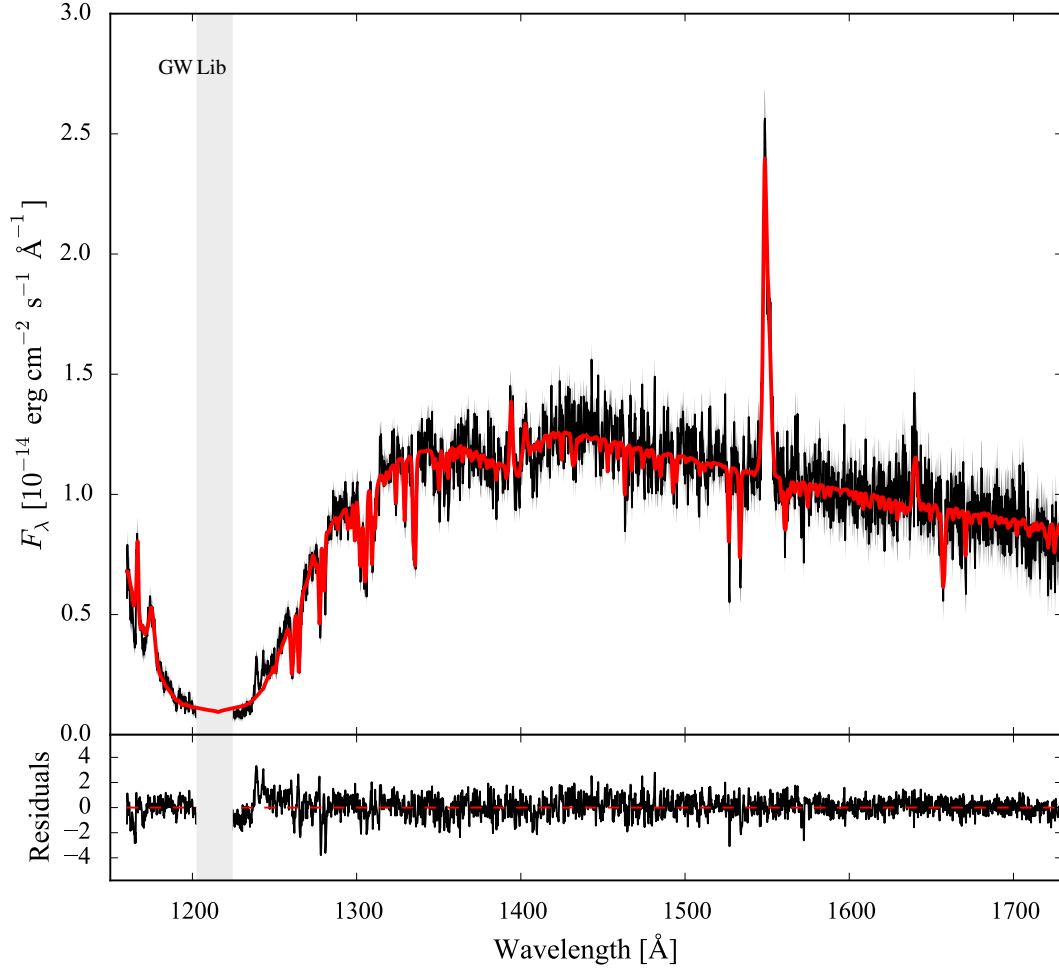| Instrument	STIS
Observation date	2000 Dec 07
$E(B-V)$ (mag)	$0.06^{+0}_{-0.02}$
P_{orb} (min)	79.28
Gaia EDR3 ID	2809168096329043712
ϖ (mas)	1.6 ± 0.6
d (pc)	609^{+343}_{-205}
Z ($Z_\odot$)	1.0
T_{eff} (K)	14353^{+1210}_{-743}
R_{WD} ($0.01\,R_\odot$)	$1.2^{+0.8}_{-0.6}$
M_{WD} ($M_\odot$)	$0.7^{+0.4}_{-0.3}$
$\log(g)$	8.2 ± 0.7
$\langle \dot{M} \rangle$ ($10^{-10}\,M_\odot\,yr^{-1}$)	$0.9^{+2.4}_{-0.9}$
WD contribution	80%

Figure B7. Ultraviolet *HST* spectra (black) of LL And along with the best-fitting model (red), computed as described in Section 3.2.

Table B8. Best-fitting parameters for AL Com.

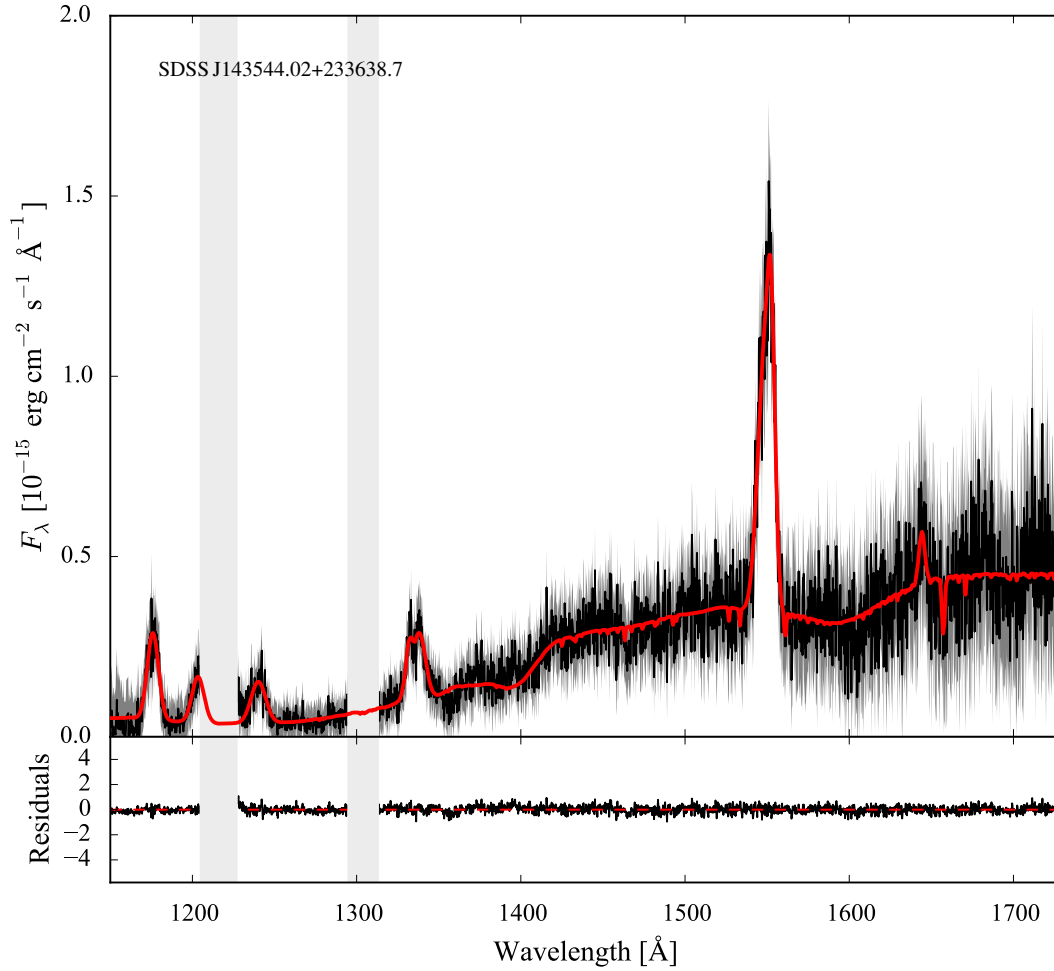| Instrument	STIS
Observation date	2000 Nov 27
$E(B-V)$ (mag)	0.045 ± 0.018
P_{orb} (min)	81.6
Gaia EDR3 ID	3932951035266314496
ϖ (mas)	1.9 ± 0.6
d (pc)	523^{+252}_{-149}
Z ($Z_\odot$)	0.2
T_{eff} (K)	15840^{+1453}_{-1243}
R_{WD} ($0.01\,R_\odot$)	$1.0^{+0.9}_{-0.6}$
M_{WD} ($M_\odot$)	$0.9^{+0.5}_{-0.3}$
$\log(g)$	8.4 ± 0.8
$\langle \dot{M} \rangle$ ($10^{-10}\,M_\odot\,yr^{-1}$)	$0.9^{+3.1}_{-1.0}$
WD contribution	79%

Figure B8. Ultraviolet *HST* spectra (black) of AL Com along with the best-fitting model (red), computed as described in Section 3.2.

Table B9. Best-fitting parameters for WZ Sge.

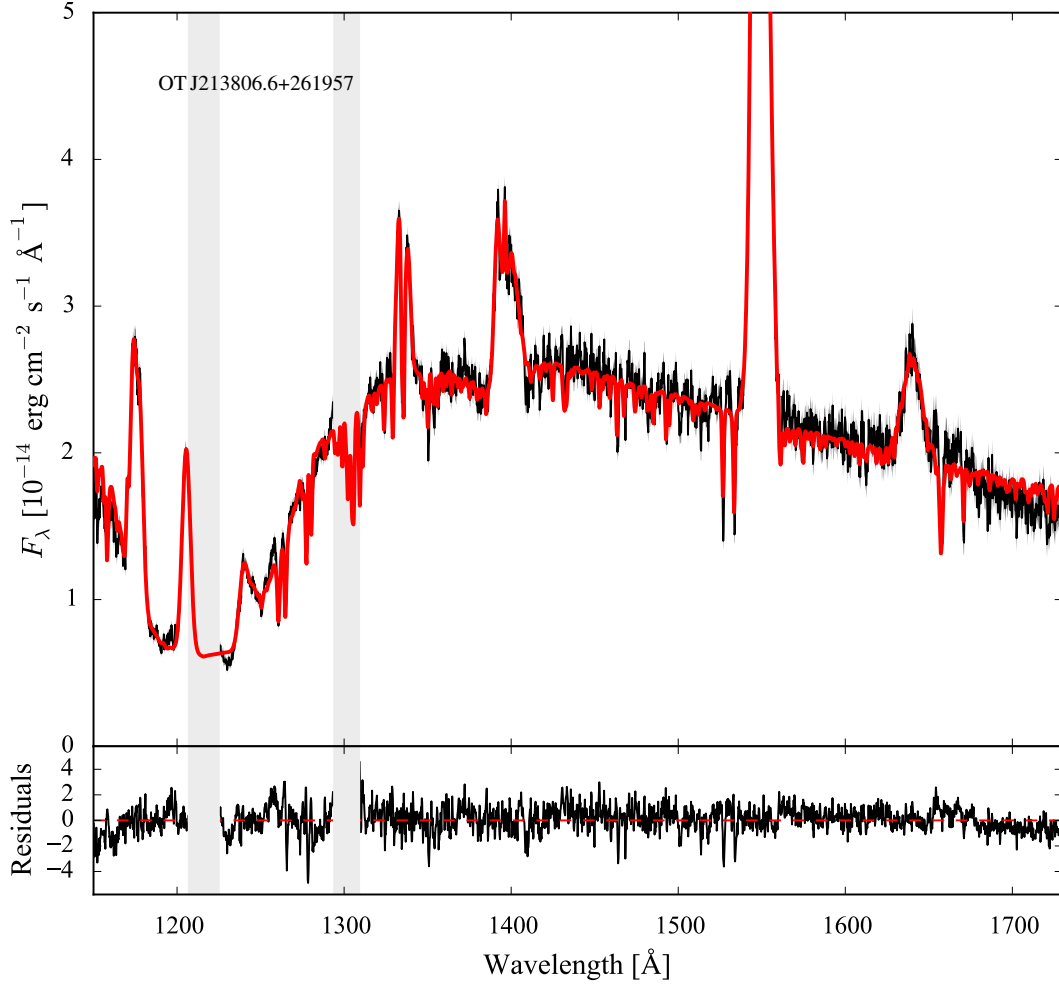| Instrument	FOS
Observation date	1992 Oct 08
$E(B-V)$ (mag)	$0.003^{+0.015}_{-0.003}$
$P_{\rm orb}$ (min)	81.63
Gaia EDR3 ID	1809844934461976832
ϖ (mas)	22.14 ± 0.03
d (pc)	45.17 ± 0.06
Z ($Z_\odot$)	0.01
$T_{\rm eff}$ (K)	13190^{+115}_{-105}
$R_{\rm WD}$ ($0.01\,R_\odot$)	1.05 ± 0.03
$M_{\rm WD}$ ($M_\odot$)	0.8 ± 0.02
$\log(g)$	8.3 ± 0.04
$\langle \dot{M} \rangle$ ($10^{-10}\,M_\odot\,{\rm yr}^{-1}$)	$0.52^{+0.014}_{-0.01}$
WD contribution	78%

Figure B9. Ultraviolet *HST* spectra (black) of WZ Sge along with the best-fitting model (red), computed as described in Section 3.2.

Table B10. Best-fitting parameters for SW UMa.

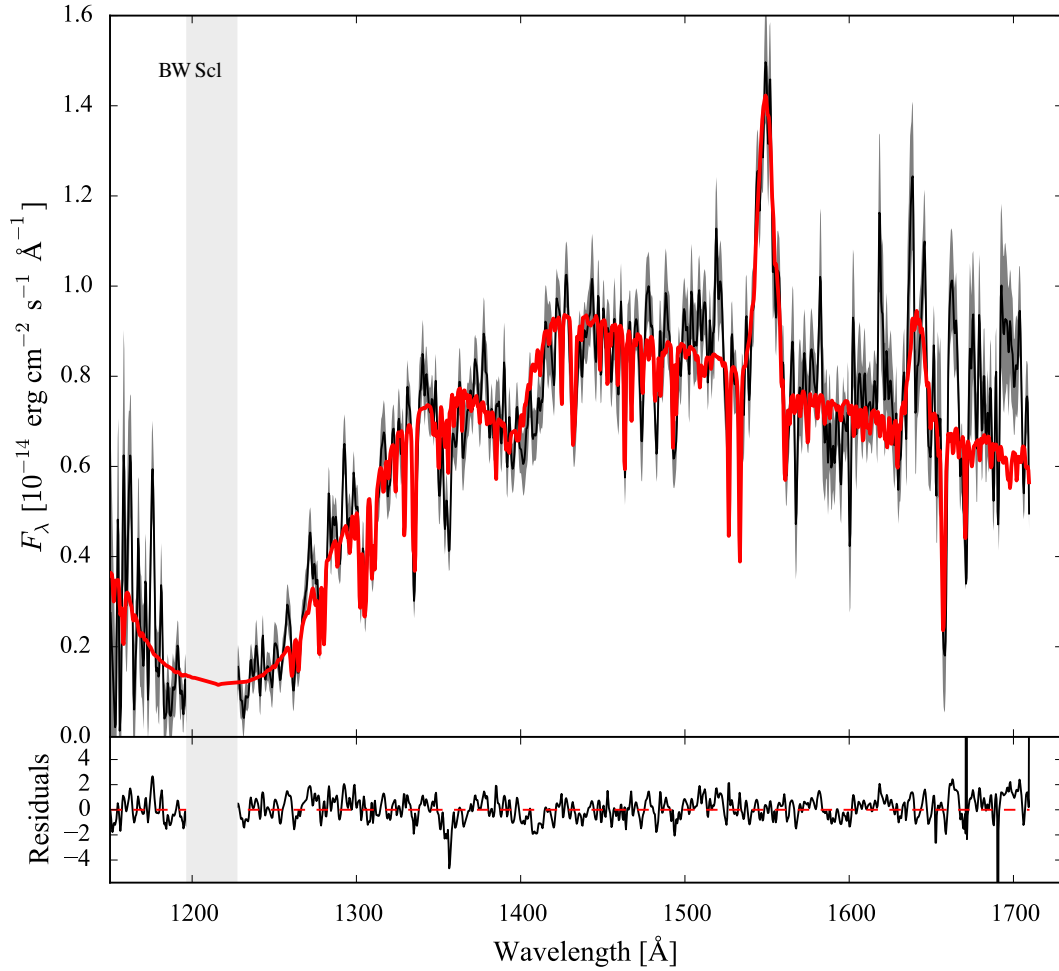| Instrument	STIS
Observation date	2000 Mar 26
$E(B-V)$ (mag)	$0.008^{+0.017}_{-0.008}$
P_{orb} (min)	81.81
Gaia EDR3 ID	1030279027003254784
ϖ (mas)	6.23 ± 0.06
d (pc)	160.6 ± 1.6
Z ($Z_\odot$)	0.2
T_{eff} (K)	13854^{+189}_{-131}
R_{WD} ($0.01\,R_\odot$)	$1.29^{+0.09}_{-0.10}$
M_{WD} ($M_\odot$)	$0.61^{+0.06}_{-0.04}$
$\log(g)$	$8.01^{+0.11}_{-0.09}$
$\langle \dot{M} \rangle$ ($10^{-10}\,M_\odot\,yr^{-1}$)	$1.07^{+0.15}_{-0.14}$
WD contribution	61%

Figure B10. Ultraviolet *HST* spectra (black) of SW UMa along with the best-fitting model (red), computed as described in Section 3.2.

Table B11. Best-fitting parameters for V1108 Her.

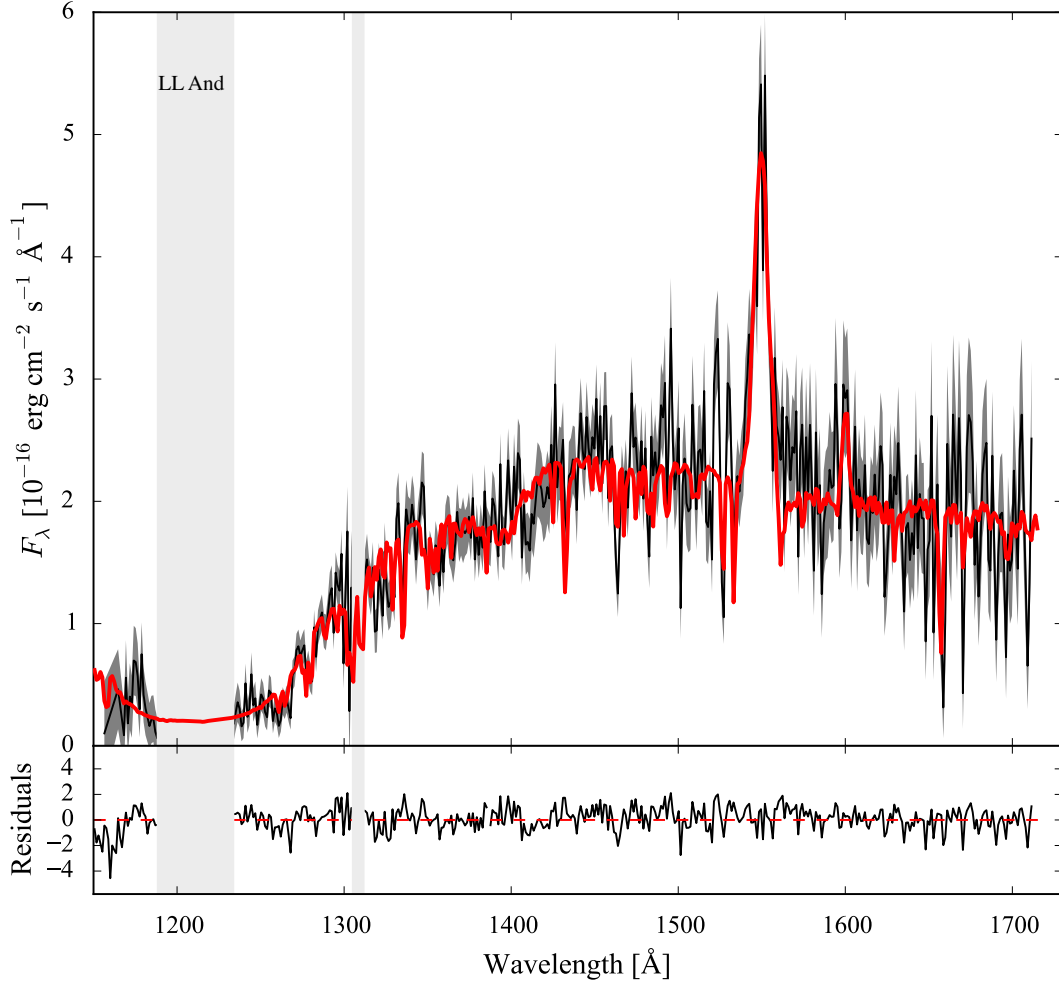| Instrument	COS
Observation date	2013 Jun 06
$E(B-V)$ (mag)	0.046 ± 0.019
P_{orb} (min)	81.87
Gaia EDR3 ID	4538504384210935424
ϖ (mas)	6.8 ± 0.1
d (pc)	148 ± 2
Z ($Z_\odot$)	1.0
T_{eff} (K)	13943^{+185}_{-226}
R_{WD} ($0.01\,R_\odot$)	$0.95^{+0.14}_{-0.11}$
M_{WD} ($M_\odot$)	$0.88^{+0.09}_{-0.11}$
$\log(g)$	$8.42^{+0.15}_{-0.17}$
$\langle \dot{M} \rangle$ ($10^{-10}\,M_\odot\,\mathrm{yr}^{-1}$)	$0.52^{+0.15}_{-0.11}$
WD contribution	75%

Figure B11. Ultraviolet *HST* spectra (black) of V1108 Her along with the best-fitting model (red), computed as described in Section 3.2.

Table B12. Best-fitting parameters for ASAS J002511+1217.2.

Instrument	COS
Observation date	2012 Nov 15
$E(B-V)$ (mag)	$0.009^{+0.016}_{-0.009}$
P_{orb} (min)	82.0
Gaia EDR3 ID	2754909740118313344
ϖ (mas)	6.4 ± 0.1
d (pc)	157 ± 3
Z ($Z_\odot$)	0.1
T_{eff} (K)	13208^{+154}_{-112}
R_{WD} ($0.01\,R_\odot$)	0.78 ± 0.04
M_{WD} ($M_\odot$)	1.02 ± 0.04
$\log(g)$	8.66 ± 0.07
$\langle \dot{M} \rangle$ ($10^{-10}\,M_\odot\,\mathrm{yr}^{-1}$)	$0.27^{+0.03}_{-0.02}$
WD contribution	74%

Figure B12. Ultraviolet *HST* spectra (black) of ASAS J002511+1217.2 along with the best-fitting model (red), computed as described in Section 3.2.

Table B13. Best-fitting parameters for HV Vir.

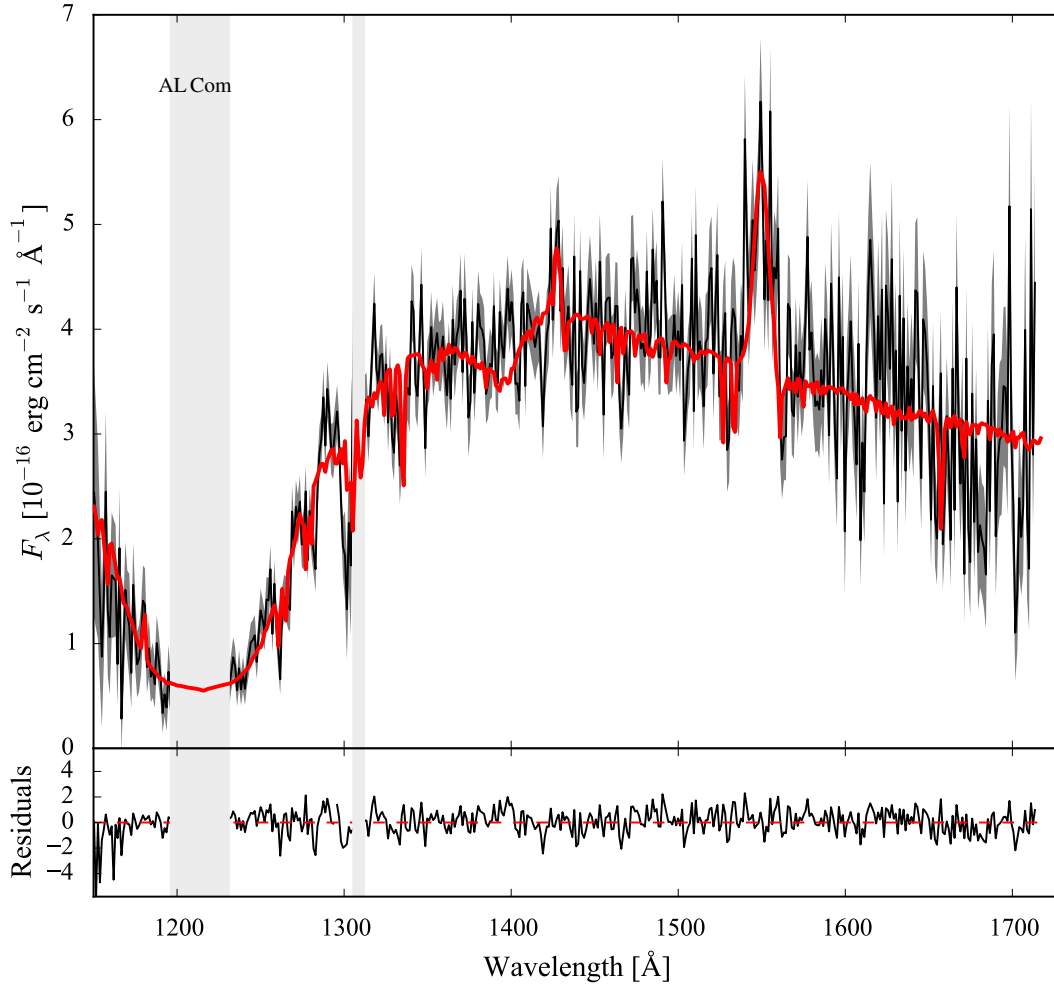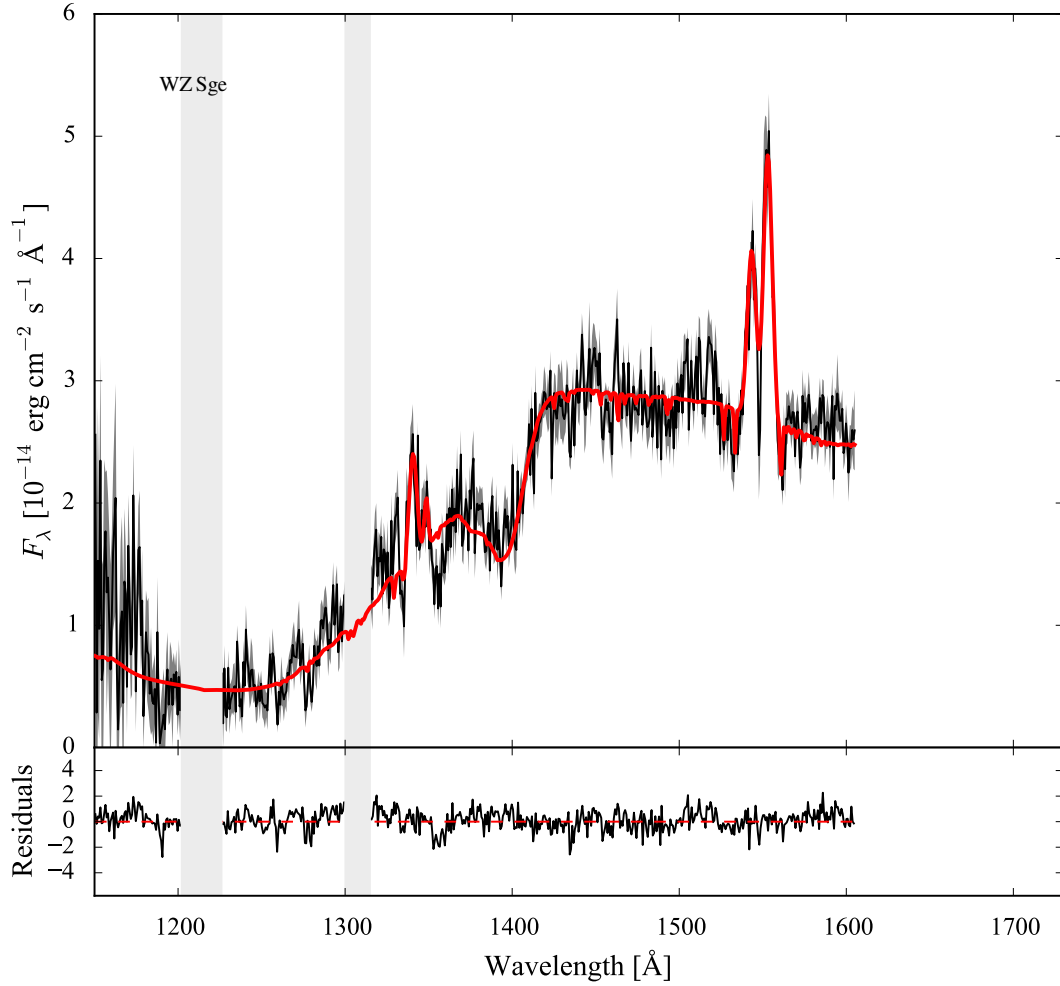| Instrument	STIS
Observation date	2000 Jun 10
$E(B-V)$ (mag)	$0.024^{+0.012}_{-0.021}$
$P_{\rm orb}$ (min)	82.18
Gaia EDR3 ID	3688359000015020800
ϖ (mas)	3.2 ± 0.3
d (pc)	317^{+29}_{-25}
Z ($Z_\odot$)	0.2
$T_{\rm eff}$ (K)	12958^{+257}_{-291}
$R_{\rm WD}$ ($0.01\,{\rm R}_\odot$)	$0.96^{+0.21}_{-0.16}$
$M_{\rm WD}$ (${\rm M}_\odot$)	$0.87^{+0.13}_{-0.17}$
$\log(g)$	$8.4^{+0.2}_{-0.3}$
$\langle \dot{M} \rangle$ ($10^{-10}\,{\rm M}_\odot\,{\rm yr}^{-1}$)	$0.4^{+0.2}_{-0.12}$
WD contribution	93%

Figure B13. Ultraviolet *HST* spectra (black) of HV Vir along with the best-fitting model (red), computed as described in Section 3.2.

Table B14. Best-fitting parameters for SDSS J103533.02+055158.4.

Instrument	COS
Observation date	2013 Mar 08
$E(B-V)$ (mag)	$0.017^{+0.018}_{-0.017}$
$P_{\rm orb}$ (min)	82.22
Gaia EDR3 ID	3859020040917830400
ϖ (mas)	5.1 ± 0.3
d (pc)	195^{+12}_{-10}
Z ($Z_\odot$)	0.01
$T_{\rm eff}$ (K)	11876^{+108}_{-115}
$R_{\rm WD}$ ($0.01\,R_\odot$)	$0.8^{+0.11}_{-0.09}$
$M_{\rm WD}$ ($M_\odot$)	$1.00^{+0.08}_{-0.10}$
$\log(g)$	$8.63^{+0.14}_{-0.16}$
$\langle \dot{M} \rangle$ ($10^{-10}\,M_\odot\,{\rm yr}^{-1}$)	$0.18^{+0.06}_{-0.04}$
WD contribution	91%

Figure B14. Ultraviolet *HST* spectra (black) of SDSS J103533.02+055158.4 along with the best-fitting model (red), computed as described in Section 3.2.

Table B15. Best-fitting parameters for WX Cet.

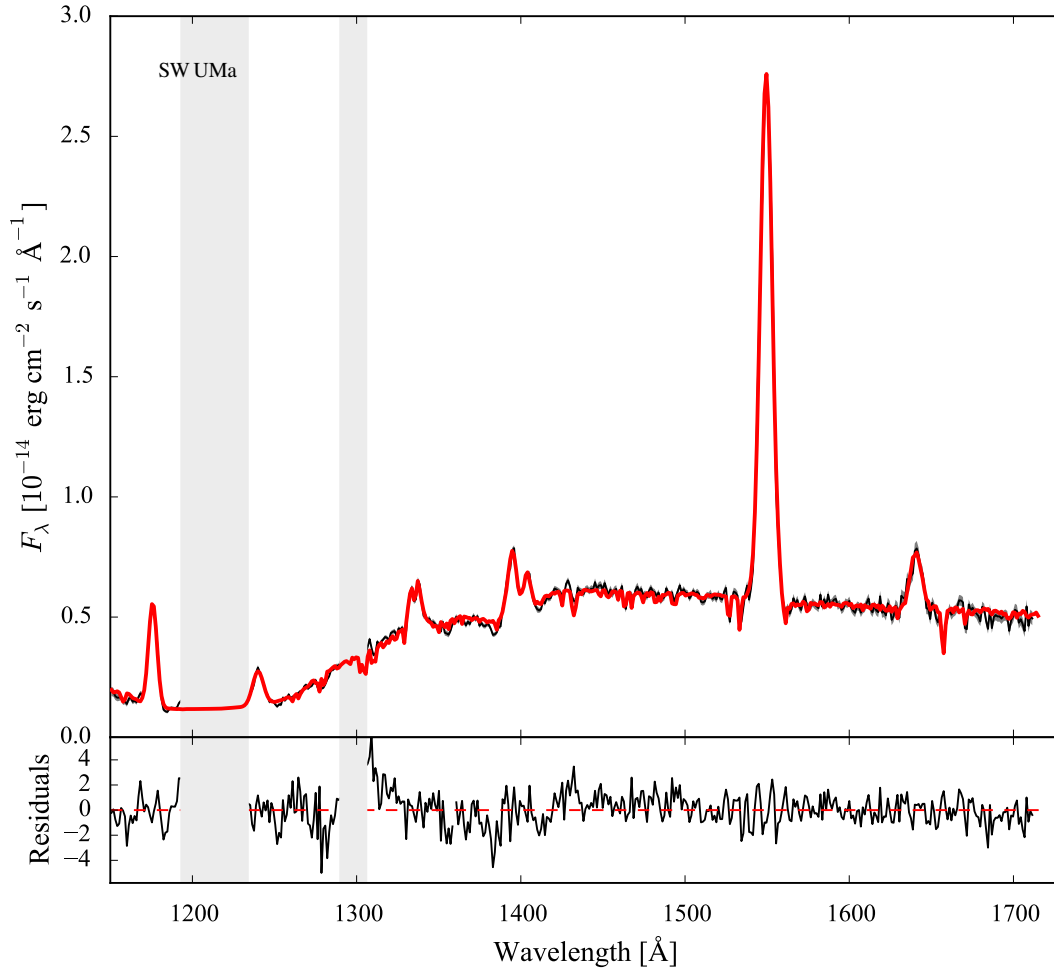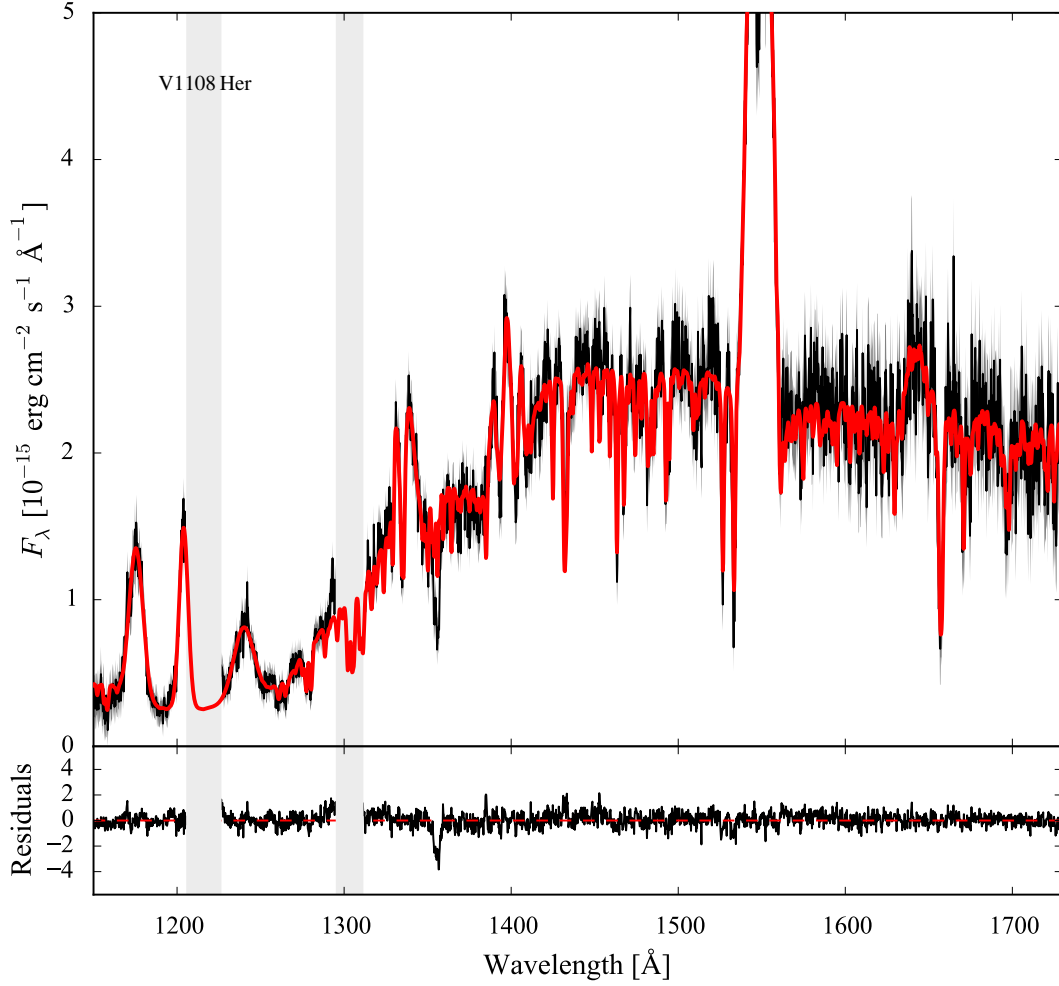| Instrument	STIS
Observation date	2000 Oct 30
$E(B-V)$ (mag)	$0.013^{+0.016}_{-0.013}$
$P_{\rm orb}$ (min)	83.9
Gaia EDR3 ID	2355217815809560192
ϖ (mas)	3.97 ± 0.13
d (pc)	252^{+9}_{-8}
Z ($Z_\odot$)	0.1
$T_{\rm eff}$ (K)	15186^{+1460}_{-1468}
$R_{\rm WD}$ ($0.01\,R_\odot$)	$0.63^{+0.28}_{-0.18}$
$M_{\rm WD}$ ($M_\odot$)	$1.10^{+0.17}_{-0.21}$
$\log(g)$	8.8 ± 0.4
$\langle \dot{M} \rangle$ ($10^{-10}\,M_\odot\,{\rm yr}^{-1}$)	$0.3^{+0.07}_{-0.06}$
WD contribution	24%

Figure B15. Ultraviolet *HST* spectra (black) of WX Cet along with the best-fitting model (red), computed as described in Section 3.2.

Table B16. Best-fitting parameters for SDSS J075507.70+143547.6.

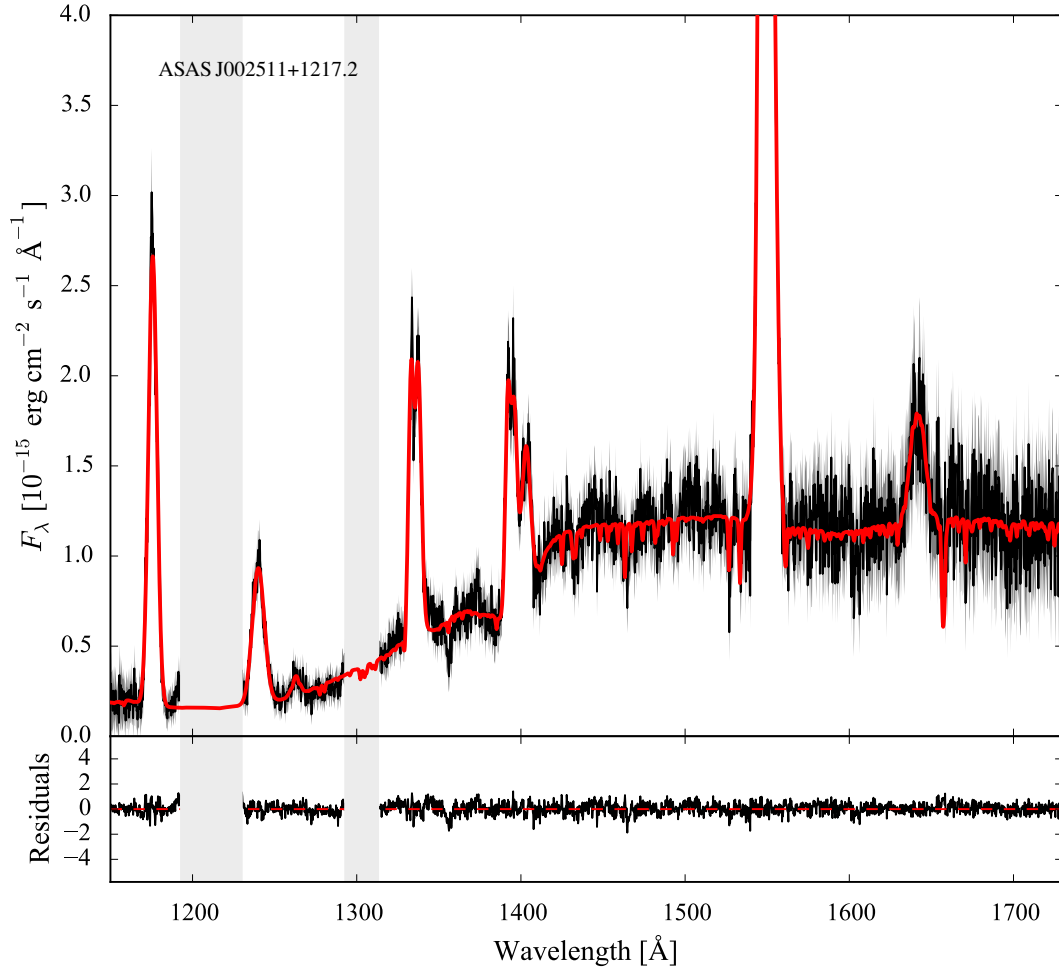| Instrument	COS
Observation date	2012 Dec 14
$E(B-V)$ (mag)	$0.011^{+0.015}_{-0.011}$
P_{orb} (min)	84.76
Gaia EDR3 ID	654539826068054400
ϖ (mas)	4.2 ± 0.2
d (pc)	239^{+12}_{-11}
Z (Z$_\odot$)	0.5
T_{eff} (K)	16193^{+280}_{-357}
R_{WD} (0.01 R$_\odot$)	$0.92^{+0.15}_{-0.11}$
M_{WD} (M$_\odot$)	$0.91^{+0.09}_{-0.12}$
$\log(g)$	$8.47^{+0.15}_{-0.19}$
$\langle \dot{M} \rangle$ (10^{-10} M$_\odot$ yr^{-1})	$0.87^{+0.27}_{-0.18}$
WD contribution	87%

Figure B16. Ultraviolet *HST* spectra (black) of SDSS J075507.70+143547.6 along with the best-fitting model (red), computed as described in Section 3.2.

Table B17. Best-fitting parameters for SDSS J080434.20+510349.2.

Instrument	COS
Observation date	2011 Nov 03
$E(B-V)$ (mag)	$0.007^{+0.016}_{-0.007}$
P_{orb} (min)	84.97
Gaia EDR3 ID	935056333580267392
ϖ (mas)	7.03 ± 0.11
d (pc)	142 ± 2
Z ($Z_\odot$)	0.5
T_{eff} (K)	13715^{+55}_{-79}
R_{WD} ($0.01\,R_\odot$)	$0.80^{+0.04}_{-0.03}$
M_{WD} ($M_\odot$)	$1.01^{+0.03}_{-0.04}$
$\log(g)$	$8.64^{+0.05}_{-0.06}$
$\langle \dot{M} \rangle$ ($10^{-10}\,M_\odot\,\text{yr}^{-1}$)	0.32 ± 0.03
WD contribution	87%

Figure B17. Ultraviolet *HST* spectra (black) of SDSS J080434.20+510349.2 along with the best-fitting model (red), computed as described in Section 3.2.

Table B18. Best-fitting parameters for EG Cnc.

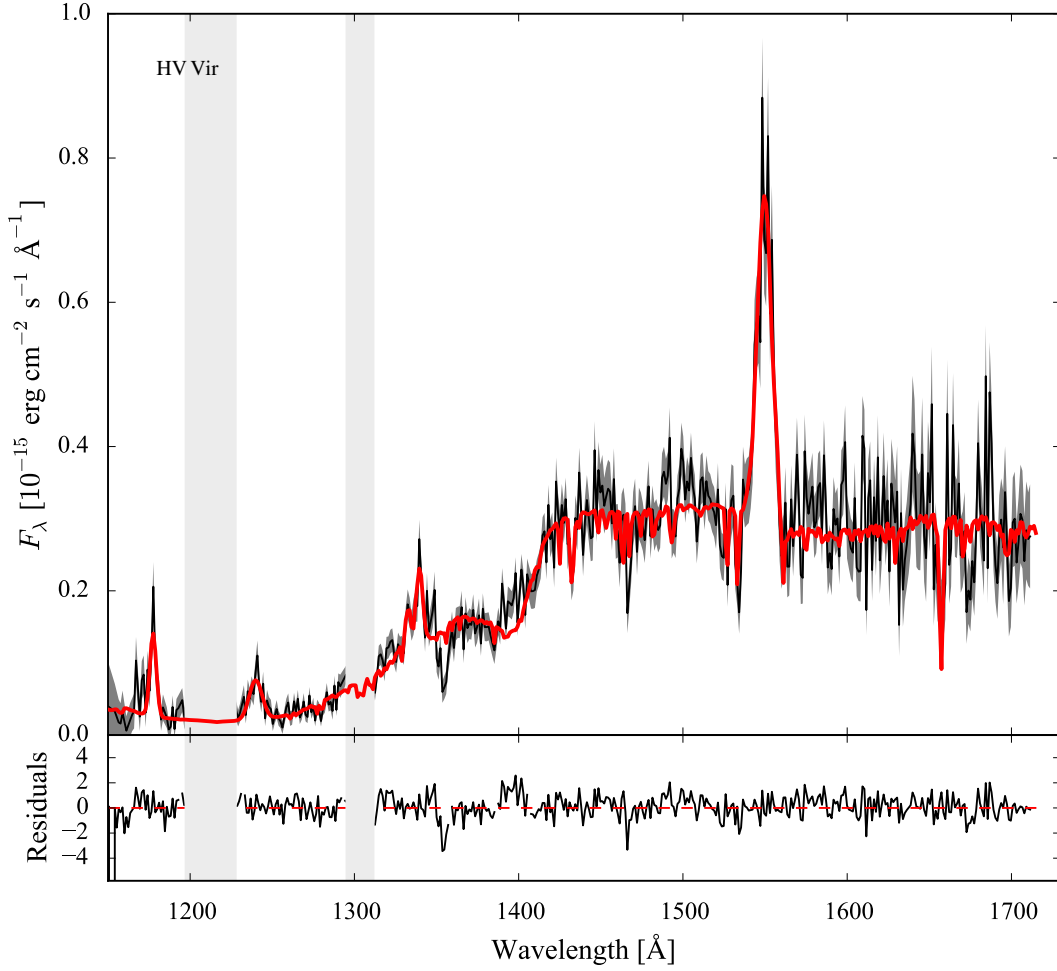| Instrument	STIS
Observation date	2006 Dec 20
$E(B-V)$ (mag)	$0.008^{+0.017}_{-0.008}$
P_{orb} (min)	86.36
Gaia EDR3 ID	703580960947960576
ϖ (mas)	5.4 ± 0.2
d (pc)	186 ± 7
Z ($Z_{\odot}$)	0.2
T_{eff} (K)	12295^{+56}_{-57}
R_{WD} (0.01 $R_{\odot}$)	$0.77^{+0.06}_{-0.05}$
M_{WD} ($M_{\odot}$)	$1.03^{+0.04}_{-0.05}$
$\log(g)$	$8.67^{+0.07}_{-0.08}$
$\langle \dot{M} \rangle$ ($10^{-10}\,M_{\odot}\,\mathrm{yr}^{-1}$)	$0.2^{+0.03}_{-0.02}$
WD contribution	100%

Figure B18. Ultraviolet *HST* spectra (black) of EG Cnc along with the best-fitting model (red), computed as described in Section 3.2.

Table B19. Best-fitting parameters for EK TrA.

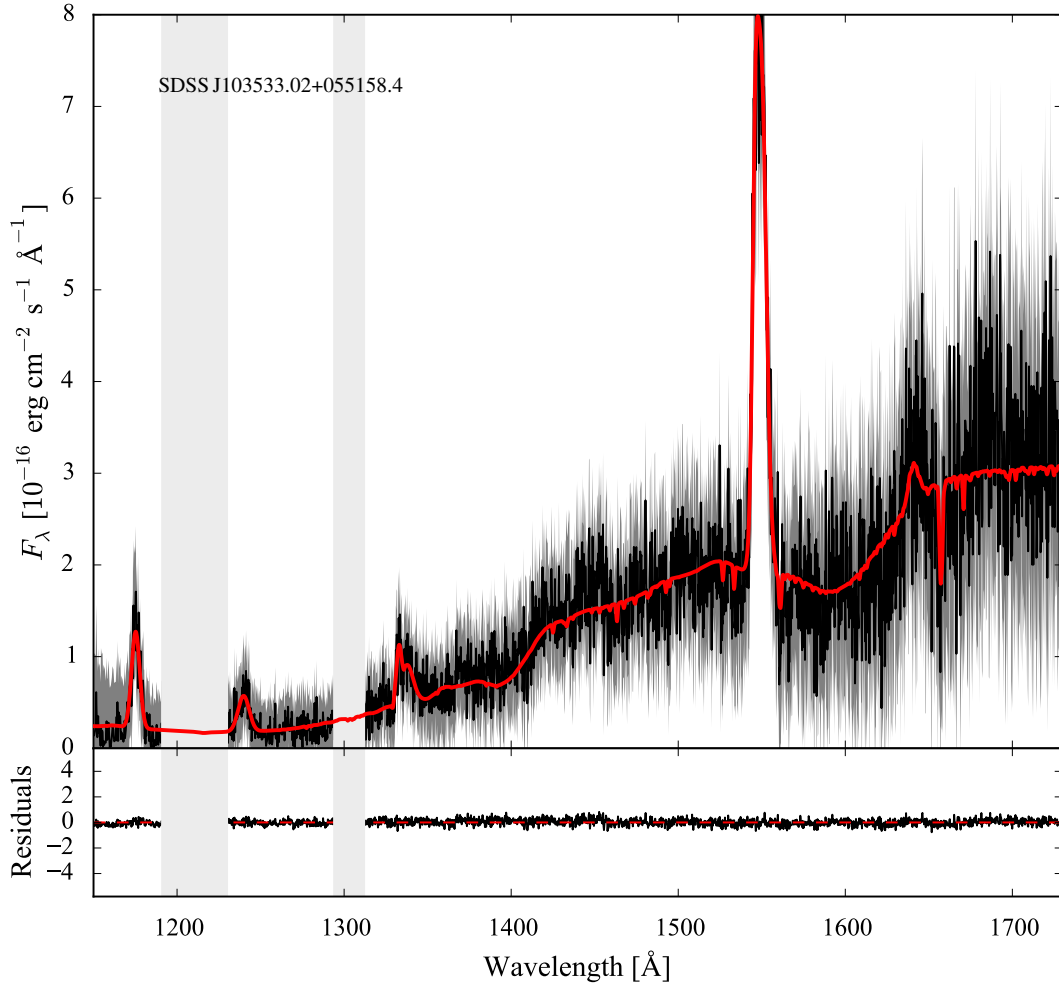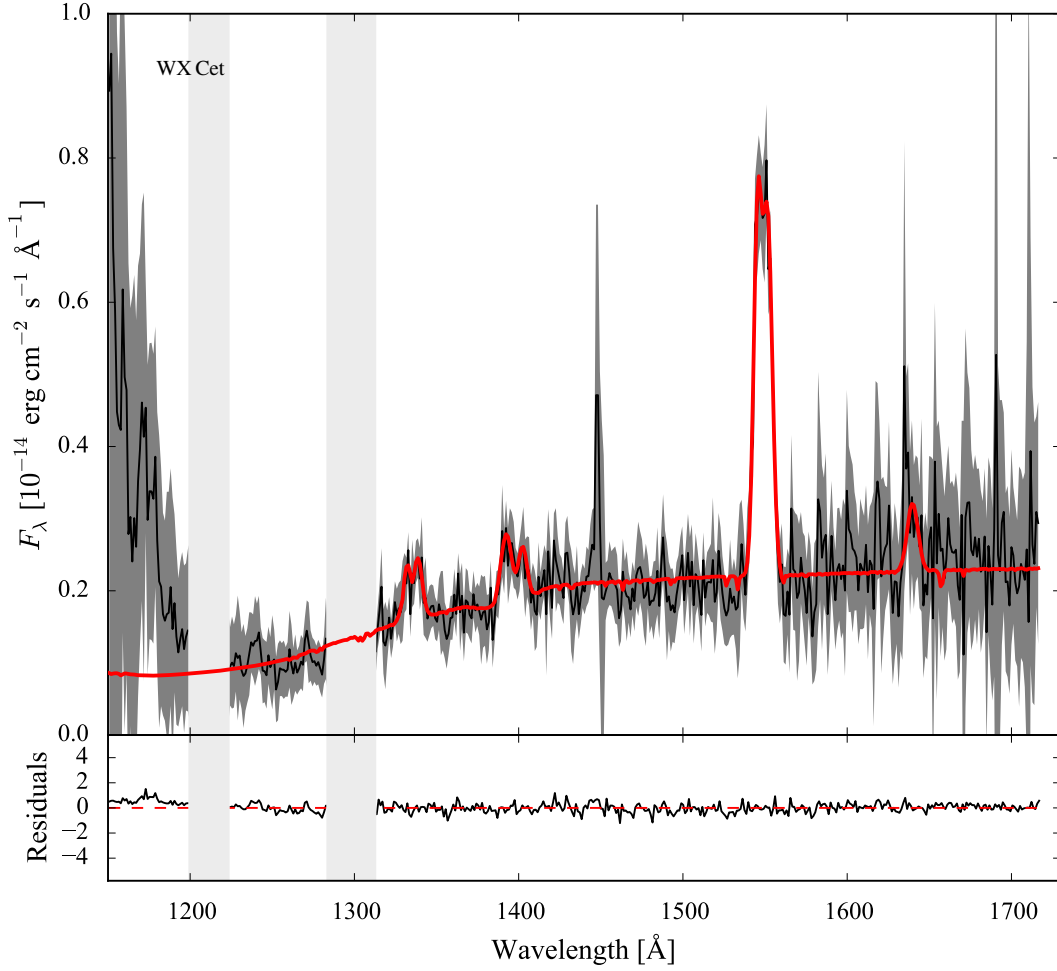| Instrument	STIS
Observation date	1999 Jul 25
$E(B-V)$ (mag)	0.034 ± 0.019
P_{orb} (min)	86.36
Gaia EDR3 ID	5825198967486003072
ϖ (mas)	6.61 ± 0.04
d (pc)	151.4 ± 0.8
Z ($Z_\odot$)	0.5
T_{eff} (K)	17608^{+269}_{-481}
R_{WD} ($0.01\,R_\odot$)	$0.97^{+0.17}_{-0.11}$
M_{WD} ($M_\odot$)	$0.87^{+0.09}_{-0.13}$
$\log(g)$	$8.4^{+0.14}_{-0.21}$
$\langle \dot{M} \rangle$ ($10^{-10}\,M_\odot\,\mathrm{yr}^{-1}$)	$1.4^{+0.4}_{-0.3}$
WD contribution	58%

Figure B19. Ultraviolet *HST* spectra (black) of EK TrA along with the best-fitting model (red), computed as described in Section 3.2.

Table B20. Best-fitting parameters for 1RXS J105010.8–140431.

Instrument	COS
Observation date	2013 May 10
$E(B-V)$ (mag)	$0.005^{+0.015}_{-0.005}$
P_{orb} (min)	88.56
Gaia EDR3 ID	3750072904055666176
ϖ (mas)	9.19 ± 0.09
d (pc)	109 ± 1
Z ($Z_\odot$)	0.1
T_{eff} (K)	11523^{+29}_{-47}
R_{WD} ($0.01\,\mathrm{R}_\odot$)	$1.08^{+0.04}_{-0.03}$
M_{WD} ($\mathrm{M}_\odot$)	$0.77^{+0.02}_{-0.03}$
$\log(g)$	$8.25^{+0.04}_{-0.05}$
$\langle \dot{M} \rangle$ ($10^{-10}\,\mathrm{M}_\odot\,\mathrm{yr}^{-1}$)	$0.332^{+0.028}_{-0.018}$
WD contribution	87%

Figure B20. Ultraviolet *HST* spectra (black) of 1RXS J105010.8–140431 along with the best-fitting model (red), computed as described in Section 3.2.

Table B21. Best-fitting parameters for BC UMa.

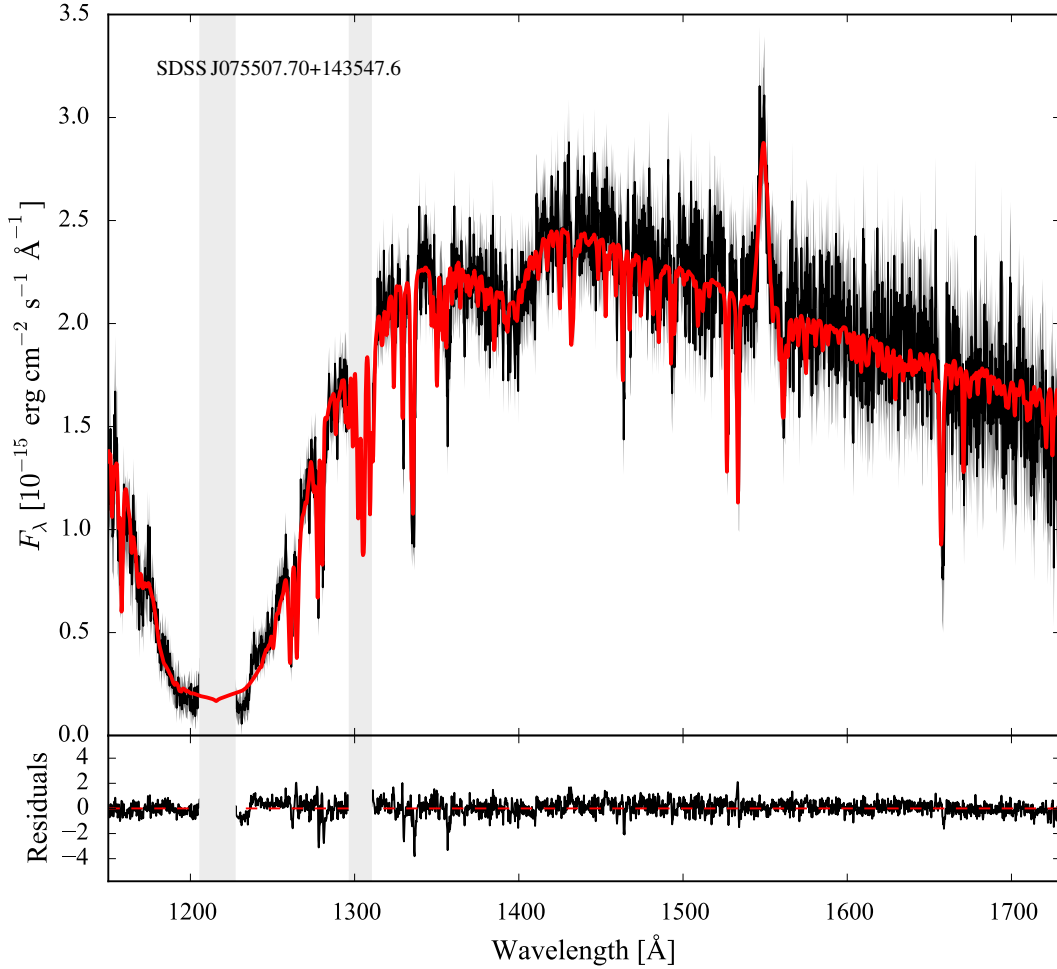| Instrument	STIS
Observation date	2000 Jul 18
$E(B-V)$ (mag)	$0.017^{+0}_{-0.017}$
$P_{\rm orb}$ (min)	90.16
Gaia EDR3 ID	787683052032971904
ϖ (mas)	3.41 ± 0.13
d (pc)	293^{+11}_{-10}
Z ($Z_\odot$)	0.2
$T_{\rm eff}$ (K)	14378^{+272}_{-327}
$R_{\rm WD}$ ($0.01\,{\rm R_\odot}$)	$1.57^{+0.19}_{-0.16}$
$M_{\rm WD}$ (${\rm M_\odot}$)	$0.48^{+0.08}_{-0.09}$
$\log(g)$	$7.73^{+0.15}_{-0.19}$
$\langle \dot{M} \rangle$ ($10^{-10}\,{\rm M_\odot\,yr^{-1}}$)	$2.0^{+0.5}_{-0.3}$
WD contribution	85%

Figure B21. Ultraviolet *HST* spectra (black) of BC UMa along with the best-fitting model (red), computed as described in Section 3.2.

Table B22. Best-fitting parameters for VY Aqr.

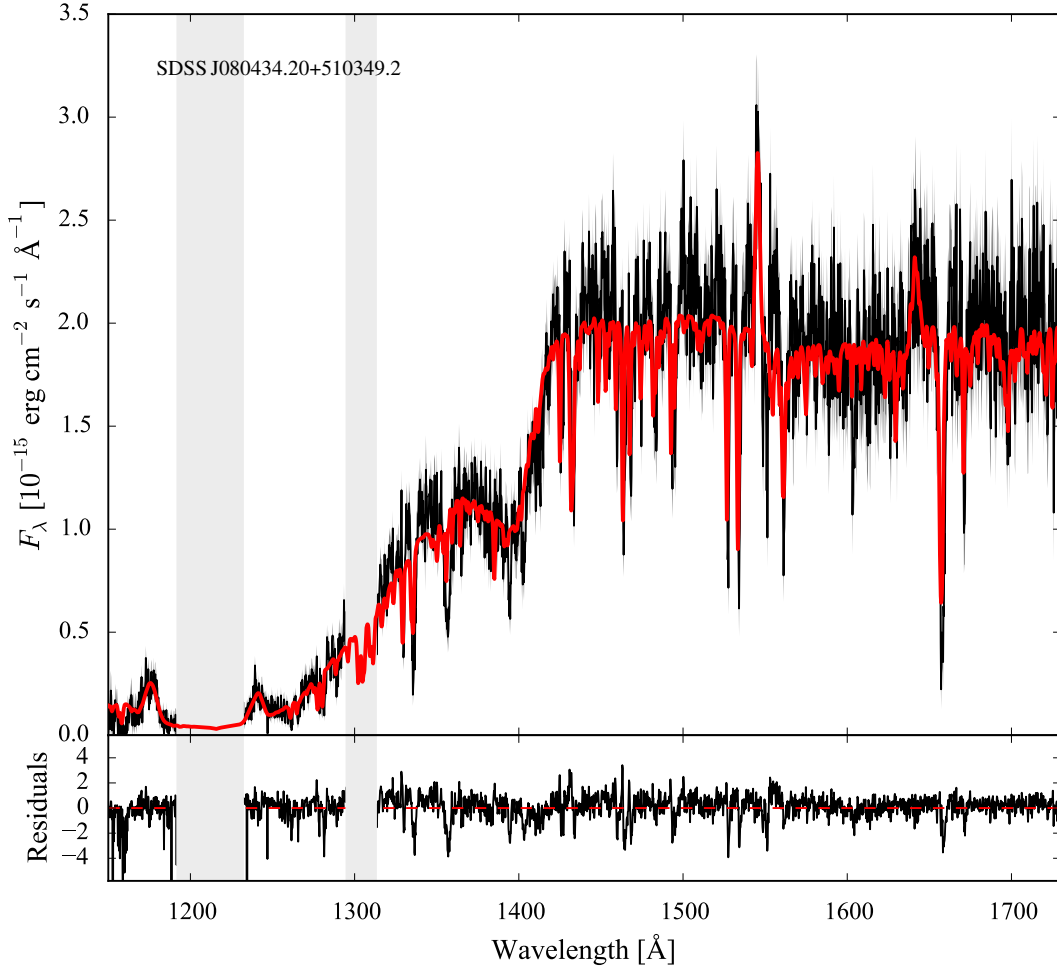| Instrument	STIS
Observation date	2000 Jul 10
$E(B-V)$ (mag)	$0.008^{+0.016}_{-0.008}$
$P_{\rm orb}$ (min)	90.85
Gaia EDR3 ID	6896767366186700416
ϖ (mas)	7.08 ± 0.09
d (pc)	$141.3^{+1.9}_{-1.8}$
Z ($Z_{\odot}$)	0.5
$T_{\rm eff}$ (K)	14453^{+316}_{-366}
$R_{\rm WD}$ ($0.01\,R_{\odot}$)	$0.74^{+0.07}_{-0.06}$
$M_{\rm WD}$ ($M_{\odot}$)	1.06 ± 0.06
$\log(g)$	$8.73^{+0.12}_{-0.11}$
$\langle \dot{M} \rangle$ ($10^{-10}\,M_{\odot}\,{\rm yr}^{-1}$)	$0.33^{+0.04}_{-0.03}$
WD contribution	45%

Figure B22. Ultraviolet *HST* spectra (black) of VY Aqr along with the best-fitting model (red), computed as described in Section 3.2.

Table B23. Best-fitting parameters for QZ Lib.

Instrument	COS
Observation date	2013 Apr 26
$E(B-V)$ (mag)	0.10 ± 0.03
P_{orb} (min)	92.36
Gaia EDR3 ID	6318149711371454464
ϖ (mas)	5.0 ± 0.2
d (pc)	199^{+11}_{-10}
Z ($Z_\odot$)	0.01
T_{eff} (K)	11419^{+175}_{-229}
R_{WD} ($0.01\,R_\odot$)	$1.01^{+0.23}_{-0.18}$
M_{WD} ($M_\odot$)	$0.82^{+0.14}_{-0.19}$
$\log(g)$	$8.3^{+0.2}_{-0.3}$
$\langle \dot{M} \rangle$ ($10^{-10}\,M_\odot\,\text{yr}^{-1}$)	$0.27^{+0.15}_{-0.09}$
WD contribution	74%

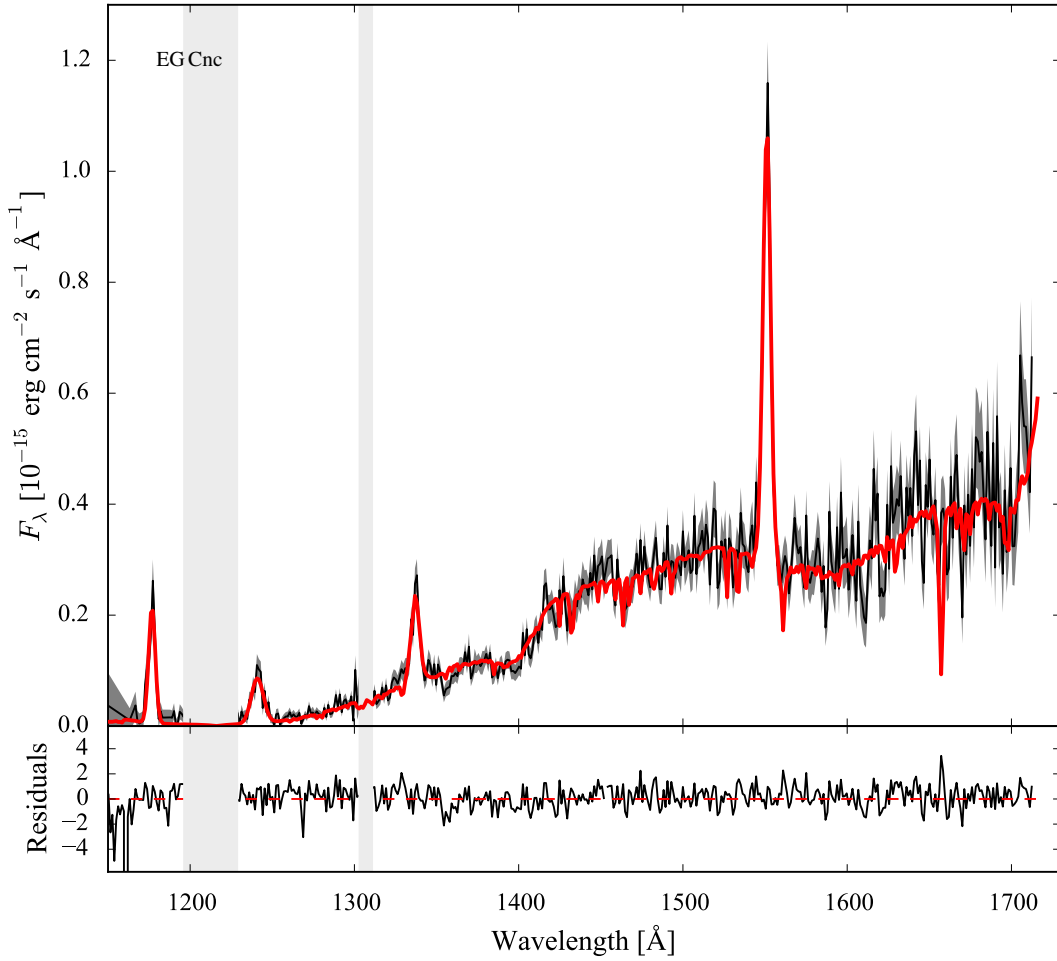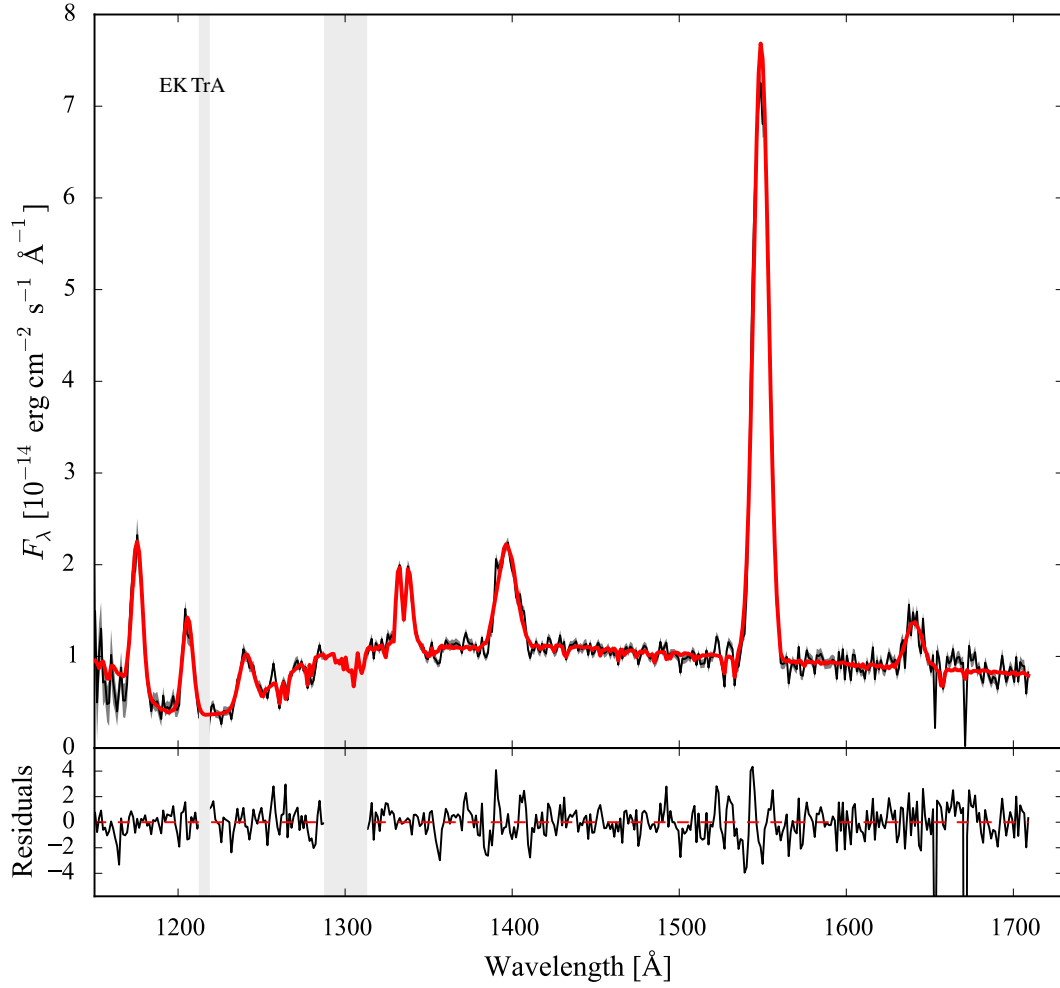

Figure B23. Ultraviolet *HST* spectra (black) of QZ Lib along with the best-fitting model (red), computed as described in Section 3.2.

Table B24. Best-fitting parameters for SDSS J153817.35+512338.0.

Instrument	COS
Observation date	2013 May 16
$E(B-V)$ (mag)	0.027 ± 0.018
P_{orb} (min)	93.11
Gaia EDR3 ID	1595085299649674240
ϖ (mas)	1.64 ± 0.12
d (pc)	607^{+47}_{-40}
Z ($Z_\odot$)	0.01
T_{eff} (K)	35284^{+600}_{-688}
R_{WD} ($0.01\,R_\odot$)	$0.89^{+0.16}_{-0.12}$
M_{WD} ($M_\odot$)	$0.97^{+0.09}_{-0.11}$
$\log(g)$	$8.53^{+0.17}_{-0.2}$
$\langle \dot{M} \rangle$ ($10^{-10}\,M_\odot\,\mathrm{yr}^{-1}$)	$18.0^{+7.0}_{-4.0}$
WD contribution	100%

Figure B24. Ultraviolet *HST* spectra (black) of SDSS J153817.35+512338.0 along with the best-fitting model (red), computed as described in Section 3.2.

Table B25. Best-fitting parameters for UV Per.

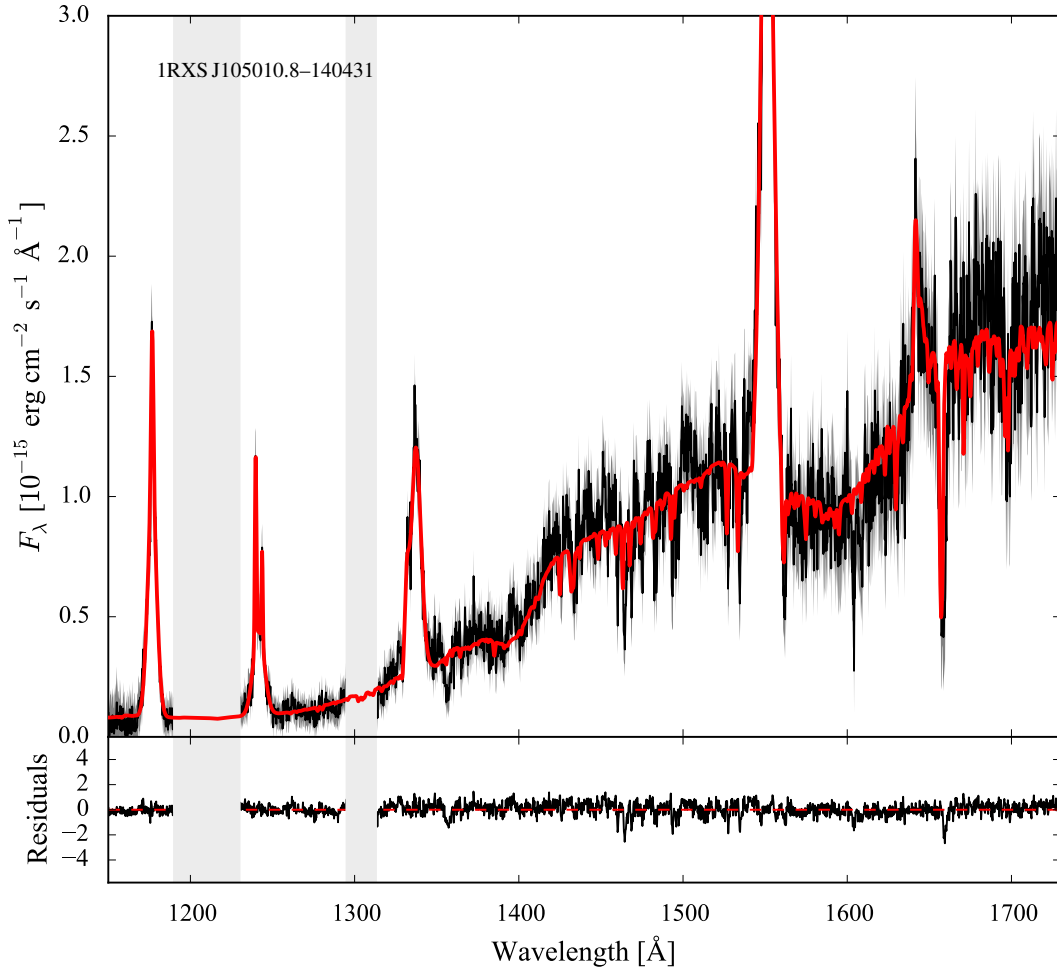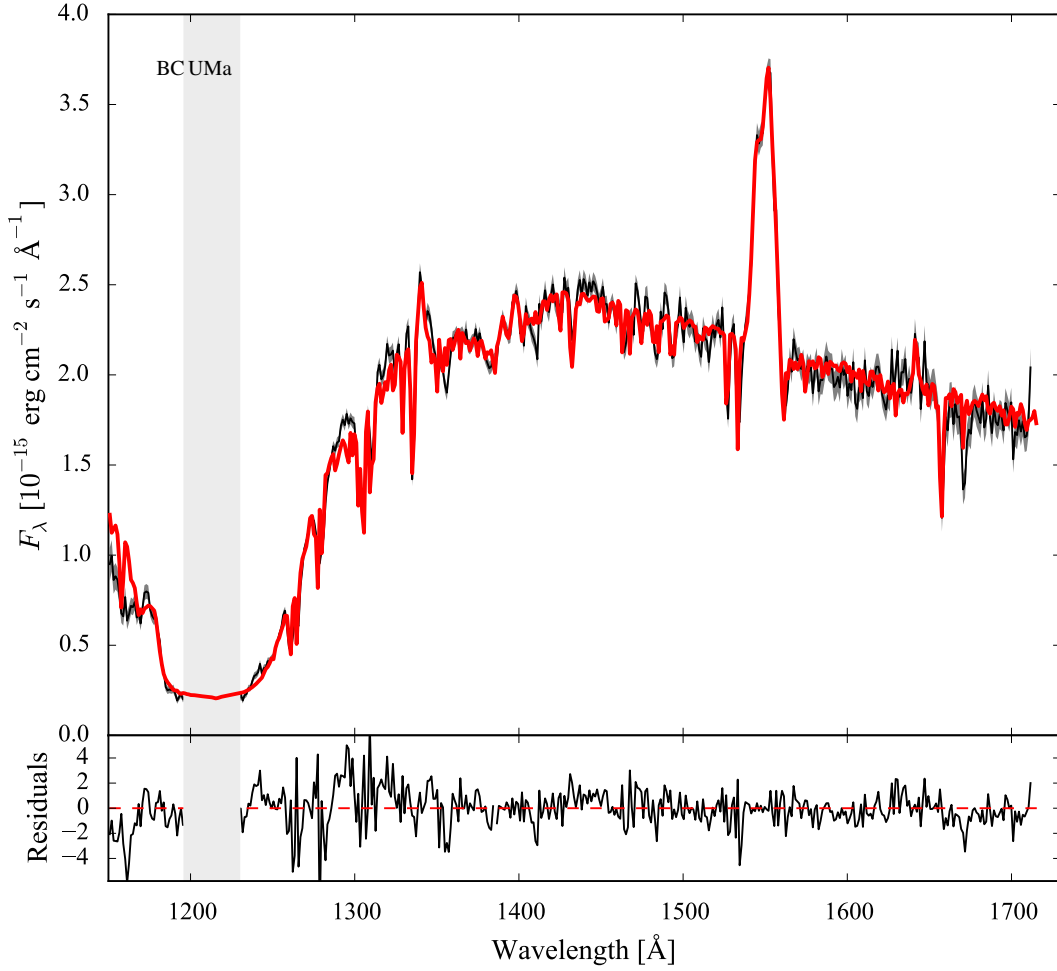| Instrument	STIS
Observation date	2002 Oct 11
$E(B-V)$ (mag)	0.07 ± 0.04
P_{orb} (min)	93.44
Gaia EDR3 ID	457106501671769472
ϖ (mas)	4.04 ± 0.11
d (pc)	248^{+7}_{-6}
Z ($Z_\odot$)	0.2
T_{eff} (K)	14040^{+539}_{-645}
R_{WD} ($0.01\,R_\odot$)	$1.2^{+0.4}_{-0.3}$
M_{WD} ($M_\odot$)	0.7 ± 0.2
$\log(g)$	8.1 ± 0.4
$\langle \dot{M} \rangle$ ($10^{-10}\,M_\odot\,\mathrm{yr}^{-1}$)	$0.9^{+0.7}_{-0.4}$
WD contribution	69%

Figure B25. Ultraviolet *HST* spectra (black) of UV Per along with the best-fitting model (red), computed as described in Section 3.2.

Table B26. Best-fitting parameters for 1RXS J023238.8–371812.

Instrument	COS
Observation date	2012 Nov 01
$E(B-V)$ (mag)	$0.005^{+0.014}_{-0.005}$
$P_{\rm orb}$ (min)	95.04
Gaia EDR3 ID	4953766320874344704
ϖ (mas)	4.68 ± 0.16
d (pc)	214^{+8}_{-7}
Z (Z$_\odot$)	0.2
$T_{\rm eff}$ (K)	14457^{+118}_{-135}
$R_{\rm WD}$ (0.01 R$_\odot$)	$0.63^{+0.05}_{-0.04}$
$M_{\rm WD}$ (M$_\odot$)	1.15 ± 0.04
$\log(g)$	$8.9^{+0.07}_{-0.08}$
$\langle \dot{M} \rangle$ (10^{-10} M$_\odot$ yr^{-1})	0.23 ± 0.03
WD contribution	71%

Figure B26. Ultraviolet *HST* spectra (black) of 1RXS J023238.8–371812 along with the best-fitting model (red), computed as described in Section 3.2.

Table B27. Best-fitting parameters for RZ Sge.

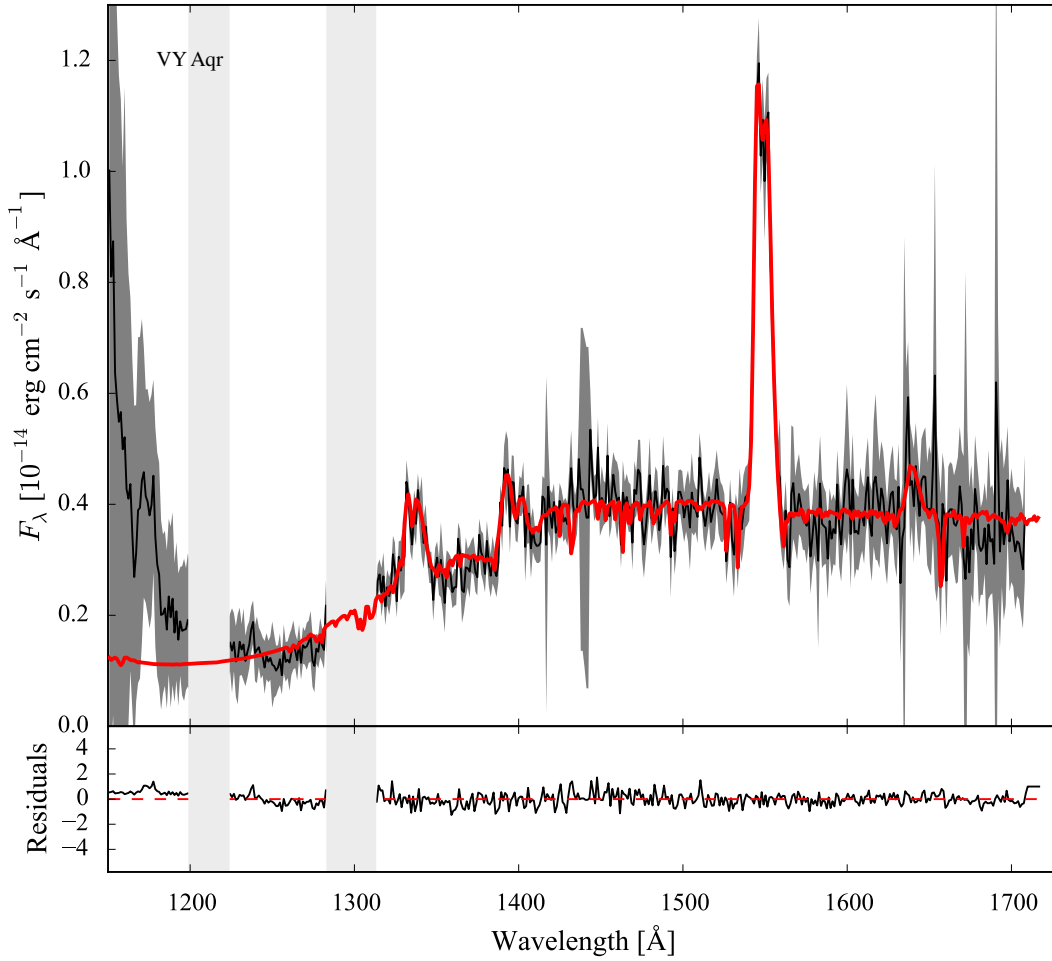| Instrument	STIS
Observation date	2003 Jun 13
$E(B-V)$ (mag)	0.03 ± 0.3
P_{orb} (min)	98.32
Gaia EDR3 ID	1820209309025797888
ϖ (mas)	3.40 ± 0.08
d (pc)	294 ± 7
Z ($Z_\odot$)	0.5
T_{eff} (K)	15197^{+419}_{-507}
R_{WD} ($0.01\,R_\odot$)	$1.09^{+0.27}_{-0.17}$
M_{WD} ($M_\odot$)	$0.78^{+0.13}_{-0.18}$
$\log(g)$	$8.3^{+0.2}_{-0.3}$
$\langle \dot{M} \rangle$ ($10^{-10}\,M_\odot\,\mathrm{yr}^{-1}$)	$1.0^{+0.5}_{-0.3}$
WD contribution	51%

Figure B27. Ultraviolet *HST* spectra (black) of RZ Sge along with the best-fitting model (red), computed as described in Section 3.2.

Table B28. Best-fitting parameters for CY UMa.

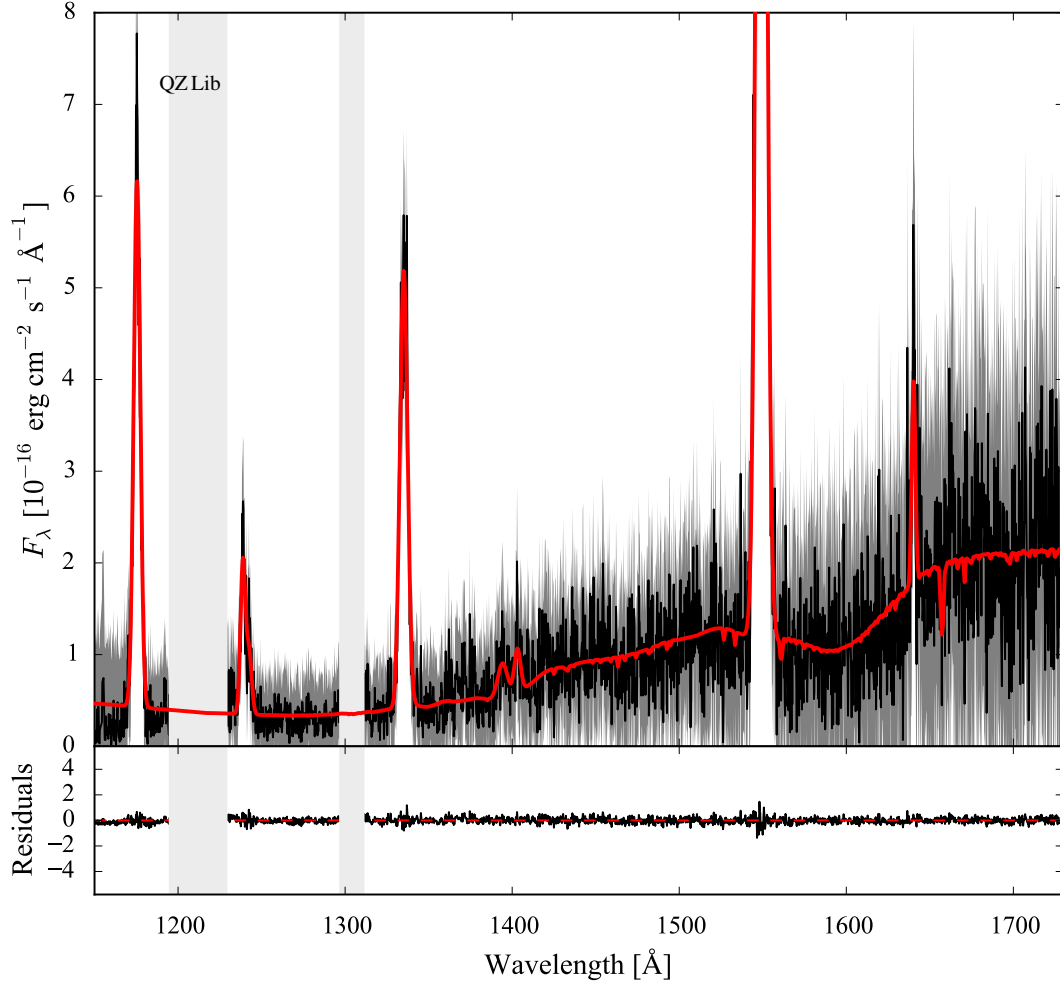| Instrument	STIS
Observation date	2002 Dec 27
$E(B-V)$ (mag)	$0.018^{+0}_{-0.015}$
P_{orb} (min)	100.18
Gaia EDR3 ID	832942871937909632
ϖ (mas)	3.27 ± 0.07
d (pc)	306 ± 6
Z ($Z_\odot$)	0.1
T_{eff} (K)	14692^{+471}_{-394}
R_{WD} ($0.01\,R_\odot$)	1.40 ± 0.13
M_{WD} ($M_\odot$)	$0.57^{+0.08}_{-0.06}$
$\log(g)$	$7.91^{+0.14}_{-0.13}$
$\langle \dot{M} \rangle$ ($10^{-10}\,M_\odot\,\mathrm{yr}^{-1}$)	1.6 ± 0.2
WD contribution	63%

Figure B28. Ultraviolet *HST* spectra (black) of CY UMa along with the best-fitting model (red), computed as described in Section 3.2.

Table B29. Best-fitting parameters for GD 552.

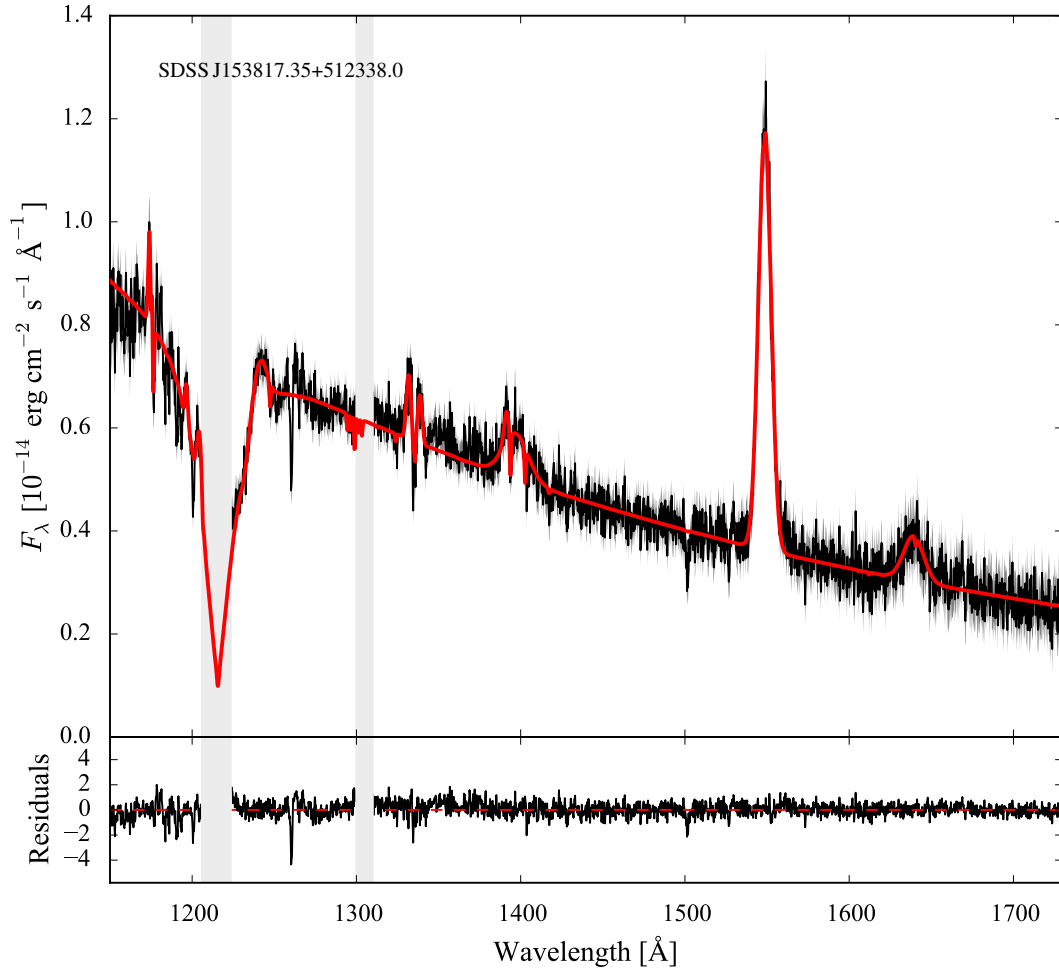| Instrument	STIS
Observation date	2002 Oct 24/2002 Aug 31
$E(B-V)$ (mag)	$0.007^{+0.015}_{-0.007}$
P_{orb} (min)	102.73
Gaia EDR3 ID	2208124536065383424
ϖ (mas)	12.41 ± 0.04
d (pc)	80.6 ± 0.2
Z ($Z_\odot$)	0.1
T_{eff} (K)	10761^{+37}_{-43}
R_{WD} ($0.01\,R_\odot$)	$1.07^{+0.05}_{-0.04}$
M_{WD} ($M_\odot$)	$0.78^{+0.03}_{-0.04}$
$\log(g)$	$8.27^{+0.05}_{-0.06}$
$\langle \dot{M} \rangle$ ($10^{-10}\,M_\odot\,\mathrm{yr}^{-1}$)	$0.243^{+0.023}_{-0.018}$
WD contribution	55%

Figure B29. Ultraviolet *HST* spectra (black) of GD 552 along with the best-fitting model (red), computed as described in Section 3.2.

Table B30. Best-fitting parameters for IY UMa.

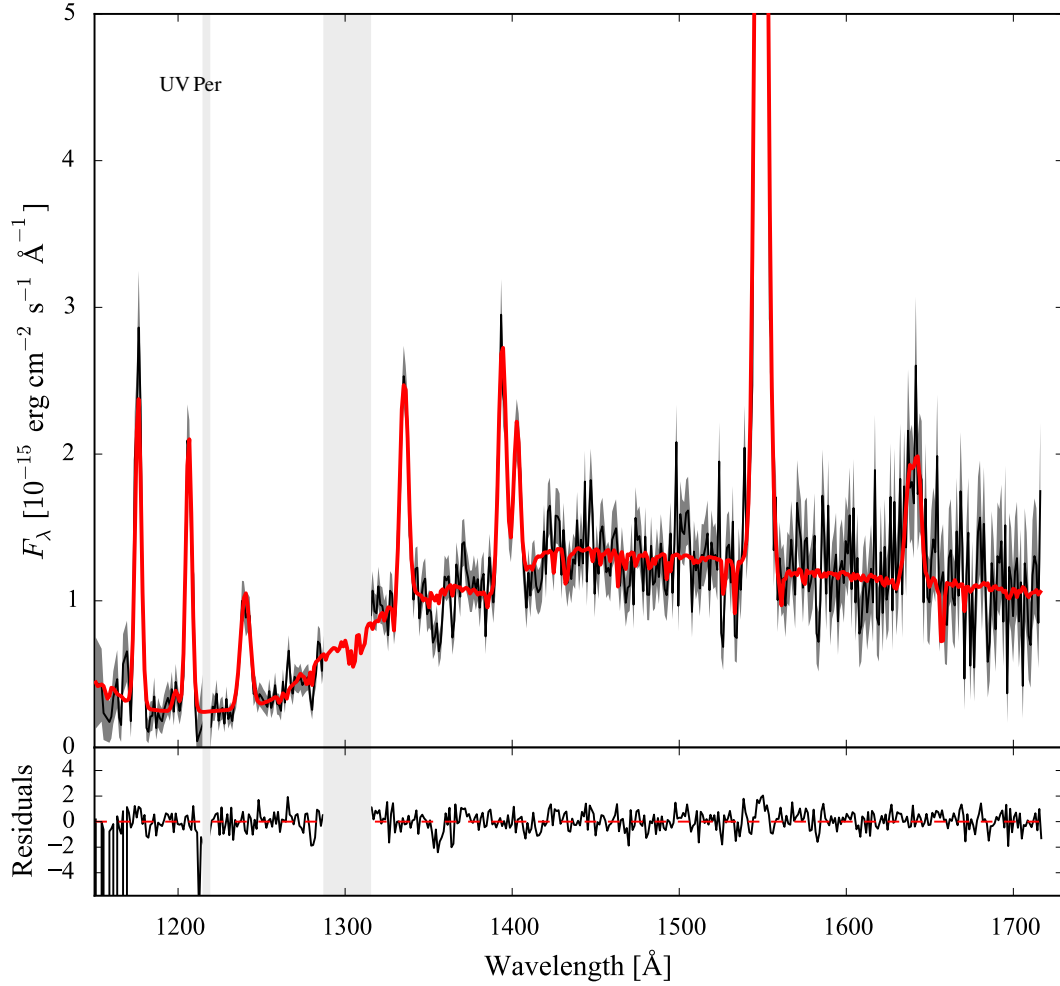| Instrument	COS
Observation date	2013 Mar 30
$E(B-V)$ (mag)	$0.015^{+0}_{-0.015}$
$P_{\rm orb}$ (min)	106.43
Gaia EDR3 ID	855167540988615296
ϖ (mas)	5.52 ± 0.07
d (pc)	181 ± 2
Z ($Z_\odot$)	1.0
$T_{\rm eff}$ (K)	17057^{+179}_{-79}
$R_{\rm WD}$ ($0.01\,{\rm R_\odot}$)	$0.83^{+0.04}_{-0.05}$
$M_{\rm WD}$ ($M_\odot$)	$0.99^{+0.04}_{-0.03}$
$\log(g)$	$8.59^{+0.07}_{-0.05}$
$\langle \dot{M} \rangle$ ($10^{-10}\,{\rm M_\odot\,yr^{-1}}$)	0.85 ± 0.07
WD contribution	79%

Figure B30. Ultraviolet *HST* spectra (black) of IY UMa along with the best-fitting model (red), computed as described in Section 3.2.

Table B31. Best-fitting parameters for SDSS J100515.38+191107.9.

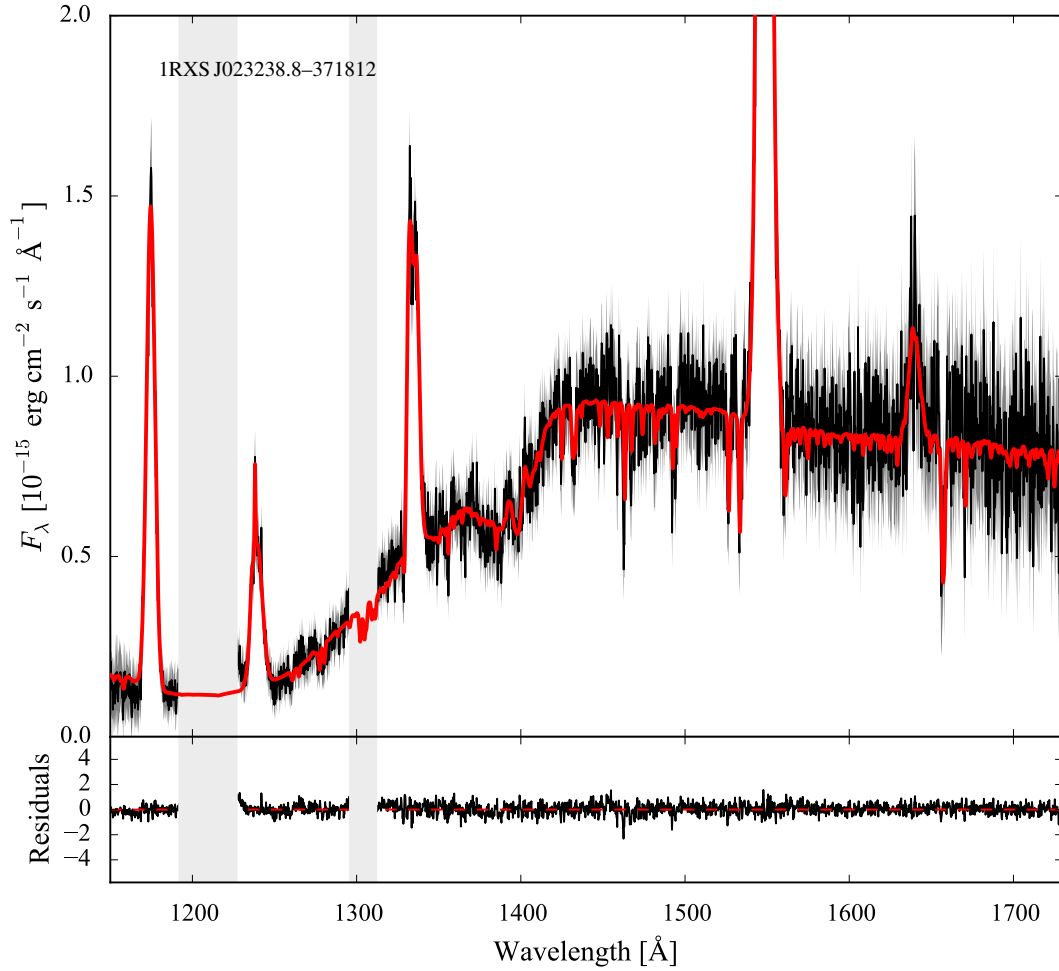| Instrument	COS
Observation date	2013 Jan 31
$E(B-V)$ (mag)	$0.021^{+0.011}_{-0.014}$
$P_{\rm orb}$ (min)	107.6
Gaia EDR3 ID	626719772406892288
ϖ (mas)	2.95 ± 0.17
d (pc)	339^{+21}_{-19}
Z ($Z_\odot$)	0.2
$T_{\rm eff}$ (K)	14483^{+520}_{-430}
$R_{\rm WD}$ ($0.01\,{\rm R_\odot}$)	$1.7^{+0.4}_{-0.3}$
$M_{\rm WD}$ ($\rm M_\odot$)	$0.44^{+0.15}_{-0.09}$
$\log(g)$	7.6 ± 0.3
$\langle \dot{M} \rangle$ ($10^{-10}\,{\rm M_\odot\ yr^{-1}}$)	$2.4^{+1.2}_{-0.8}$
WD contribution	76%

Figure B31. Ultraviolet *HST* spectra (black) of SDSS J100515.38+191107.9 along with the best-fitting model (red), computed as described in Section 3.2.

Table B32. Best-fitting parameters for RZ Leo.

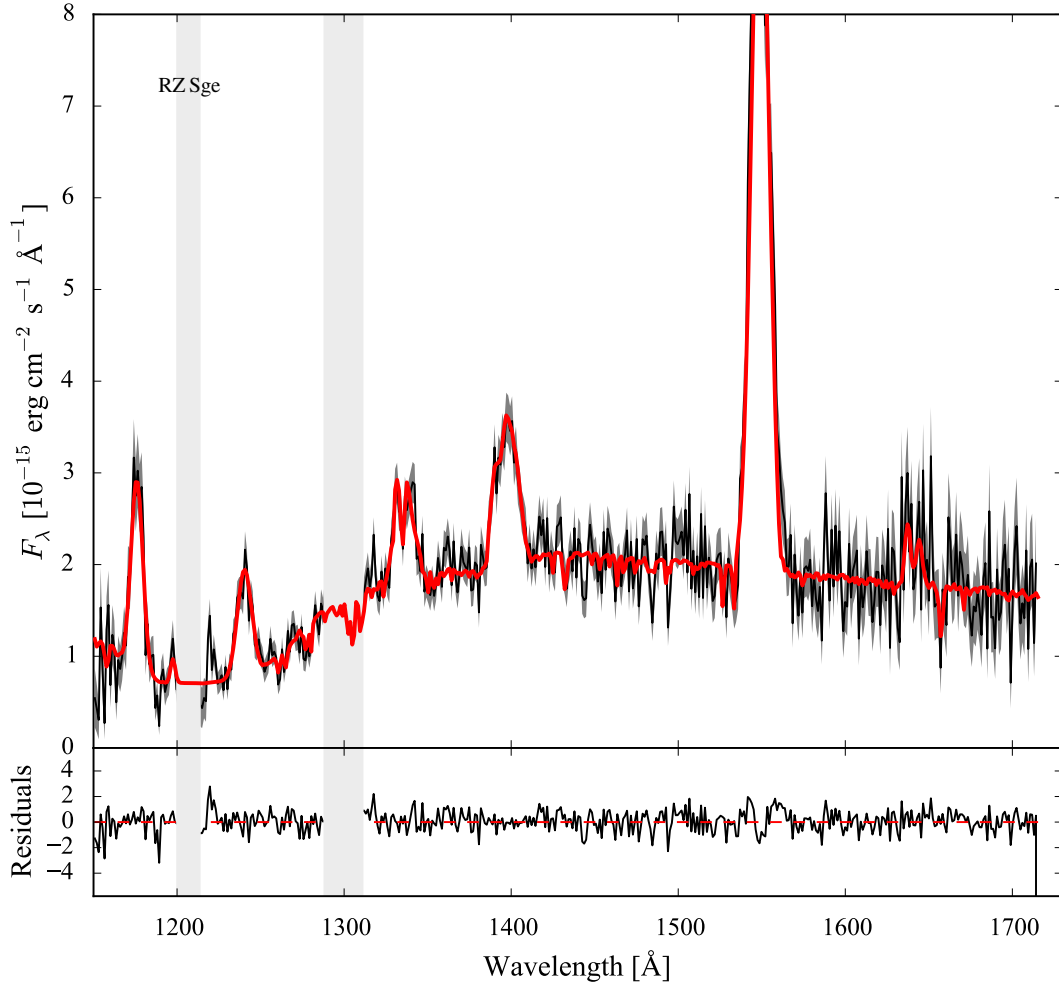| Instrument	COS
Observation date	2013 Apr 11
$E(B-V)$ (mag)	$0.023^{+0.015}_{-0.023}$
$P_{\rm orb}$ (min)	110.17
Gaia EDR3 ID	3799290858445023488
ϖ (mas)	3.59 ± 0.15
d (pc)	279^{+12}_{-11}
Z ($Z_\odot$)	0.5
$T_{\rm eff}$ (K)	15573^{+437}_{-424}
$R_{\rm WD}$ ($0.01\,R_\odot$)	$0.85^{+0.2}_{-0.16}$
$M_{\rm WD}$ ($M_\odot$)	$0.97^{+0.13}_{-0.16}$
$\log(g)$	$8.6^{+0.2}_{-0.3}$
$\langle \dot{M} \rangle$ ($10^{-10}\,M_\odot\,{\rm yr}^{-1}$)	$0.62^{+0.3}_{-0.19}$
WD contribution	81%

Figure B32. Ultraviolet *HST* spectra (black) of RZ Leo along with the best-fitting model (red), computed as described in Section 3.2.

Table B33. Best-fitting parameters for AX For.

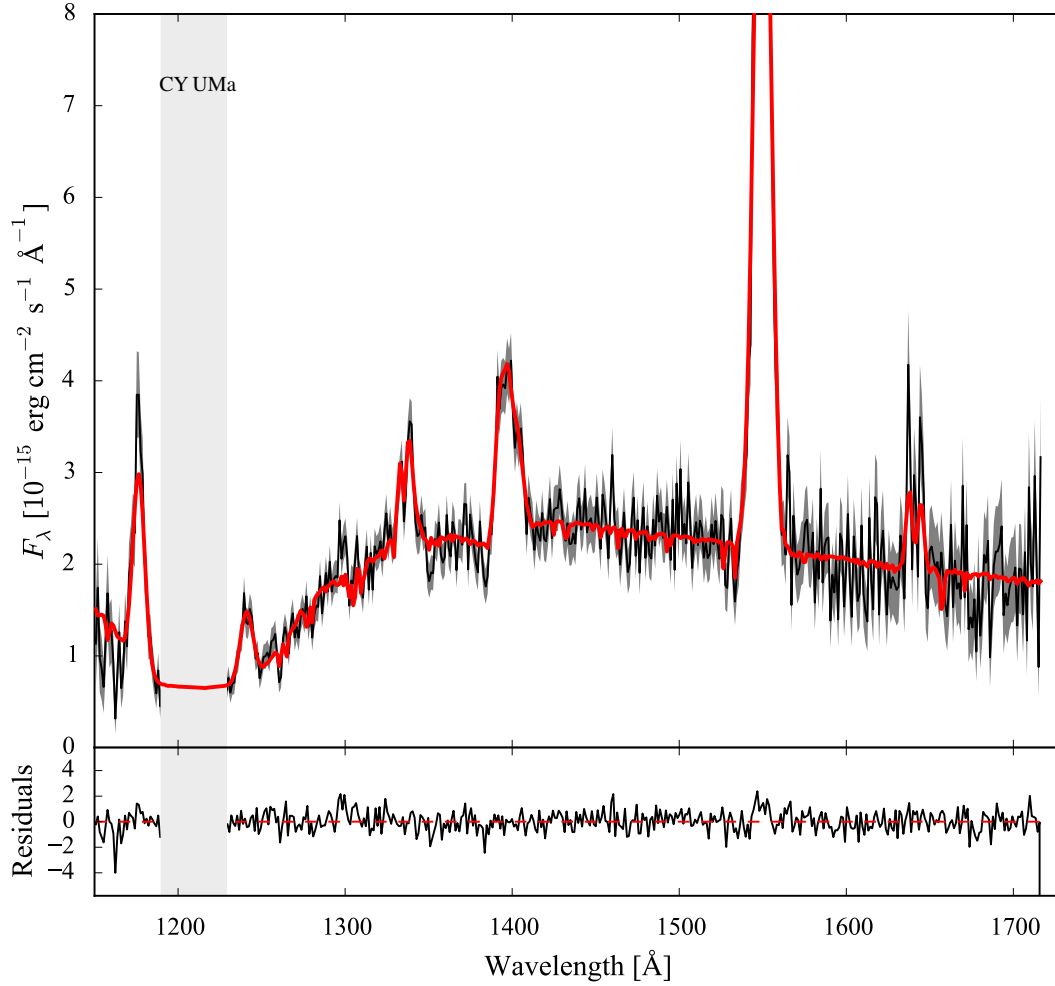| Instrument	COS
Observation date	2013 Jul 11
$E(B-V)$ (mag)	0.018 ± 0.018
P_{orb} (min)	113.04
Gaia EDR3 ID	5067753236787919232
ϖ (mas)	2.86 ± 0.08
d (pc)	349 ± 10
Z ($Z_\odot$)	1.0
T_{eff} (K)	–
R_{WD} ($0.01\,R_\odot$)	$1.09^{+0.08}_{-0.09}$
M_{WD} ($M_\odot$)	0.76 ± 0.07
$\log(g)$	8.24 ± 0.08
$\langle \dot{M} \rangle$ ($10^{-10}\,M_\odot\,\mathrm{yr}^{-1}$)	–
WD contribution	$-\%$

Figure B33. Ultraviolet *HST* spectra (black) of AX For along with the best-fitting model (red), computed as described in Section 3.2.

Table B34. Best-fitting parameters for CU Vel.

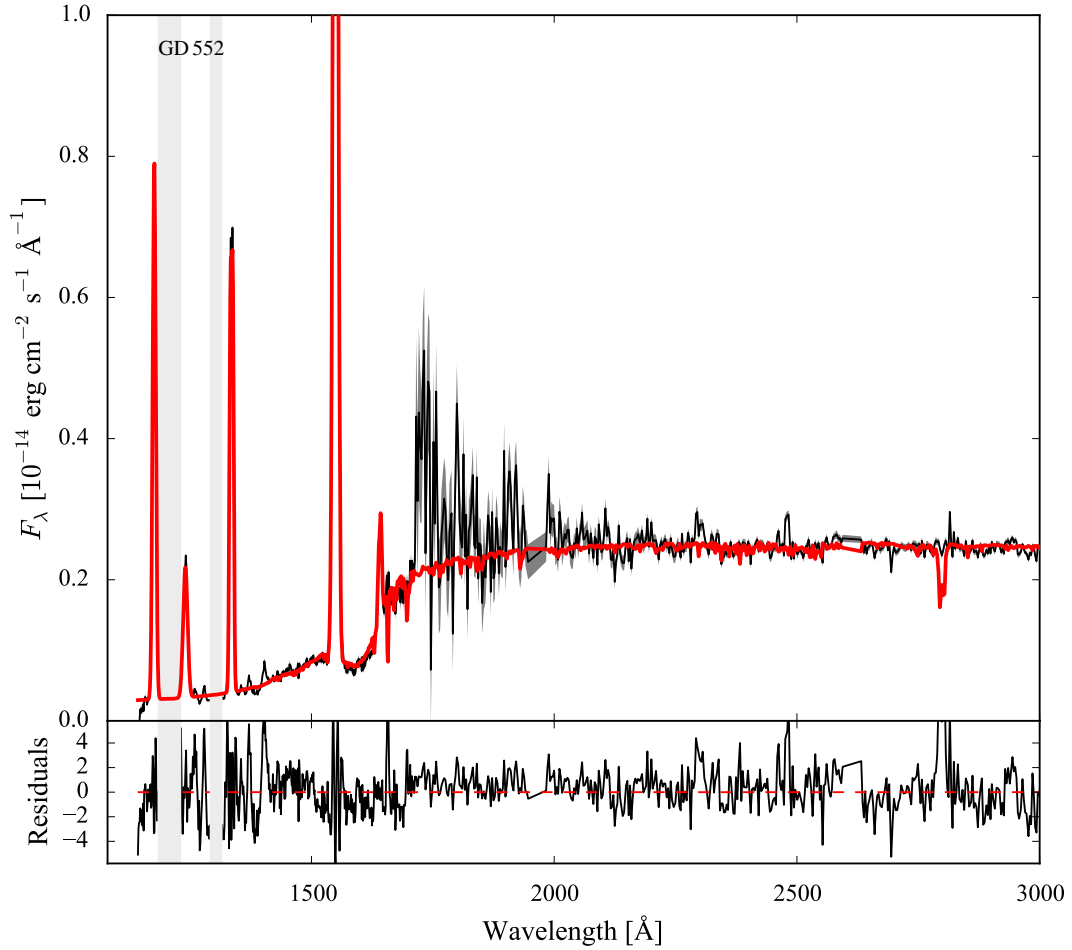| Instrument	COS
Observation date	2013 Jan 18
$E(B-V)$ (mag)	$0.007^{+0.015}_{-0.007}$
P_{orb} (min)	113.04
Gaia EDR3 ID	5524430207364715520
ϖ (mas)	6.31 ± 0.04
d (pc)	158 ± 1
Z ($Z_\odot$)	0.1
T_{eff} (K)	14174^{+117}_{-169}
R_{WD} ($0.01\,R_\odot$)	$1.58^{+0.11}_{-0.08}$
M_{WD} ($M_\odot$)	$0.47^{+0.04}_{-0.05}$
$\log(g)$	$7.71^{+0.08}_{-0.11}$
$\langle \dot{M} \rangle$ ($10^{-10}\,M_\odot\,yr^{-1}$)	$1.97^{+0.28}_{-0.19}$
WD contribution	90%

Figure B34. Ultraviolet *HST* spectra (black) of CU Vel along with the best-fitting model (red), computed as described in Section 3.2.

Table B35. Best-fitting parameters for EF Peg.

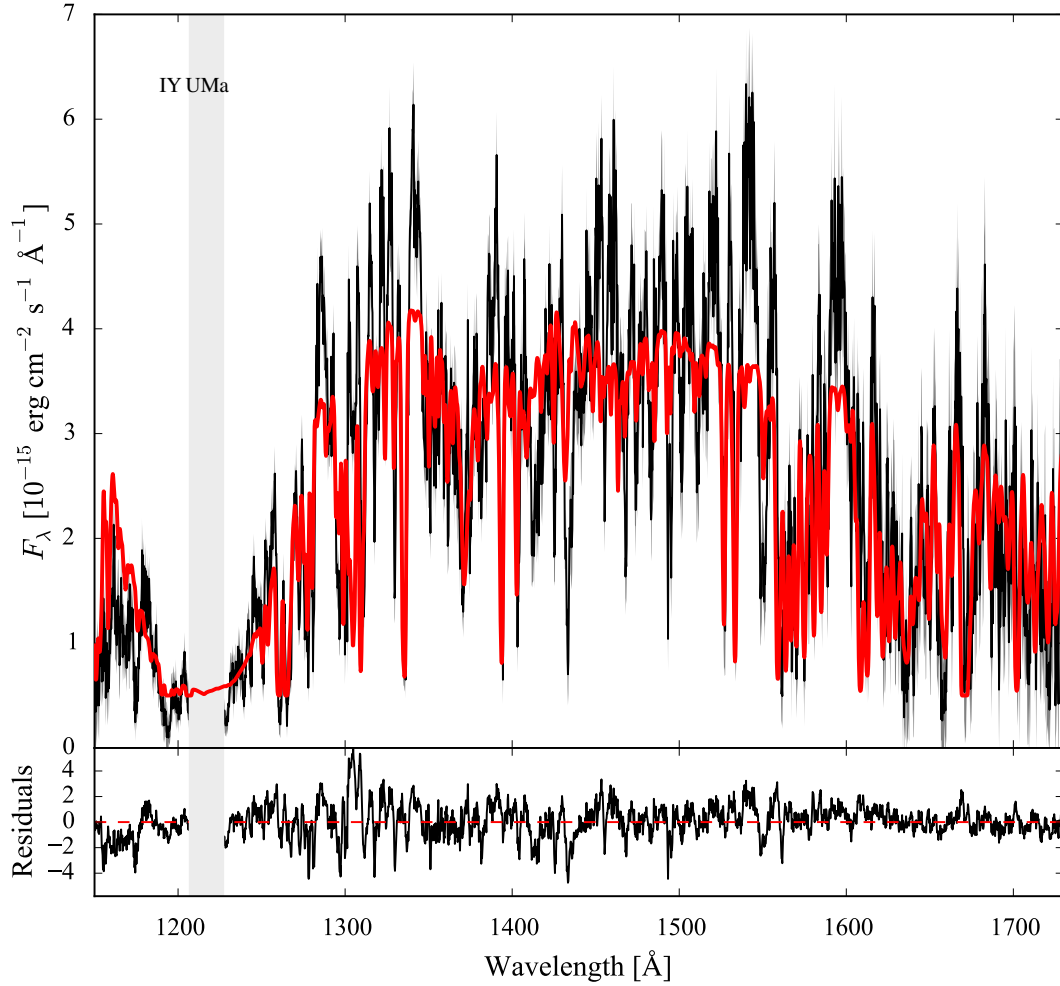| Instrument	STIS
Observation date	2000 Jun 18
$E(B-V)$ (mag)	0.048 ± 0.019
$P_{\rm orb}$ (min)	120.53
Gaia EDR3 ID	1759321791033449472
ϖ (mas)	3.5 ± 0.2
d (pc)	288^{+21}_{-18}
Z (Z$_\odot$)	0.2
$T_{\rm eff}$ (K)	16644^{+448}_{-570}
$R_{\rm WD}$ (0.01 R$_\odot$)	1.1 ± 0.2
$M_{\rm WD}$ (M$_\odot$)	$0.8^{+0.16}_{-0.17}$
$\log(g)$	8.3 ± 0.3
$\langle \dot{M} \rangle$ (10^{-10} M$_\odot$ yr^{-1})	$1.3^{+0.5}_{-0.4}$
WD contribution	90%

Figure B35. Ultraviolet *HST* spectra (black) of EF Peg along with the best-fitting model (red), computed as described in Section 3.2.

Table B36. Best-fitting parameters for DV UMa.

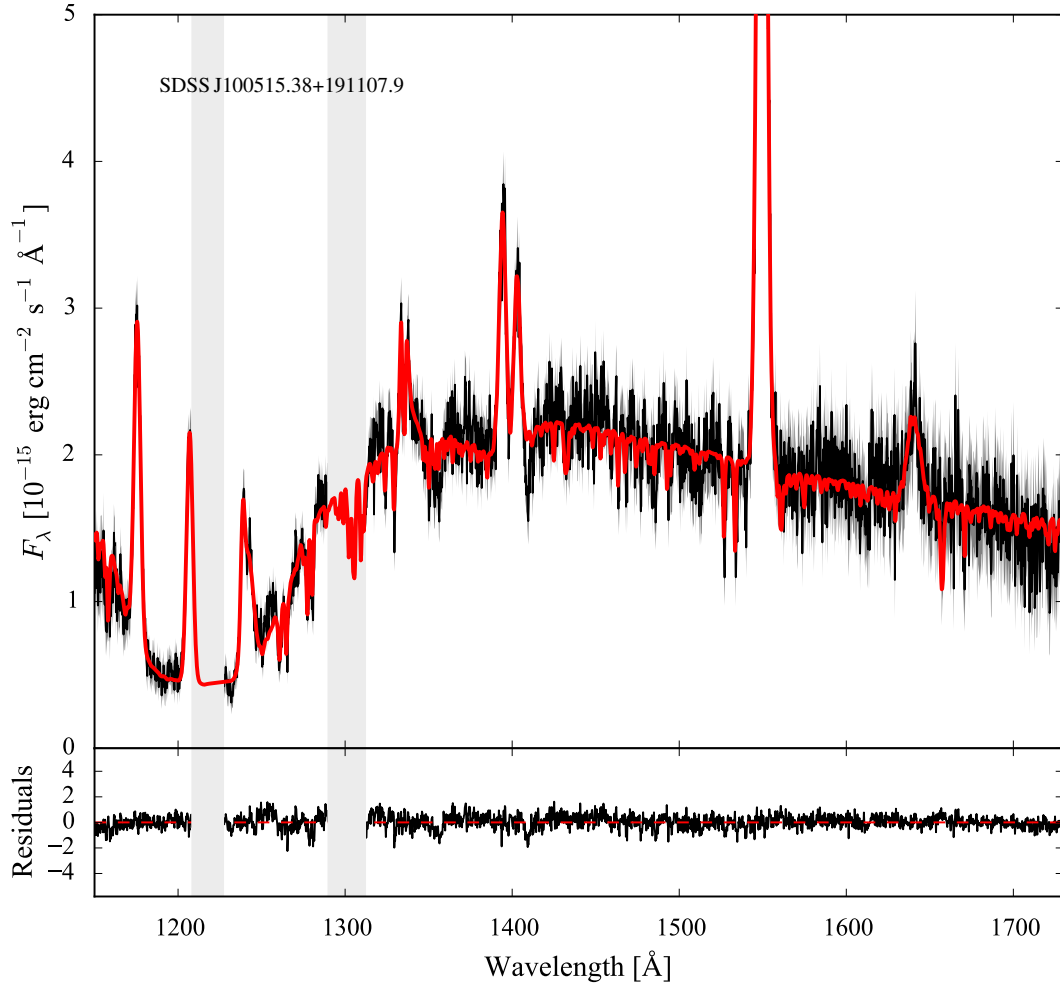| Instrument	STIS
Observation date	2004 Feb 08
$E(B-V)$ (mag)	$0.02^{+0}_{-0.012}$
P_{orb} (min)	123.62
Gaia EDR3 ID	820959638305816448
ϖ (mas)	2.60 ± 0.15
d (pc)	382^{+24}_{-21}
Z ($Z_\odot$)	1.0
T_{eff} (K)	19410^{+244}_{-400}
R_{WD} ($0.01\,R_\odot$)	$0.86^{+0.12}_{-0.09}$
M_{WD} ($M_\odot$)	$0.96^{+0.07}_{-0.1}$
$\log(g)$	$8.55^{+0.13}_{-0.16}$
$\langle \dot{M} \rangle$ ($10^{-10}\,M_\odot\,\mathrm{yr}^{-1}$)	$1.5^{+0.4}_{-0.3}$
WD contribution	89%

Figure B36. Ultraviolet *HST* spectra (black) of DV UMa along with the best-fitting model (red), computed as described in Section 3.2.

Table B37. Best-fitting parameters for IR Com.

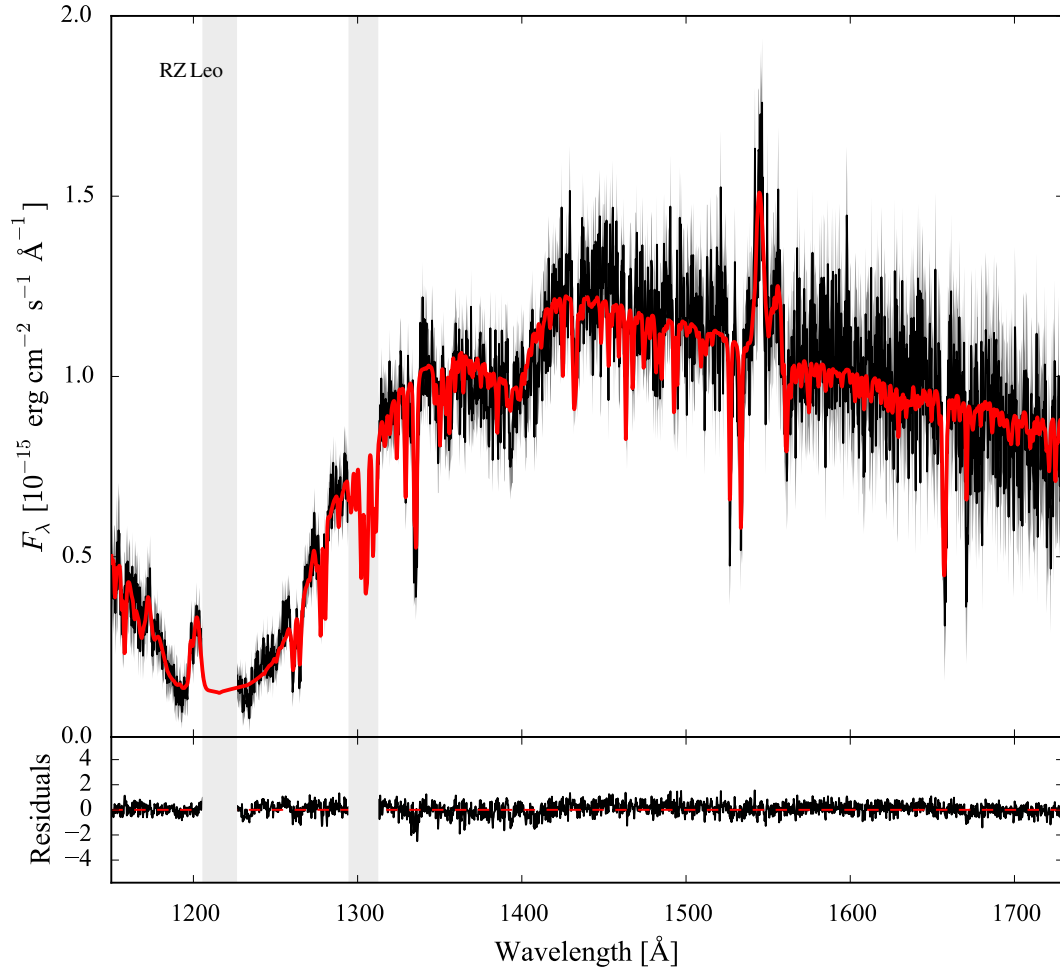| Instrument	COS
Observation date	2013 Jul 11
$E(B-V)$ (mag)	$0.019^{+0.021}_{-0.019}$
$P_{\rm orb}$ (min)	125.34
Gaia EDR3 ID	3955313418148878080
ϖ (mas)	4.63 ± 0.06
d (pc)	216 ± 3
Z ($Z_\odot$)	1.0
$T_{\rm eff}$ (K)	17531^{+236}_{-271}
$R_{\rm WD}$ ($0.01\,{\rm R}_\odot$)	$0.78^{+0.11}_{-0.08}$
$M_{\rm WD}$ (${\rm M}_\odot$)	$1.03^{+0.07}_{-0.09}$
$\log(g)$	$8.67^{+0.12}_{-0.15}$
$\langle \dot{M} \rangle$ ($10^{-10}\,{\rm M}_\odot\,{\rm yr}^{-1}$)	$0.82^{+0.21}_{-0.15}$
WD contribution	87%

Figure B37. Ultraviolet *HST* spectra (black) of IR Com along with the best-fitting model (red), computed as described in Section 3.2.

Table B38. Best-fitting parameters for AM Her.

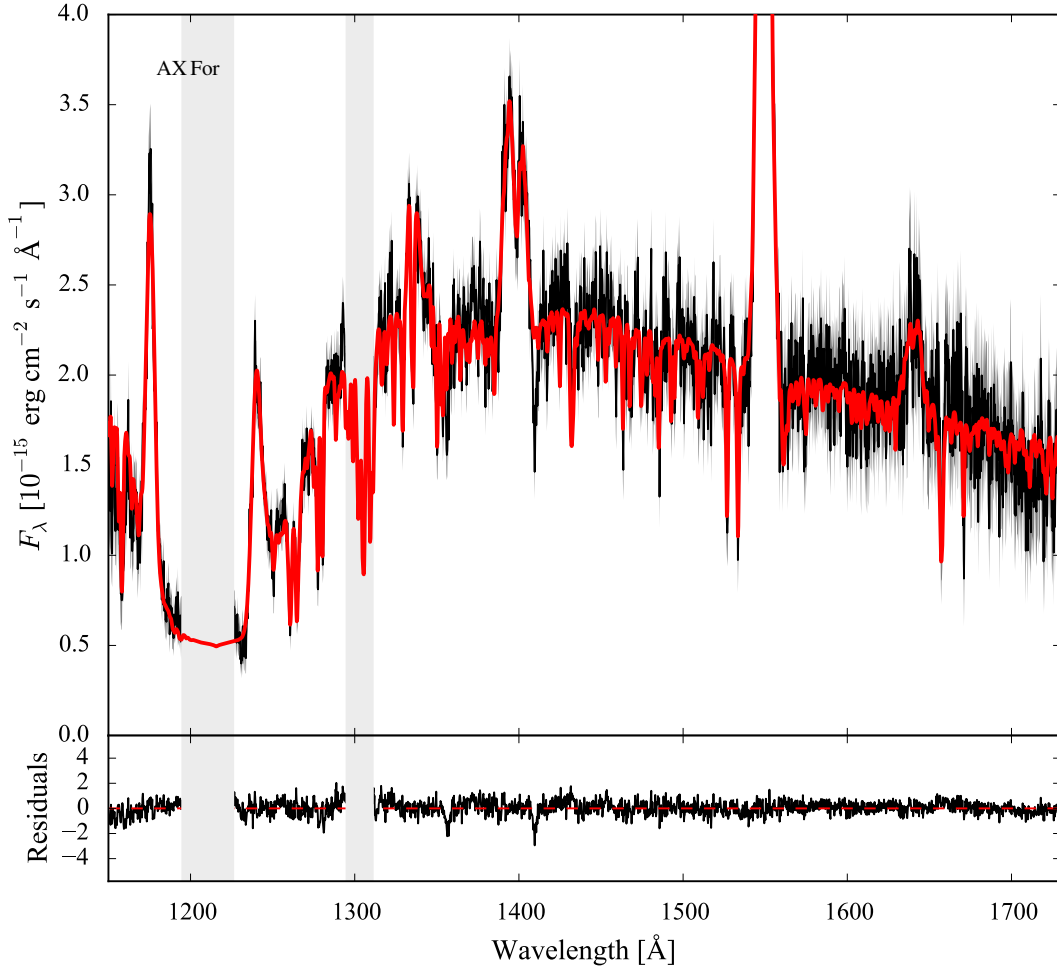| Instrument	STIS
Observation date	2002 Jul 11/12
$E(B-V)$ (mag)	0.017 ± 0.016
P_{orb} (min)	185.65
Gaia EDR3 ID	2123837555230207744
ϖ (mas)	11.37 ± 0.03
d (pc)	87.9 ± 0.2
Z ($Z_{\odot}$)	0.001
T_{eff} (K)	19248^{+486}_{-450}
R_{WD} ($0.01\,R_{\odot}$)	$1.3^{+0.17}_{-0.14}$
M_{WD} ($M_{\odot}$)	$0.63^{+0.1}_{-0.08}$
$\log(g)$	$8.01^{+0.17}_{-0.16}$
$\langle \dot{M} \rangle$ ($10^{-10}\,M_{\odot}\,\mathrm{yr}^{-1}$)	$4.0^{+0.9}_{-0.7}$
WD contribution	92%

Figure B38. Ultraviolet *HST* spectra (black) of AM Her along with the best-fitting model (red), computed as described in Section 3.2.

Table B39. Best-fitting parameters for DW UMa.

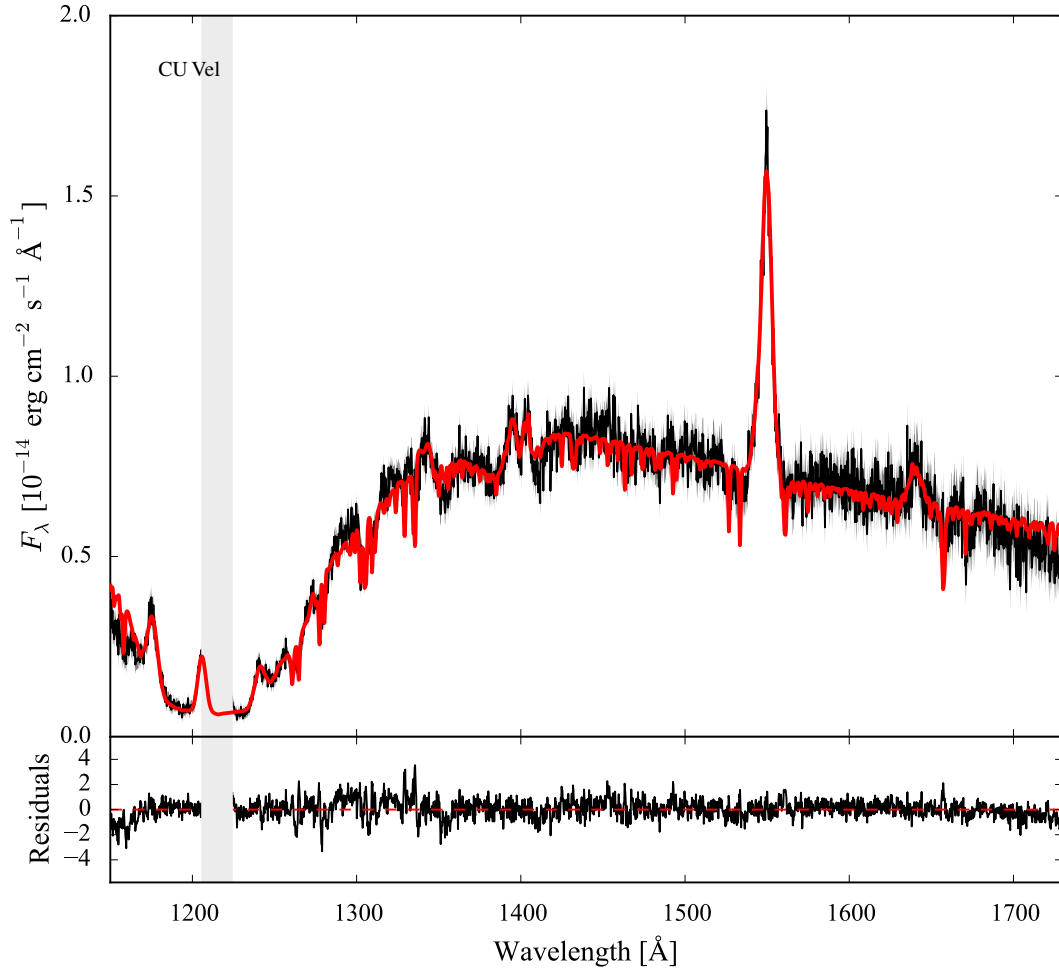| Instrument	STIS
Observation date	1999 Jan 25
$E(B-V)$ (mag)	$0.009^{+0.018}_{-0.009}$
P_{orb} (min)	196.71
Gaia EDR3 ID	855119196836523008
ϖ (mas)	1.73 ± 0.02
d (pc)	579^{+7}_{-6}
Z (Z$_\odot$)	0.71
T_{eff} (K)	56760^{+146}_{-259}
R_{WD} (0.01 R$_\odot$)	$1.19^{+0.07}_{-0.05}$
M_{WD} (M$_\odot$)	$0.82^{+0.03}_{-0.04}$
$\log(g)$	$8.2^{+0.05}_{-0.07}$
$\langle \dot{M} \rangle$ (10^{-10} M$_\odot$ yr^{-1})	228.0 ± 24.0
WD contribution	97%

Figure B39. Ultraviolet *HST* spectra (black) of DW UMa along with the best-fitting model (red), computed as described in Section 3.2.

Table B40. Best-fitting parameters for U Gem.

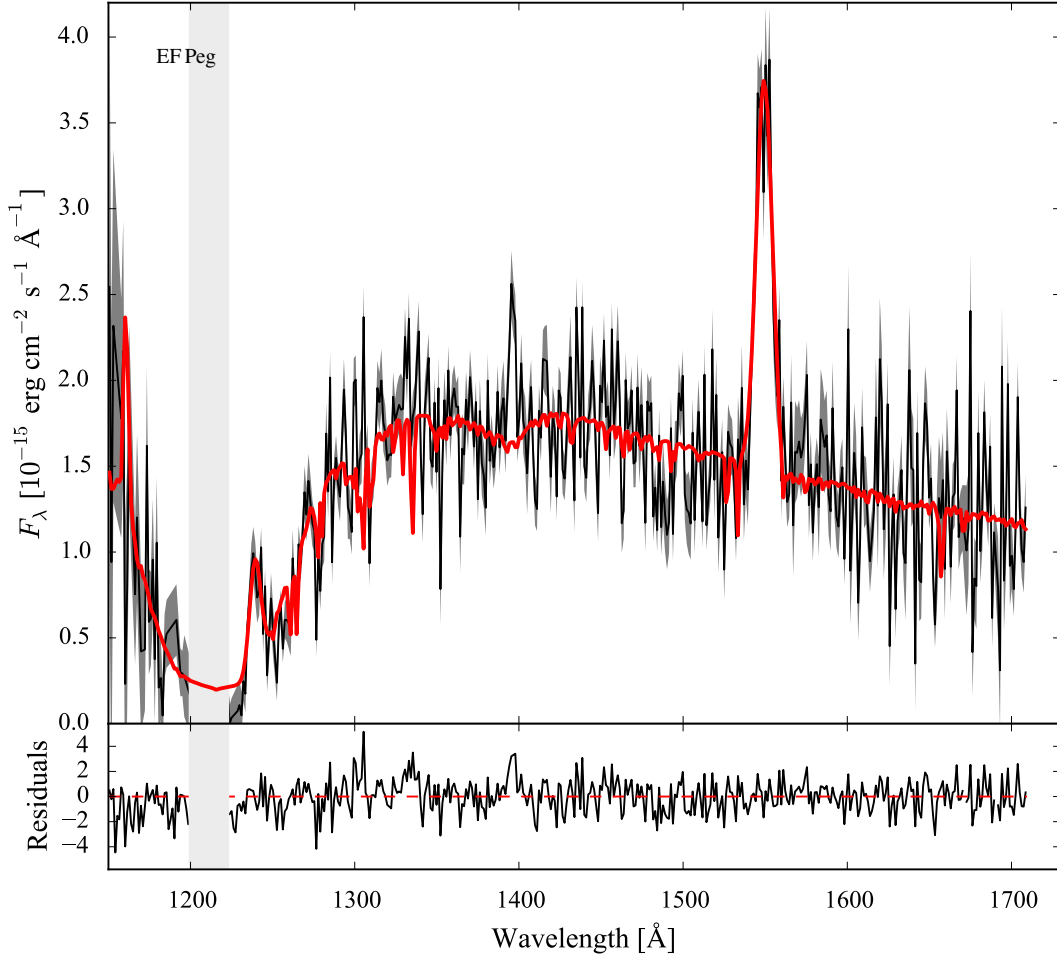| Instrument	FOS
Observation date	1992 Sep 28
$E(B-V)$ (mag)	$0.003^{+0.015}_{-0.003}$
P_{orb} (min)	254.74
Gaia EDR3 ID	674214551557961984
ϖ (mas)	10.75 ± 0.03
d (pc)	93.0 ± 0.3
Z ($Z_\odot$)	1.0
T_{eff} (K)	33070^{+648}_{-616}
R_{WD} ($0.01\,R_\odot$)	0.634 ± 0.016
M_{WD} ($M_\odot$)	1.160 ± 0.013
$\log(g)$	8.90 ± 0.03
$\langle \dot{M} \rangle$ ($10^{-10}\,M_\odot\,\mathrm{yr}^{-1}$)	$6.53^{+0.22}_{-0.17}$
WD contribution	100%

Figure B40. Ultraviolet *HST* spectra (black) of U Gem along with the best-fitting model (red), computed as described in Section 3.2.

Table B41. Best-fitting parameters for SS Aur.

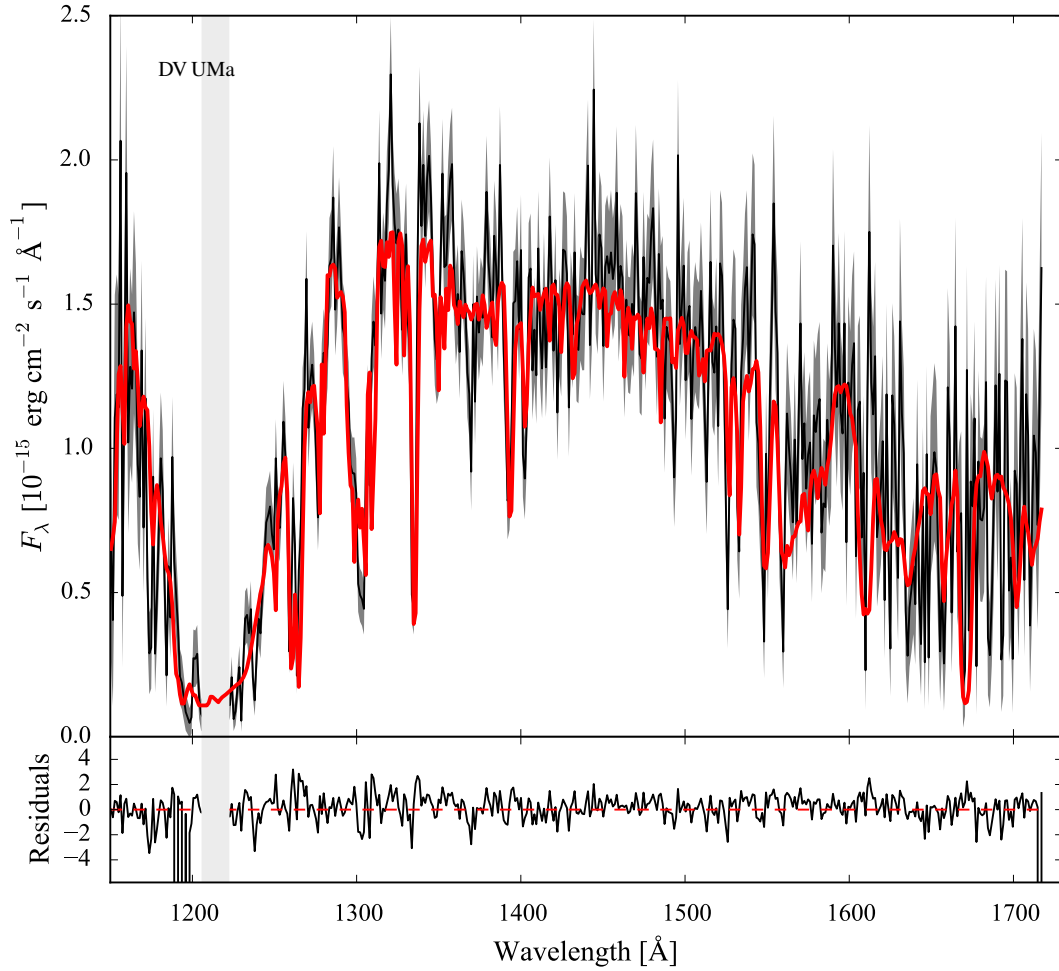| Instrument	STIS
Observation date	2003 Mar 20
$E(B-V)$ (mag)	0.047 ± 0.033
P_{orb} (min)	263.23
Gaia EDR3 ID	968824328534823936
ϖ (mas)	4.02 ± 0.03
d (pc)	249 ± 2
Z ($Z_\odot$)	0.1
T_{eff} (K)	28627^{+190}_{-269}
R_{WD} ($0.01\,R_\odot$)	$0.86^{+0.15}_{-0.11}$
M_{WD} ($M_\odot$)	$0.98^{+0.09}_{-0.11}$
$\log(g)$	$8.56^{+0.16}_{-0.19}$
$\langle \dot{M} \rangle$ ($10^{-10}\,M_\odot\,\mathrm{yr}^{-1}$)	$7.3^{+3.0}_{-1.9}$
WD contribution	100%

Figure B41. Ultraviolet *HST* spectra (black) of SS Aur along with the best-fitting model (red), computed as described in Section 3.2.

Table B42. Best-fitting parameters for RX And.

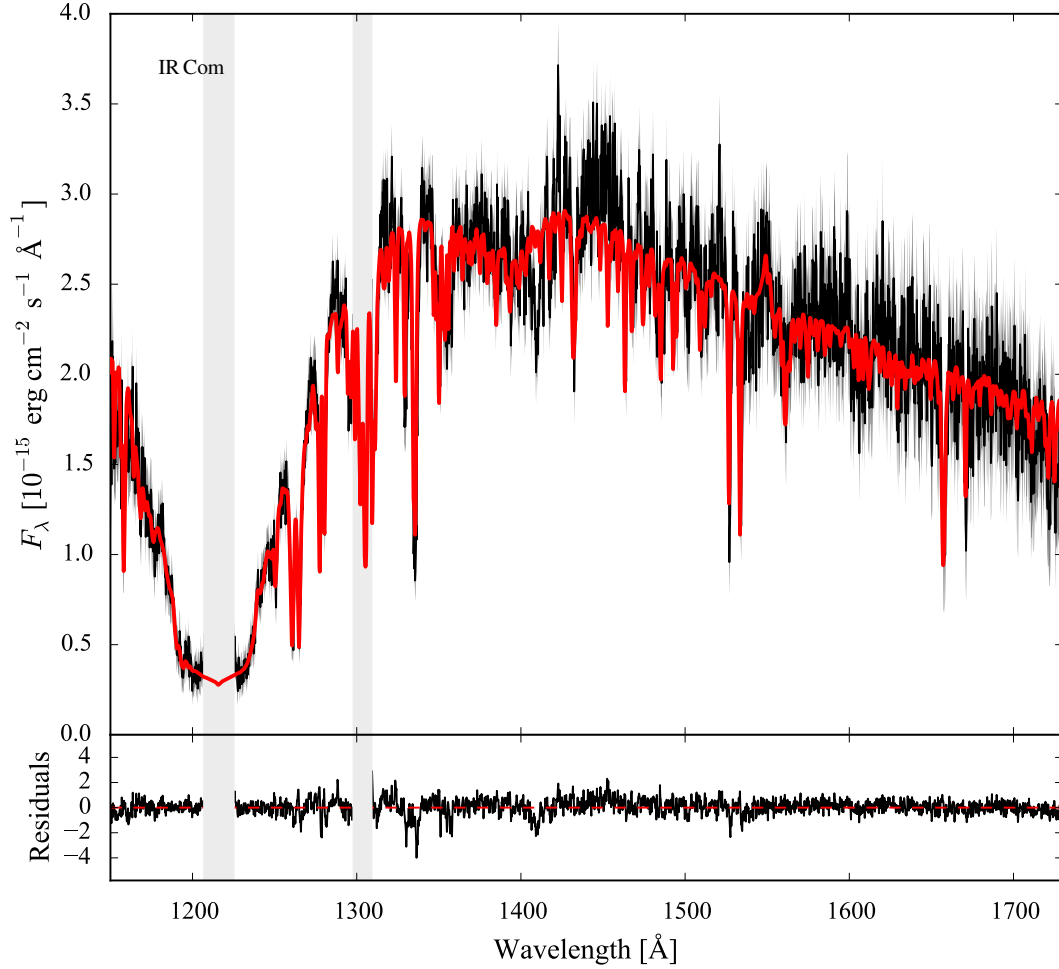| Instrument	GHRS
Observation date	1996 Dec 22
$E(B-V)$ (mag)	0.02 ± 0.02
P_{orb} (min)	302.25
Gaia EDR3 ID	374510294830244992
ϖ (mas)	5.08 ± 0.03
d (pc)	197 ± 1
Z ($Z_\odot$)	0.5
T_{eff} (K)	33900^{+634}_{-995}
R_{WD} ($0.01\,R_\odot$)	$1.12^{+0.12}_{-0.08}$
M_{WD} ($M_\odot$)	$0.81^{+0.06}_{-0.08}$
$\log(g)$	$8.25^{+0.1}_{-0.13}$
$\langle \dot{M} \rangle$ ($10^{-10}\,M_\odot\,\mathrm{yr}^{-1}$)	$26.0^{+6.0}_{-4.0}$
WD contribution	100%

Figure B42. Ultraviolet *HST* spectra (black) of RX And along with the best-fitting model (red), computed as described in Section 3.2.

Table B43. Best-fitting parameters for V442 Cen.

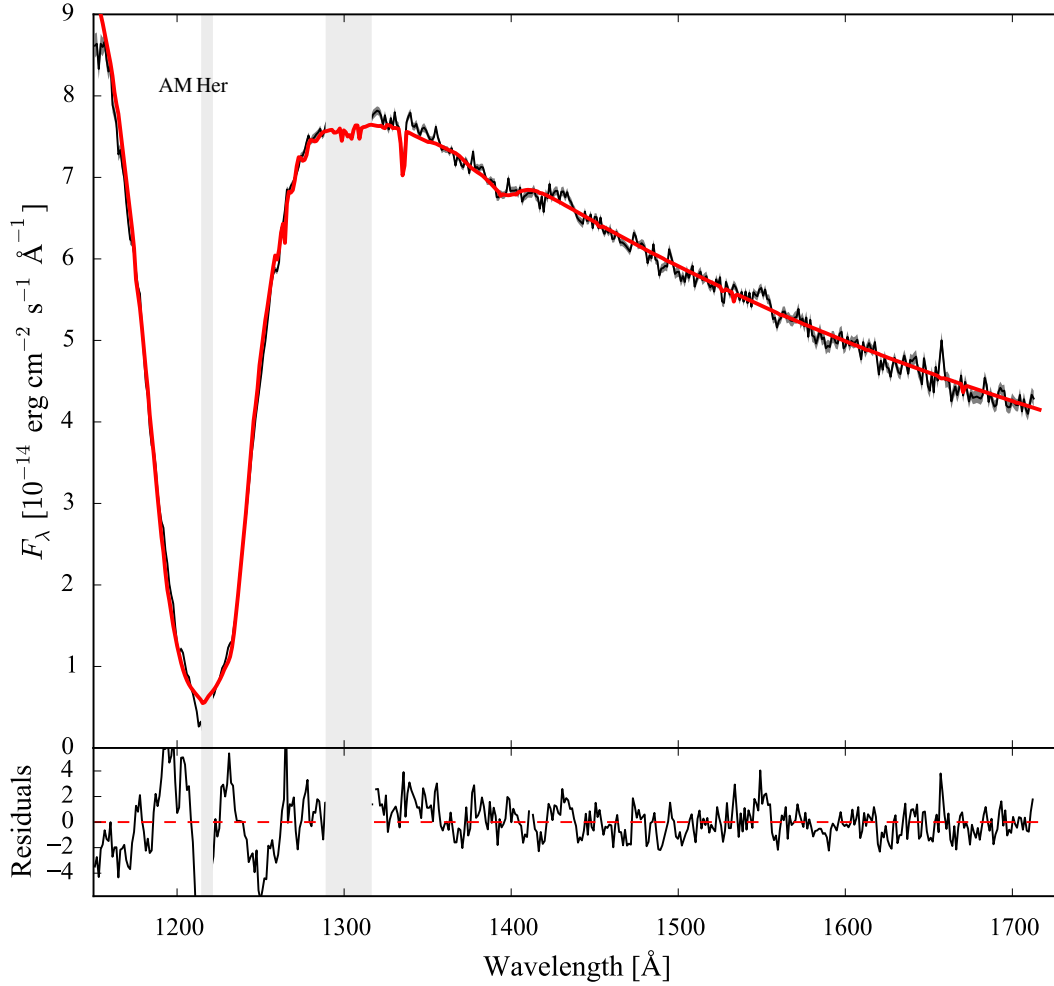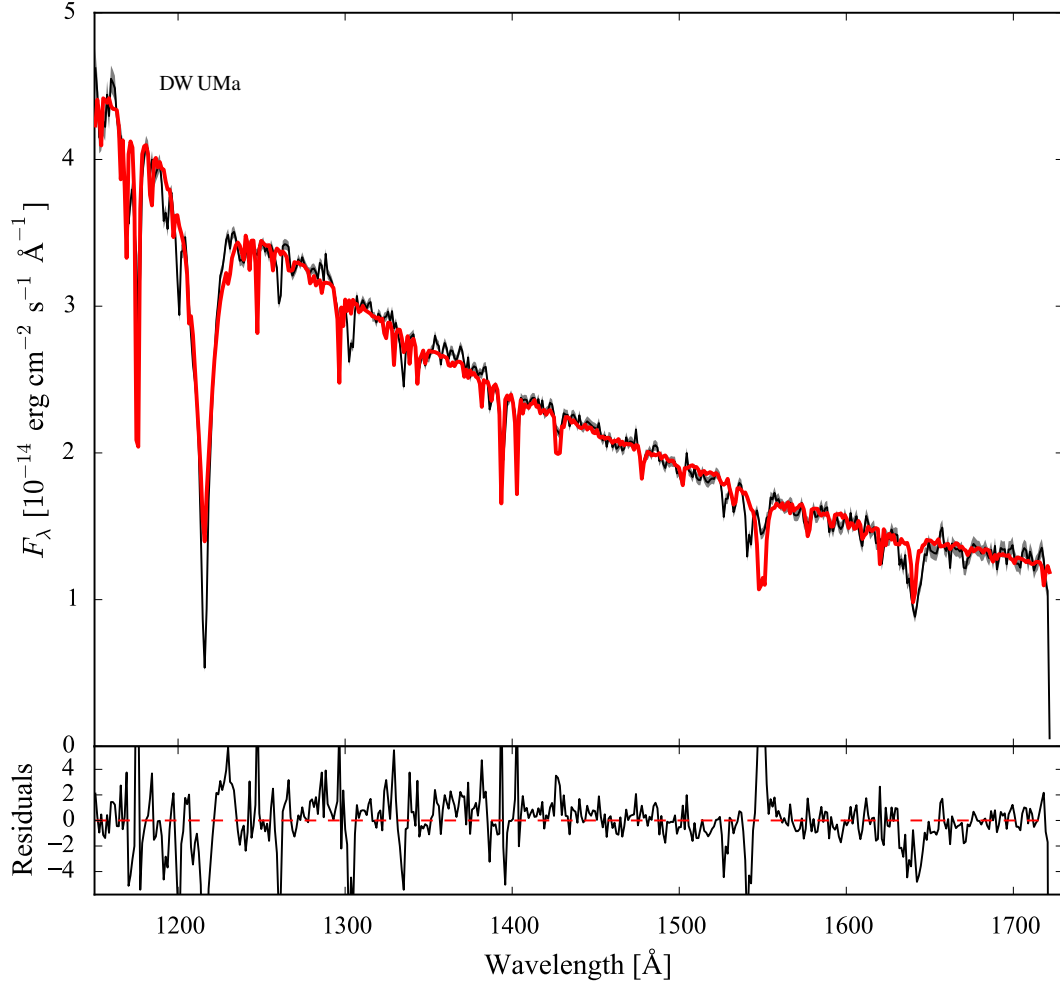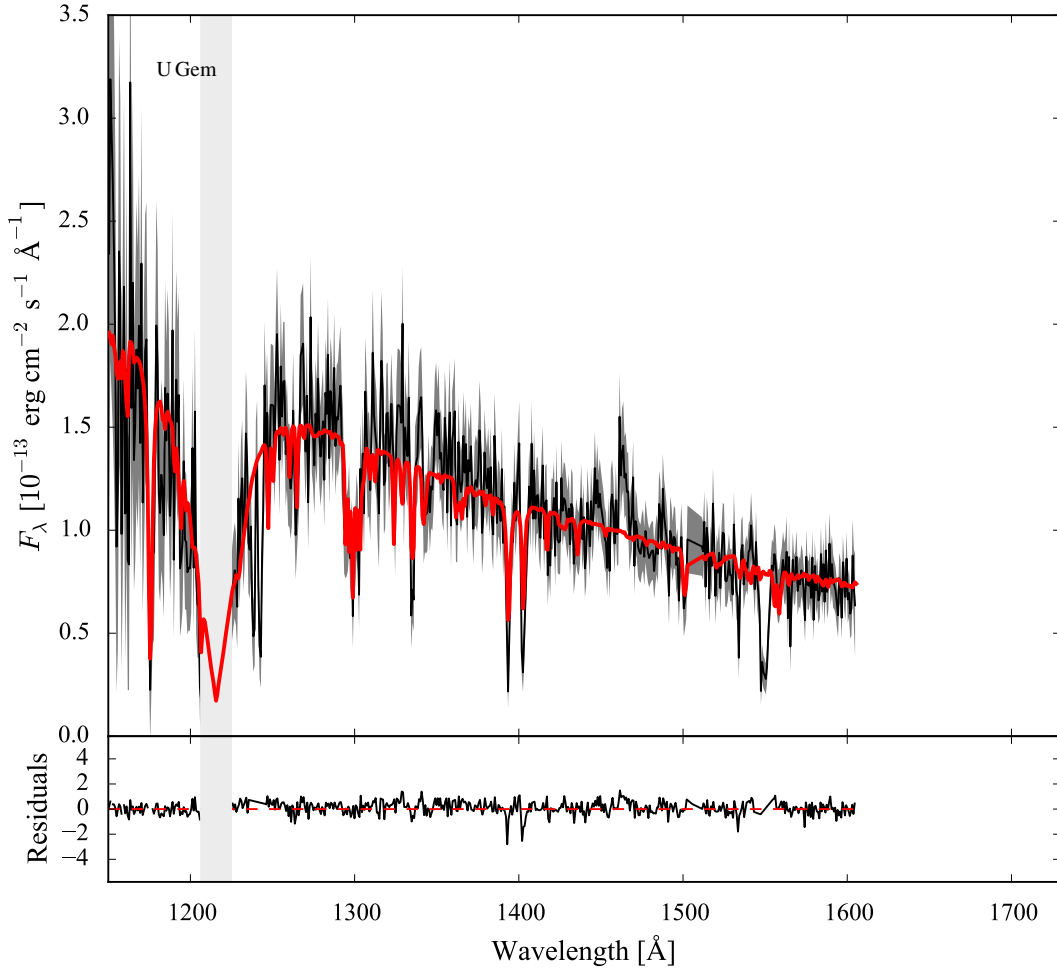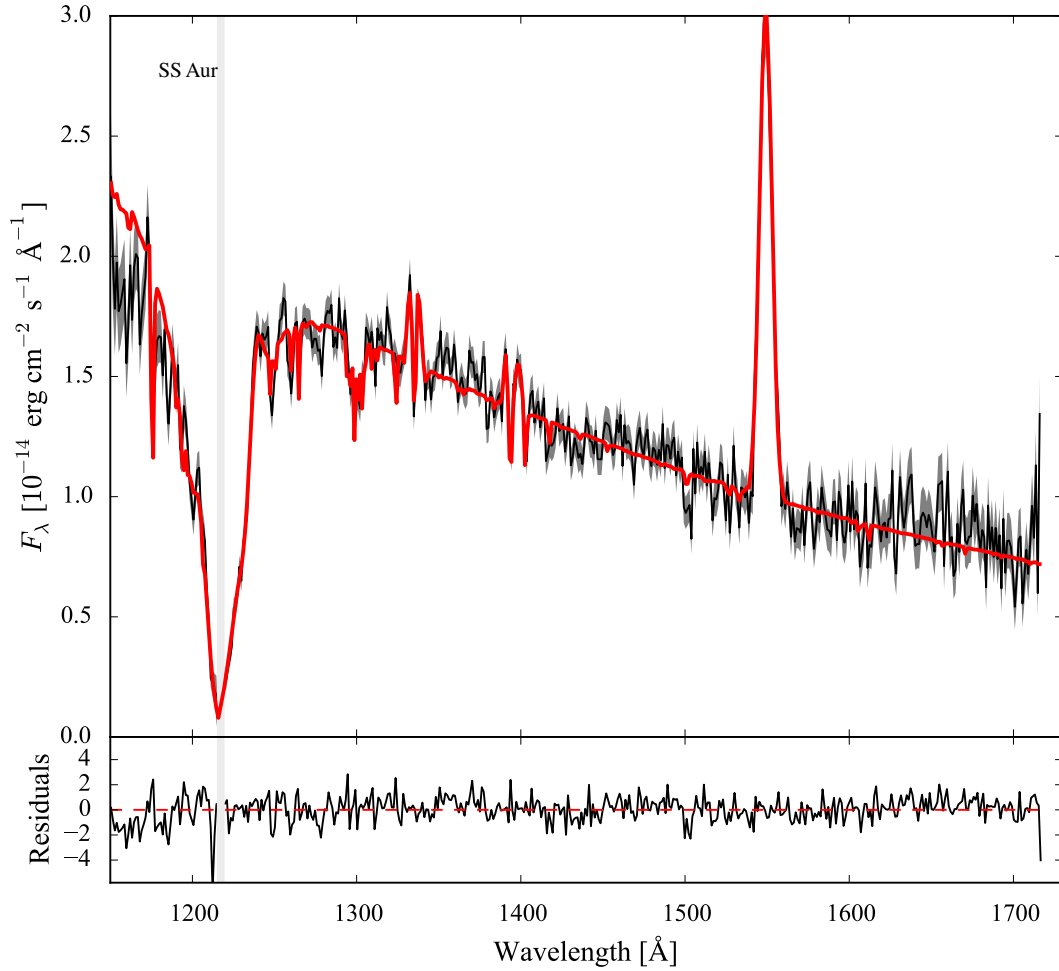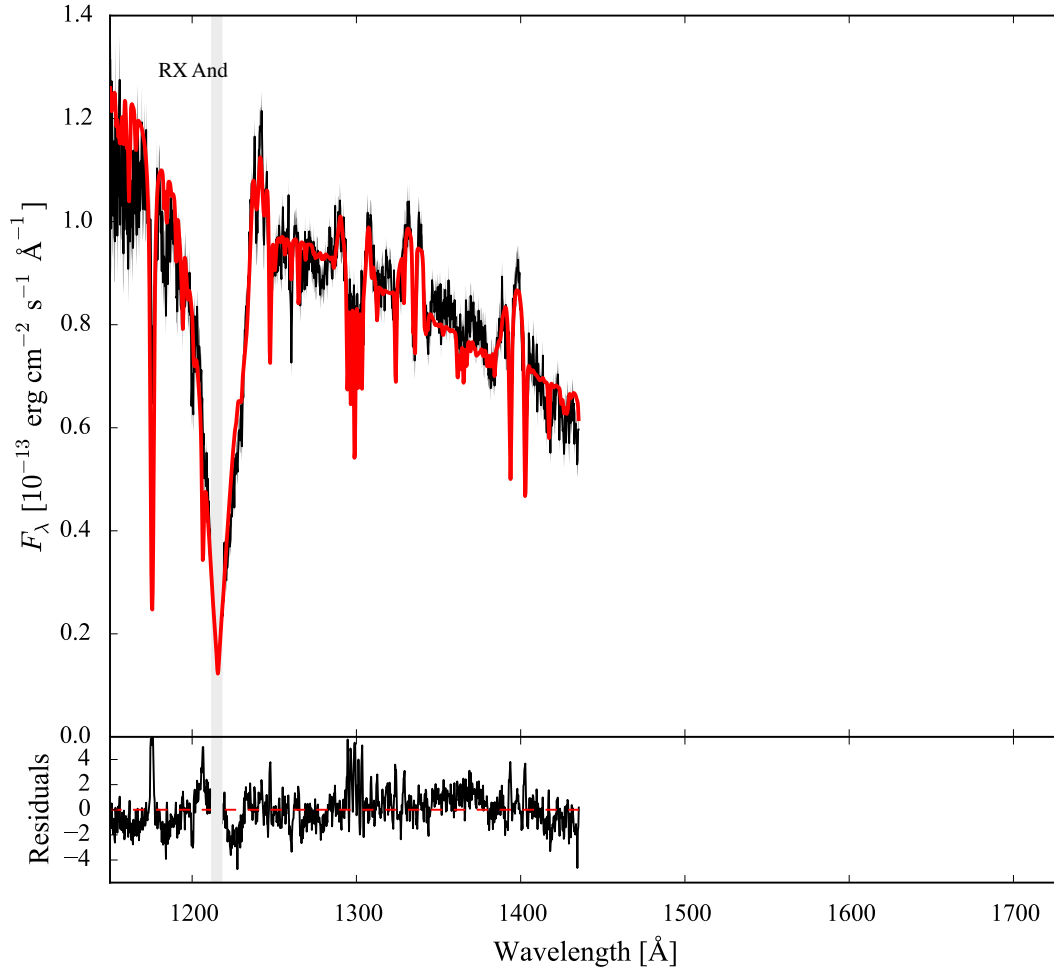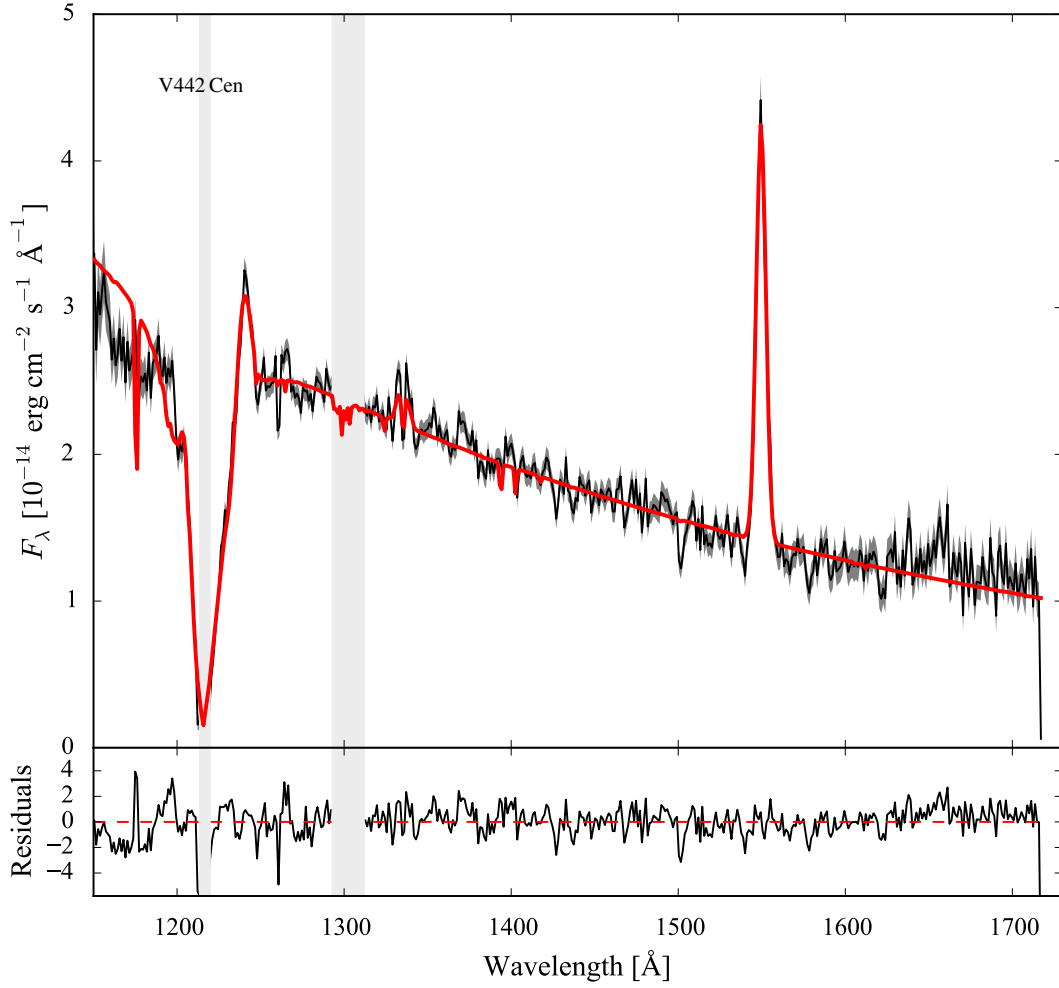| Instrument	STIS
Observation date	2002 Dec 29
$E(B-V)$ (mag)	0.048 ± 0.015
$P_{\rm orb}$ (min)	662.4
Gaia EDR3 ID	5398867830598349952
ϖ (mas)	2.92 ± 0.04
d (pc)	343 ± 5
Z ($Z_\odot$)	0.01
$T_{\rm eff}$ (K)	29802^{+211}_{-247}
$R_{\rm WD}$ ($0.01\,{\rm R_\odot}$)	$1.35^{+0.14}_{-0.12}$
$M_{\rm WD}$ ($\rm M_\odot$)	$0.64^{+0.06}_{-0.05}$
$\log(g)$	7.98 ± 0.12
$\langle \dot{M} \rangle$ ($10^{-10}\,{\rm M_\odot\,yr^{-1}}$)	$25.0^{+5.0}_{-4.0}$
WD contribution	100%

Figure B43. Ultraviolet *HST* spectra (black) of V442 Cen along with the best-fitting model (red), computed as described in Section 3.2.
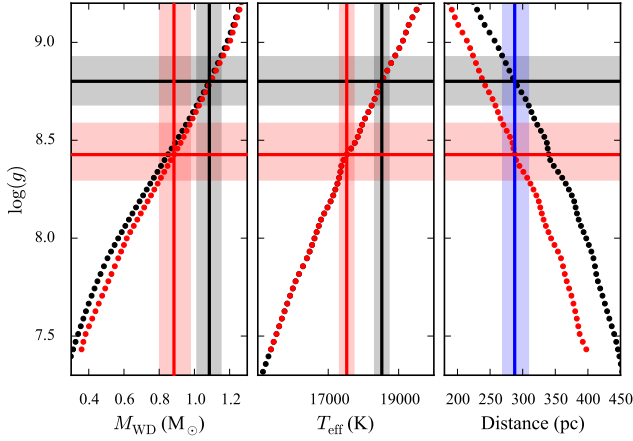
Figure C1. $\log(g)$-M_{WD} (left panel), $\log(g)$-T_{eff} (middle panel) and $\log(g)$-distance relationships (right panel) for EF Peg from Howell et al. (2002) (black dots) and their correction (red dots) accounting for the dependency of the mass-radius relationship on the white dwarf T_{eff} and the reddening. The blue line represents the distance to the system derived from its *Gaia* EDR3 parallax while the black and red lines correspond to the $\log(g)$, M_{WD} and T_{eff} from Howell et al. (2002) and the procedure described in Appendix C, respectively. The shaded areas represent the 1σ statistical uncertainties.

APPENDIX C: CORRECTION APPLIED TO THE $\log(g)$-DISTANCE RELATIONSHIPS FROM THE LITERATURE

The method described by Gänsicke et al. (2005) allows us to investigate of the correlation between $\log(g)$ and the best-fit value for T_{eff}, for different distances. It consists of fitting the ultraviolet data by stepping through a grid of atmosphere models with fixed values for $\log(g)$, leaving the temperature and scaling factor free. For each best-fitting model, the mass and radius of the white dwarf are then computed assuming a mass-radius relationship and the distance to the system is then estimated using Equation 3.

Howell et al. (2002); Szkody et al. (2002a); Gänsicke et al. (2005, 2006) used the above method to compute the $\log(g)$-distance relationship for AM Her, BC UMa, BW Scl, EF Peg, EG Cnc, HV Vir, LL And and SW UMa. However, these works assumed a zero-temperature mass-radius relationship and, therefore, did not account for its dependency on the white dwarf T_{eff}. Moreover, the authors did not apply any reddening correction in their spectral analysis. To take into account these effects, we corrected the $\log(g)$-distance relationship by applying the procedure described in the following, which we illustrate using EF Peg as an example:

 (i) we retrieved the $\log(g)$-M_{WD}, $\log(g)$-T_{eff} and $\log(g)$-distance relationships for EF Peg from the work by Howell et al. (2002) (black dots Figure C1). For each couple of $\log(g)$-M_{WD} values, we computed the corresponding R_{WD}. This, combined with the $\log(g)$-distance provide the scaling factor (S) for each best-fitting model identified by each couple of $\log(g)$-T_{eff} values.
 (ii) To take into account the dependency of the mass-radius relationship on the white dwarf temperature, for each couple of values $\log(g)$-T_{eff}, we computed the corresponding white dwarf M_{WD} and R_{WD} using the mass-radius relationship by Holberg & Bergeron (2006); Tremblay et al. (2011) (red dots in the left panel Figure C1). The difference between the two mass-radius relationships is more important the lower the mass of the white dwarf.
 (iii) To correct the results by Howell et al. (2002) for the reddening, we
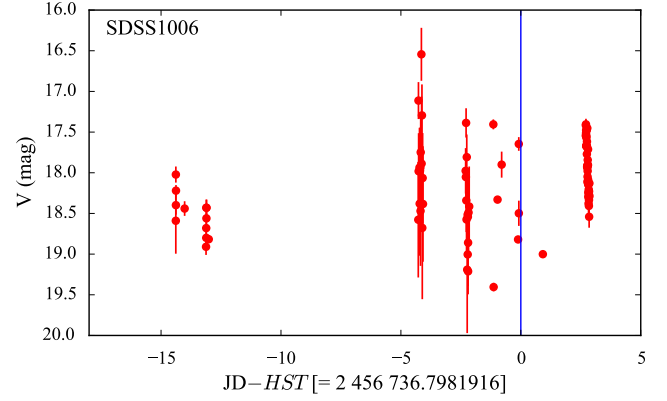
Figure E1. Light curve of SDSS1006 as retrieved from the AAVSO database. The blue line represents the epoch of the *HST* observation, which has been subtracted from the Julian date on the x–axis.

computed the scaling factor (S_{corr}) corresponding to the best-fitting model reddened by $E(B-V)$ using the following equation:

$$S_{\mathrm{corr}} = S \times 10^{0.4 A_\lambda} \qquad (C1)$$

where A_λ is the extinction from Cardelli et al. (1989) and S the scaling factor computed at point 1.

(iv) Combining the R_{WD} computed at point 2 and S_{corr}, we derived the distance to the system (red dots in the right panel in Figure C1). The non-null reddening of EF Peg ($E(B-V) = 0.048$) implies that the computation by Howell et al. (2002) systematically overestimated the distance to the system.

Assuming the distance to the system derived from its *Gaia* EDR3 parallax (vertical blue line), it is now possible to derive the mass of the white dwarf. In the case of EF Peg, $d = 288$ pc, implies $T_{\mathrm{eff}} = 18\,522$ K and $M_{\mathrm{WD}} = 1.08\,\mathrm{M}_\odot$ for the original computation by Howell et al. (2002) (black lines) and $T_{\mathrm{eff}} = 17\,526$ K and $M_{\mathrm{WD}} = 0.88\,\mathrm{M}_\odot$ (red lines) for the corrected relationship we computed. We applied this same procedure to AM Her, BC UMa, BW Scl, EG Cnc, HV Vir, LL And and SW UMa and the corrected masses are reported in Table 6.

APPENDIX D: WHITE DWARF PARAMETERS FROM THE LITERATURE

The following table lists the 54 reliable mass measurements of CV white dwarfs from the literature. A measurement is defined reliable when the white dwarf can be unambiguously detected either in the ultraviolet spectrum (from a broad Lyα absorption profile and, possibly, sharp absorption metal lines) or its ingress and egress can be seen in eclipse light curves.

APPENDIX E: CVS OBSERVED WITH *HST*

E0.1 Notes on individual objects

Systems observed after an outbursts

Pala et al. (2017) reported that IY UMa went into outburst about 25 and five days before the *HST* observations. Nonetheless, we can conclude that the white dwarf emission has returned to the quiescent level, as our white dwarf parameters are consistent (see Section 4.1.1) with the independent measurement by McAllister et al. (2019).

System	$P_{\rm orb}$ (min)	$T_{\rm eff}$ (K)	$M_{\rm WD}$ ($M_\odot$)	$\langle\dot{M}\rangle$ ($M_\odot$ yr^{-1})	Magnetic	Method	Reference
SDSS J150722.30+523039.8	66.61	$11\,300 \pm 1000$	0.89 ± 0.01	$(2.0^{+0.8}_{-0.6}) \times 10^{-11}$	no	eclipse	1
PHL 1445	76.3	$13\,200 \pm 700$	0.73 ± 0.03	$(8.0^{+3.0}_{-2.0}) \times 10^{-11}$	no	eclipse	2
SDSS J143317.78+101123.3	78.11	$12\,700 \pm 1500$	0.86 ± 0.01	$(4.0^{+2.0}_{-1.0}) \times 10^{-11}$	no	eclipse	1
SDSS J123813.73–033932.9	80.52	–	0.98 ± 0.06	–	no	gr	3
V455 And	81.08	$11\,300 \pm 1000$	0.87 ± 0.08	$(2.2^{+1.0}_{-0.7}) \times 10^{-11}$	no	sp	35
WZ Sge	81.6	$14\,900 \pm 250$	0.85 ± 0.04	$(7.0^{+2.0}_{-1.0}) \times 10^{-11}$	no	rv,gr,sp	4,5
ASASSN-17jf	81.78	–	0.669 ± 0.031	–	no		36
SDSS J150137.22+550123.4	81.85	$13\,400 \pm 1100$	$0.72^{+0.02}_{-0.01}$	$(9.0 \pm 3.0) \times 10^{-11}$	no	eclipse	6
SDSS J103533.02+055158.4	82.09	$10\,000 \pm 1100$	0.83 ± 0.01	$(1.6^{+0.8}_{-0.6}) \times 10^{-11}$	no	eclipse	1
SSS100615 J200331–284941	84.53	$13\,600 \pm 1500$	0.88 ± 0.03	$(4.0 \pm 2.0) \times 10^{-11}$	no	eclipse	6
SDSS J150240.98+333423.9	84.83	$11\,800 \pm 1200$	0.71 ± 0.0	$(6.0^{+3.0}_{-2.0}) \times 10^{-11}$	no	eclipse	1
SDSS J090350.73+330036.1	85.07	$13\,300 \pm 1700$	0.87 ± 0.01	$(4.0^{+3.0}_{-2.0}) \times 10^{-11}$	no	eclipse	1
CSS080623 J140454–102702	85.79	$15\,500 \pm 1700$	0.71 ± 0.02	$(1.7^{+0.9}_{-0.6}) \times 10^{-10}$	no	eclipse	6
ASASSN–14ag	86.85	$14\,000^{+2200}_{-2000}$	0.63 ± 0.04	$(2.0^{+2.0}_{-1.0}) \times 10^{-10}$	no	eclipse	7
XZ Eri	88.07	$15\,300 \pm 2400$	0.77 ± 0.02	$(1.2^{+1.0}_{-0.6}) \times 10^{-10}$	no	eclipse	1
ASASSN-16kr	88.17	–	0.952 ± 0.018	–	no	eclipse	36
CRTS SSS11126 J052210–350530	89.56	–	0.760 ± 0.023	–	no	eclipse	36
SDSS J105754.25+275947.5	90.42	$13\,300 \pm 1100$	0.8 ± 0.01	$(6.0 \pm 2.0) \times 10^{-11}$	no	eclipse	8
SDSS J122740.83+513925.0	90.66	$15\,900 \pm 1400$	0.8 ± 0.02	$(1.3^{+0.5}_{-0.4}) \times 10^{-10}$	no	eclipse	1
OY Car	90.89	$18\,600^{+2800}_{-1600}$	0.88 ± 0.01	$(1.6^{+1.3}_{-0.8}) \times 10^{-10}$	no	eclipse	6
CTCV J2354–4700	94.39	$14\,800 \pm 700$	0.94 ± 0.03	$(4.9^{+1.3}_{-1.0}) \times 10^{-11}$	no	eclipse	1
LSQ1725	94.67	–	0.97 ± 0.03	–	yes	eclipse	9
SSS130413 J094551–194402	94.71	–	0.84 ± 0.03	–	no	eclipse	6
CSS110113 J043112–031452	95.11	$14\,500 \pm 2200$	$1.0^{+0.04}_{-0.01}$	$(4.0^{+3.0}_{-2.0}) \times 10^{-11}$	no	eclipse	6
SDSS J115207.00+404947.8	97.56	$15\,900 \pm 2000$	0.62 ± 0.04	$(3.0 \pm 2.0) \times 10^{-10}$	no	eclipse	6
EX Hya	98.25	–	0.78 ± 0.03	–	yes	rv	28
OU Vir	104.7	–	0.7 ± 0.01	–	no	eclipse	1
HT Cas	106.1	$14\,000 \pm 1000$	0.61 ± 0.04	$(2.2^{+1.0}_{-0.7}) \times 10^{-10}$	no	eclipse	10
IY UMa	106.43	$17\,750 \pm 1000$	$0.95^{+0.01}_{-0.03}$	$(9.0^{+3.0}_{-2.0}) \times 10^{-11}$	no	eclipse	6
VW Hyi	107.0	$19\,300 \pm 250$	0.7 ± 0.2	$(3.3^{+0.6}_{-0.4}) \times 10^{-10}$	no	gr	11,12,13
Z Cha	107.28	$16\,300 \pm 1400$	0.8 ± 0.01	$(1.3^{+0.5}_{-0.4}) \times 10^{-10}$	no	eclipse	6
SDSS J090103.94+480911.0	112.15	$14\,900 \pm 2000$	0.75 ± 0.02	$(1.3^{+0.8}_{-0.6}) \times 10^{-10}$	no	eclipse	6
V713 Cep	123.0	$17\,000^{+6000}_{-3000}$	0.7 ± 0.01	$(3.0^{+6.0}_{-2.0}) \times 10^{-10}$	no	eclipse	6
DV UMa	123.63	$17\,400 \pm 1900$	1.09 ± 0.03	$(5.0^{+3.0}_{-2.0}) \times 10^{-11}$	no	eclipse	6
CTCV J1300–3052	128.07	$11\,000 \pm 1000$	0.72 ± 0.02	$(4.0 \pm 2.0) \times 10^{-11}$	no	eclipse	6
SDSS J170213.26+322954.1	144.12	15200 ± 1200	0.91 ± 0.03	$(6.0 \pm 2.0) \times 10^{-11}$	no	eclipse	1
HY Eri	171.32	–	0.42 ± 0.05	–	yes	eclipse,rv	14
AM Her	185.7	$19\,800 \pm 700$	0.78 ± 0.15	$(3.0^{+5.0}_{-1.0}) \times 10^{-10}$	yes	sp	15
DW UMa	196.7	$50\,000 \pm 1000$	0.77 ± 0.07	$(1.4^{+0.6}_{-0.4}) \times 10^{-8}$	no	eclipse	16
HS 0220+0603	214.86	$30\,000 \pm 5000$	0.87 ± 0.09	$(1.1^{+1.3}_{-0.6}) \times 10^{-9}$	no?	eclipse	17
IP Peg	227.8	–	1.16 ± 0.02	–	no	eclipse	18
KIS J1927+4447	238.04	$23\,000 \pm 3000$	0.69 ± 0.07	$(1.0^{+1.0}_{-0.5}) \times 10^{-9}$	no	eclipse	19
GY Cnc	252.64	$25\,900 \pm 2300$	0.88 ± 0.02	$(6.0^{+3.0}_{-2.0}) \times 10^{-10}$	no	eclipse	6
U Gem	254.7	$30\,000 \pm 1000$	1.2 ± 0.05	$(3.1^{+1.2}_{-0.8}) \times 10^{-10}$	no	rv,gr,sp	20,21,22,23,24,25
SDSS J100658.40+233724.4	267.71	$16\,000 \pm 1000$	0.82 ± 0.11	$(1.1^{+1.0}_{-0.5}) \times 10^{-10}$	no	eclipse	6
DQ Her	278.8	–	0.6 ± 0.07	–	yes	rv	26
V1640 Her	299.31	–	0.87 ± 0.01	–	no	rv	27
V347 Pup	334.0	–	0.63 ± 0.04	–	no	rv	29
1RXS J064434.5+334451	387.9	–	0.73 ± 0.07	–	no	eclipse	30
EM Cyg	418.9	–	1.0 ± 0.06	–	no	rv	31
AC Cnc	432.7	–	0.76 ± 0.03	–	no	rv	32
V363 Aur	462.6	–	0.9 ± 0.06	–	no?	rv	32
KIC 5608384	524.32	–	0.46 ± 0.02	–	no	rv	33
AE Aqr	592.8	–	0.63 ± 0.05	–	yes	rv	34

Notes. For OU Vir and SSS130413 J094551–194402, the effective temperatures reported by Savoury et al. (2011) and McAllister et al. (2019) have been obtained during descent from superoutburst and within a month from the last outburst, respectively. We do not include their $T_{\rm eff}$ in our analysis since only represent an upper limit for their quiescent temperatures.

References. (1) Savoury et al. (2011), (2) McAllister et al. (2015), (3) Pala et al. (2019), (4) Long et al. (2004), (5) Steeghs et al. (2007), (6) McAllister et al. (2019), (7) McAllister et al. (2017a), (8) McAllister et al. (2017b), (9) Fuchs et al. (2016), (10) Feline et al. (2005), (11) Gänsicke et al. (2006), (12) Sion et al. (1997), (13) Smith et al. (2006), (14) Beuermann et al. (2020), (15) Gänsicke et al. (2006), (16) Araujo-Betancor et al. (2003), (17) Rodríguez-Gil et al. (2015), (18) Copperwheat et al. (2010), (19) Littlefair et al. (2014), (20) Zhang & Robinson (1987), (21) Sion et al. (1998), (22) Long & Gilliland (1999), (23) Naylor et al. (2005), (24) Long et al. (2006), (25) Echevarría et al. (2007), (26) Horne et al. (1993), (27) Ashley et al. (2020), (28) Echevarría et al. (2016), (29) Thoroughgood et al. (2005), (30) Hernandez et al. (2017), (31) Welsh et al. (2007), (32) Thoroughgood et al. (2004), (32) Thoroughgood et al.

For SDSS J100658.41+233724.4 (SDSS1006), SDSS J040714.78-064425.1 (SDSS0407) and V844 Her, Pala et al. (2017) reported that the *HST* observations have been acquired during the quiescent state. However, from an inspection of the light curve retrieved from the American Association of Variable star Observations (AAVSO) database[11], we noticed that SDSS0407 and V844 Her underwent an outburst within two months before the *HST* observations, while SDSS1006 system showed some level of variability just before the *HST* data were acquired (Figure E1). We therefore did not include these systems in our sample since the analysis of their ultraviolet data would provide only a lower limit on their $M_{\rm WD}$.

Table E1: CVs with ultraviolet *HST* observations providing (at least) the full coverage of the Lyα (1100 − 1600 Å) from the white dwarf photosphere with a resolution $R \simeq 1000 − 3000$. Systems observed in the quiescent phase and in which the white dwarf signature is clearly detected in the spectra have been analysed in this work. For the remaining objects, we specify here why the corresponding data were not suitable for our analysis. The systems are sorted by their orbital periods.

System	α	δ	Period (min)	Instrument	Grating	Central wavelength	Comment
CSS 120422:111127+571239	11:11:26.83	+57:12:38.6	55.37	COS COS	G140L G140L	1105 1280	Evolved donor.
V485 Cen	12:57:23.12	−33:12:05.64	59.03	STIS COS	G140L G140L	1425 1105	Evolved donor.
EI Psc	23:29:54.22	+06:28:11.5	64.18	STIS	G140L	1425	Evolved donor.
SDSS J150722.30+523039.8	15:07:22.11	+52:30:40.46	66.61	COS STIS	G140L G230L	1230 2376	This work.
SDSS J074531.91+453829.5	07:45:31.90	+45:38:29.16	76.0	COS	G140L	1105	This work.
GW Lib	15:19:55.26	−25:00:24.24	76.78	COS	G140L	1105	This work.
SDSS J143544.02+233638.7	14:35:44.01	+23:36:38.84	78.0	COS	G140L	1105	This work.
OT J213806.6+261957	21:38:06.71	+26:19:57.03	78.1	COS	G140L	1105	This work.
BW Scl	23:53:00.99	−38:51:47.67	78.23	STIS	E140M	1425	This work.
V844 Her	16:25:01.74	+39:09:26.2	78.69	STIS	G140L	1425	Obtained after to an outburst.
LL And	00:41:51.51	+26:37:20.75	79.28	STIS	G140L	1425	This work.
GZ Cet	01:37:01.06	−09:12:34.4	79.69	COS	G140L	1105	Evolved donor.
SDSS J013701.06−091234.8	01:37:01.04	−09:12:35.65	79.71	COS	G140L	1105	Evolved donor.
V386 Ser	16:10:33.61	−01:02:23.0	80.52	COS	G140L	1105	Obtained after an outburst.
SDSS J123813.73-033933.0	12:38:13.73	−03:39:32.8	80.52	COS	G140L	1105	UV data analysed in combination with the Gaia parallaxes by Pala et al. (2019).
V455 And	23:34:01.37	+39:21:38.64	81.08	STIS COS COS	G140L G140L G160M	1425 1105 1577	Weak detection of the white dwarf. Obtained after an outburst. Obtained after an outburst.
AL Com	12:32:25.77	+14:20:41.78	81.6	STIS	G140L	1425	This work.
WZ Sge	20:07:36.58	+17:42:14.34	81.63	FOS	G160L	2440	This work.
PU CMa	06:40:47.65	−24:23:13.51	81.63	COS	G140L	1105	Obtained after an outburst.
SW UMa	08:36:42.70	+53:28:38.07	81.81	STIS	G140L	1425	This work.
V1108 Her	18:39:26.14	+26:04:09.97	81.87	COS	G140L	1105	This work.
ASAS J002511+1217.2	00:25:11.04	+12:17:11.79	82.0	COS	G140L	1105	This work.
HV Vir	13:21:03.18	+01:53:28.92	82.18	STIS	G140L	1425	This work.
SDSS J103533.02+055158.4	10:35:33.01	+05:51:59.00	82.22	COS	G140L	1105	This work.
WX Cet	01:17:04.17	−17:56:22.38	83.9	STIS	E140M	1425	This work.
CC Scl	23:15:31.80	−30:48:48.57	84.1	COS	G140L	1105	Obtained after an outburst.
KV Dra	14:50:38.31	+64:03:28.6	84.61	STIS	G140L	1425	White dwarf not detected.
SDSS J075507.70+143547.6	07:55:07.68	+14:35:47.26	84.76	COS	G140L	1105	This work.
SDSS J080434.20+510349.2	08:04:34.15	+51:03:48.71	84.97	COS	G140L	1105	This work.
GQ Mus	11:52:02.42	−67:12:20.6	85.49	FOS	G160L	2440	Classical nova, white dwarf not detected.
FS Aur	05:47:48.36	+28:35:11.2	85.8	STIS	G140L	1425	White dwarf not detected.
EK TrA	15:14:00.09	−65:05:36.68	86.36	STIS	E140M	1425	This work.
EG Cnc	08:43:03.97	+27:51:49.71	86.36	STIS	G140L	1425	This work.
AQ Eri	05:06:13.11	−04:08:07.3	87.75	STIS	G140L	1425	White dwarf not detected.
1RXS J105010.8−140431	10:50:10.59	−14:04:36.95	88.56	COS	G140L	1105	This work.
DP Leo	11:17:15.93	+17:57:42.0	89.8	FOS	G160L	2440	Magnetic, weak white dwarf signature in the UV data. Time-resolved observations

Table E1 – continued from previous page

System	α	δ	Period (min)	Instrument	Grating	Central wavelength	Comment
							available but of too low quality for spectral analysis.
V2051 Oph	17:08:19.09	–25:48:31.7	89.9	FOS	G160L	2440	Weak white dwarf signature, data of too low quality for spectral analysis.
V436 Cen	11:14:00.06	–37:40:47.7	90.0	STIS	G140L	1425	White dwarf not detected.
V347 Pav	18:44:48.14	–74:18:34.1	90.08	STIS	G140L	1425	Magnetic, no time-resolved observations available.
EU UMa	11:49:55.71	+28:45:07.4	90.14	FOS	G130H	1600	Magnetic. Time-resolved observations are available but the white dwarf signature is not detected in the UV spectrum.
BC UMa	11:52:15.79	+49:14:41.68	90.16	STIS	G140L	1425	This work.
VY Aqr	21:12:09.30	–08:49:37.47	90.85	STIS	E140M	1425	This work.
OY Car	10:06:22.10	–70:14:04.6	90.89	FOS	G160L	2440	Obtained in 1991. White dwarf + iron curtain detected but too low quality for spectral analysis.
				FOS	G160L	2440	Obtained in 1992, during an outburst.
MR Uma	11:31:22.38	+43:22:38.66	91.17	COS	G140L	1105	Obtained after an outburst.
QZ Lib	15:36:16.02	–08:39:08.63	92.36	COS	G140L	1105	This work.
SDSS J153817.35+512338.0	15:38:17.35	+51:23:37.98	93.11	COS	G140L	1105	This work.
IX Dra	18:12:31.50	+67:04:45.9	93.31	STIS	G140L	1425	White dwarf not detected.
UV Per	02:10:08.34	+57:11:21.00	93.44	STIS	G140L	1425	This work.
1RXS J023238.8–371812	02:32:38.23	–37:17:54.65	95.04	COS	G140L	1105	This work.
SDSS J093249.57+472523.0	09:32:49.57	+47:25:23.0	95.48	COS	G140L	1105	Evolved donor.
SS UMi	15:51:22.33	+71:45:11.9	97.6	STIS	G140L	1425	White dwarf not detected.
KS UMa	10:20:26.54	+53:04:33.1	97.86	STIS	G140L	1425	White dwarf not detected.
BZ UMa	08:53:44.15	+57:48:40.6	97.91	STIS	E140M	1425	Evolved donor.
EX Hya	12:52:24.22	–29:14:56.0	98.26	FOS	G130H	1600	Magnetic, time-resolved observations available but the white dwarf is not detected in the spectra.
				STIS	G140L	1425	
RZ Sge	20:03:18.44	+17:02:51.57	98.32	STIS	G140L	1425	This work.
TY Psc	01:25:39.35	+32:23:08.9	98.4	STIS	E140M	1425	Obtained in outburst.
CY UMa	10:56:56.95	+49:41:18.38	100.18	STIS	G140L	1425	This work.
VV Pup	08:15:06.79	–19:03:17.7	100.44	STIS	G140L	1425	Magnetic, no time-resolved observations available.
BB Ari	02:44:57.80	+27:31:09.13	101.2	COS	G140L	1105	Obtained after an outburst.
V834 Cen	14:09:07.30	–45:17:16.1	101.52	STIS	G140L	1425	Magnetic, no time-resolved observations available.
GD 552	22:50:40.25	+63:28:37.66	102.73	STIS	G230LB	2375	This work.
					G140L	1425	
DT Oct	18:40:52.39	–83:43:10.59	104.54	COS	G140L	1105	Obtained after an outburst.
HT Cas	01:10:12.96	+60:04:36.3	106.05	FOS	G160L	2440	Obtained in outburst.
IY Uma	10:43:56.63	+58:07:31.60	106.43	COS	G140L	1105	This work.
VW Hyi	04:09:11.28	–71:17:41.4	106.95	FOS	G160L	2440	Obtained in 1993 after an outburst.
				FOS	G160L	2440	Obtained in 1995 after an outburst.
				STIS	E140M	1425	Obtained in 2000 after an outburst.
				STIS	E140M	1425	Obtained in 2001 after an outburst.
SDSS J100515.38+191107.9	10:05:15.41	+19:11:07.5	107.6	COS	G140L	1105	Evolved donor.
WX Hyi	02:09:50.83	–63:18:39.9	107.73	GHRS	G140L	1425	White dwarf not detected.
BK Lyn	09:20:11.20	+33:56:42.4	107.97	STIS	E140M	1425	Nova-like, white dwarf not detected.
V893 Sco	16:15:14.98	–28:37:32.1	109.38	STIS	G140L	1425	White dwarf not detected.
T Pyx	09:04:41.51	–32:22:47.6	109.77	COS	G130M	1055	Recurrent nova, white dwarf not detected.
					G140L	1105	

Table E1 – continued from previous page

System	α	δ	Period (min)	Instrument	Grating	Central wavelength	Comment
RZ Leo	11:37:22.18	+01:48:58.86	110.17	COS	G140L	1105	This work.
SDSS J173008.38+624754.7	17:30:08.36	+62:47:54.5	110.22	STIS	G140L	1425	White dwarf not detected.
CD Ind	21:15:40.98	–58:40:53.6	110.89	STIS	E140M	1425	White dwarf not detected.
V503 Cyg	20:27:17.41	+43:41:22.5	111.89	STIS	G140L	1425	White dwarf not detected.
V2301 Oph	18:00:35.53	+08:10:13.9	112.97	FOS	G160L	2440	Nova like, white dwarf not detected.
CU Vel	08:58:33.09	–41:47:52.54	113.04	COS	G140L	1105	This work.
AX For	02:19:28.01	–30:45:45.96	113.04	COS	G140L	1105	This work.
MR Ser	15:52:47.34	+18:56:25.6	113.47	STIS	G140L	1425	Magnetic, no time-resolved observations available.
SDSS J164248.52+134751.4	16:42:48.51	+13:47:51.51	113.6	COS	G140L	11105	Obtained close to an outburst.
BL Hyi	01:41:00.41	–67:53:27.5	113.64	STIS	G140L	1425	Magnetic, no time-resolved observations available.
ST LMi	11:05:39.77	+25:06:28.6	113.89	STIS	G140L	1425	Magnetic, no time-resolved observations available.
AN UMa	11:04:25.65	+45:03:13.8	114.84	STIS	G140L	1425	Magnetic, no time-resolved observations available.
AR UMa	11:15:44.62	+42:58:22.3	115.92	STIS	G140L	1425	White dwarf not detected.
V1974 Cyg	20:30:31.66	+52:37:50.9	117.01	STIS	E140M	1425	Classical nova, white dwarf not detected.
QZ Ser	15:56:54.48	+21:07:18.93	119.75	STIS COS	G140L G140L	1425 1105	Evolved donor.
EF Peg	21:15:04.11	+14:03:49.15	120.53	STIS	E140M	1425	This work.
DV UMa	09:46:36.55	+44:46:44.62	123.62	STIS	G140L	1425	This work.
HU Aqr	21:07:58.19	–05:17:40.4	125.02	FOS	G160L	2440	Magnetic, time-resolved observations available but the white dwarf is not detected in the spectra.
IR Com	12:39:31.99	+21:08:06.25	125.34	COS	G140L	1105	This work.
EU Cnc	08:51:27.16	+11:46:57.4	125.42	GHRS	G140L	1425	Magnetic, no time-resolved observations available.
UZ For	03:35:28.64	–25:44:21.8	126.53	FOS	G160L	2440	Magnetic, time-resolved observations available but the white dwarf is not detected in the spectra.
UW Pic	05:31:35.66	–46:24:04.5	133.4	STIS	G140L	1425	White dwarf not detected.
QS Tel	19:38:35.81	–46:12:57.0	139.95	FOS	G160L	2440	Magnetic, time-resolved observations available but the white dwarf is not detected in the spectra.
NY Ser	15:13:02.29	+23:15:08.4	140.4	STIS	G140L	1425	White dwarf not detected.
OR And	23:04:37.43	+49:27:23.82	144.4	COS	G140L	1105	Nova like, white dwarf not detected.
SDSS J001153.08-064739.1	00:11:53.08	–06:47:39.2	144.41	COS	G140L	1105	Evolved donor.
V348 Pup	07:12:32.91	–36:05:38.5	146.65	FOS	G160L	2440	Nova-like, white dwarf not detected.
IM Nor	15:39:26.35	–52:19:18.8	147.79	COS	G140L	1105	Recurrent nova.
RXJ1554.2+2721	15:54:12.40	+27:21:51.2	151.87	STIS	G140L	1425	Magnetic, no time-resolved observations available.
V795 Her	17:12:56.18	+33:31:19.3	155.9	FOS	G130H	1600	Nova-like, white dwarf not detected.
TU Men	04:41:40.75	–76:36:45.52	168.77	STIS	G140L	1425	Obtained after an outburst.
AM Her	18:16:13.18	+49:52:05.21	185.65	STIS	G140L	1425	This work.
MV Lyr	19:07:16.29	+44:01:08.6	191.38	STIS	G140L	1425	White dwarf not detected.
V482 Cam	07:33:41.42	+67:32:15.6	192.41	STIS	G140L	1425	Nova-like, white dwarf not detected.
SDSS J080908.39+381406.2	08:09:08.40	+38:14:06.1	193.01	STIS	G140L	1425	Nova-like, white dwarf not detected.
DW UMa	10:33:52.88	+58:46:54.74	196.71	STIS	G140L	1425	This work.
TT Ari	02:06:53.09	+15:17:41.8	198.07	FOS	G160L	2440	Nova-like, white dwarf not detected.

Table E1 – continued from previous page

System	α	δ	Period (min)	Instrument	Grating	Central wavelength	Comment
V603 Aql	18:48:54.64	+00:35:02.9	199.01	GHRS	G140L	1425	Nova-like, white dwarf not detected.
				FOS	G160L	2440	
V1500 Cyg	21:11:36.61	+48:09:02.4	201.04	FOS	G160L	2440	Classical nova, white dwarf not detected.
V1432 Aql	19:40:11.42	–10:25:25.8	201.94	FOS	G160L	2440	Magnetic, time-resolved observations available but the white dwarf is not detected in the spectra.
HV And	00:40:55.37	+43:24:59.6	202.03	STIS	G140L	1425	Nova-like, white dwarf not detected.
1ES 0439-68.2	04:39:49.7	–68:09:02	202.03	COS	G130M	1291	Super-Soft X-ray source.
MN Hya	09:29:07.04	–24:05:05.5	203.39	FOS	G160L	2440	Magnetic, time-resolved observations available but the white dwarf is not detected in the spectra.
LS Cam	05:57:23.97	+72:41:52.4	205.03	STIS	G140L	1425	Magnetic, no time-resolved observations available.
V751 Cyg	20:52:12.80	+44:19:26.0	208.03	STIS	G140L	1425	White dwarf not detected.
VZ Sex	09:44:31.71	+03:58:05.6	214.13	STIS	G140L	1425	White dwarf not detected.
HS 0455+8315	05:06:48.28	+83:19:23.3	214.16	STIS	G140L	1425	Nova-like, white dwarf not detected.
V1294 Tau	04:00:37.26	+06:22:45.9	214.59	STIS	G140L	1425	Nova-like, white dwarf not detected.
AO Psc	22:55:17.99	–03:10:40.0	215.46	STIS	E140M	1425	Magnetic, time-tag, da analizzare?.
BP Lyn	09:03:08.89	+41:17:47.6	220.05	STIS	E140M	1425	Nova-like, white dwarf not detected.
V794 Aql	20:17:33.91	–03:39:51.0	220.75	STIS	G140L	1425	Nova-like, white dwarf not detected.
V380 Oph	17:50:13.63	+06:05:29.3	221.01	STIS	G140L	1425	White dwarf not detected.
BZ Cam	06:29:34.09	+71:04:37.0	221.08	GHRS	G140L	1425	Nova-like, white dwarf not detected.
BB Dor	05:29:28.58	–58:54:46.04	221.9	COS	G140L	1105	Nova like, white dwarf not detected.
GS Pav	20:08:07.62	–69:48:58.7	223.59	STIS	G140L	1425	White dwarf not detected.
BH Lyn	08:22:36.11	+51:05:25.0	224.46	STIS	E140M	1425	Nova-like, white dwarf not detected.
V382 Vel	10:44:48.40	–52:25:31.1	227.66	STIS	E140M	1425	Classical nova, white dwarf not detected.
IP Peg	23:23:08.60	+18:24:59.6	227.82	FOS	G160L	2440	White dwarf not detected.
V842 Cen	14:35:52.58	–57:37:35.1	236.16	COS	G140L	1105	Old nova, white dwarf not detected.
RX J0153.3+7446	01:53:20.99	+74:46:22.3	236.38	STIS	G140L	1425	Magnetic, no time-resolved observations available.
V1776 Cyg	20:23:30.55	+46:31:29.8	237.22	STIS	G140L	1425	Nova-like, white dwarf not detected.
							but the white dwarf is not detected in the spectra.
SDSS J040714.78-064425.1	04:07:14.78	–06:44:25.2	245.04	COS	G140L	1105	Obtained after an outburst.
V405 Aur	05:57:59.29	+53:53:44.9	248.58	STIS	G140L	1425	Magnetic, time-resolved observations available but the white dwarf is not detected in the spectra.
RXJ1313.2-3259	13:13:17.11	–32:59:12.4	251.41	STIS	G140L	1425	Magnetic, time-resolved observations available but they do not cover the minimum.
CW Mon	06:36:54.59	+00:02:17.20	254.3	COS	G140L	1105	Obtained after an outburst.
U Gem	07:55:05.20	+22:00:04.40	254.74	FOS	G130H	1600	This work.
V405 Peg	23:09:49.10	+21:35:16.26	255.81	COS	G140L	1105	Obtained after an outburst.
HS2214	22:16:31.15	+29:00:19.82	258.02	COS	G140L	1105	Obtained after an outburst.
BD Pav	18:43:11.96	–57:30:45.26	258.19	STIS	G140L	1425	Evolved donor.
				COS	G140L	1105	
SS Aur	06:13:22.44	+47:44:24.97	263.23	STIS	G140L	1425	This work.
HM Leo	09:38:36.99	+07:14:54.61	267.71	COS	G140L	1105	Obtained after an outburst.
SDSS J100658.41+233724.4	10:06:58.42	+23:37:24.6	267.72	COS	G140L	1105	Obtained after an outburst.
V416 Dra	18:57:20.36	+71:31:18.8	272.32	STIS	G140L	1425	Magnetic, no time-resolved observations available.

Table E1 – continued from previous page

System	α	δ	Period (min)	Instrument	Grating	Central wavelength	Comment
DQ Her	18:07:30.26	+45:51:32.4	278.81	FOS	G130H G160L	1600 2440	Magnetic, time-resolved observations available but the white dwarf is not detected in the spectra.
IX Vel	08:15:18.97	–49:13:20.7	279.25	STIS	E140M	1425	Nova-like, white dwarf not detected.
MU Cam	06:25:16.26	+73:34:39.1	283.17	STIS	G140L	1425	Magnetic, no time-resolved observations available.
UX UMa	13:36:40.96	+51:54:49.5	283.21	STIS	E140M	1425	Nova-like, white dwarf not detected.
AY Sex	10:23:47.68	+00:38:41.3	285.26	COS	G140L	1105	Evolved donor.
V895 Cen	14:29:27.20	–38:04:09.6	285.92	STIS	G140L	1425	Magnetic, no time-resolved observations available.
FO Aqr	22:17:55.38	–08:21:03.8	290.97	FOS	G160L	2440	Magnetic, no time-resolved observations available.
T Aur	05:31:59.13	+30:26:45.5	294.3	STIS	G140L	1425	White dwarf not detected.
V825 Her	17:18:37.02	+41:15:50.9	296.64	STIS	E140M	1425	Classical nova, white dwarf not detected.
V446 Her	18:57:21.60	+13:14:29.0	298.08	STIS	G140L	1425	Classical nova, white dwarf not detected.
V3885 Sgr	19:47:40.53	–42:00:26.4	298.31	STIS FOS	E140M G160L	1425 2440	Nova-like, white dwarf not detected.
1SWASP J162117.36+441254.2	16:21:17.36	+44:12:54.1	299.31	COS	G140L	1105	Evolved donor.
RX And	01:04:35.54	+41:17:57.42	302.25	GHRS	G140L G140L G140L	1425 1425 1425	This work. Obtained in 1997 after an outburst. Obtained in 1997 after an outburst.
EX Dra	18:04:14.11	+67:54:12.2	302.31	FOS	G160L	2440	Obtained in outburst.
PQ Gem	07:51:17.33	+14:44:23.9	311.56	FOS	G160L	2440	Magnetic, time-resolved observations available but the white dwarf is not detected in the spectra.
V0709 Cas	00:28:48.80	+59:17:22.2	319.97	STIS	G140L	1425	Magnetic, time-resolved observations available but the white dwarf is not detected in the spectra.
RW Tri	02:25:36.16	+28:05:50.9	333.91	STIS	G140L	1425	Nova-like, white dwarf not detected.
V347 Pup	06:10:33.66	–48:44:25.4	333.99	FOS	G130H	1600	Nova-like, white dwarf not detected.
VY Scl	23:29:00.48	–29:46:45.9	334.08	STIS	G140L	1425	Nova-like, white dwarf not detected.
RW Sex	10:19:56.62	–08:41:56.1	353.01	GGHRS STIS	G140L E140M	1425 1425	Nova-like, white dwarf not detected.
SDSS J154453.60+255348.8	15:44:53.61	+25:53:48.9	361.85	COS	G140L	1105	No valid data.
TZ Per	02:13:50.96	+58:22:52.3	378.58	STIS	G140L	1425	Obtained in outburst.
TT Crt	11:34:47.26	–11:45:31.0	386.52	STIS	G140L	1425	Obtained after an outburst.
LY UMa	10:48:18.01	+52:18:29.8	390.64	STIS	G140L	1425	White dwarf not detected.
SS Cyg	21:42:42.79	+43:35:09.9	396.19	GHRS	G140L	1425	Obtained during or close to an outburst.
EM Cyg	19:38:40.11	+30:30:28.4	418.91	STIS	G140L	1425	White dwarf not detected.
V959 Mon	06:39:38.60	+05:53:53.0	426.96	STIS	E140M	1425	Classical nova, white dwarf not detected.
HS 0218+3229	02:21:33.48	+32:43:23.8	428.01	COS	G140L	1105	Evolved donor.
AF Cam	03:32:15.48	+58:47:22.1	466.67	STIS	G140L	1425	White dwarf not detected.
V1309 Ori	05:15:41.41	+01:04:40.5	478.96	FOS	G160L	2440	Magnetic, time-resolved observations available but the white dwarf is not detected in the spectra.
HS1055	10:57:56.29	+09:23:14.87	541.88	COS	G140L	1105	Obtained after an outburst.
AE Aqr	20:40:09.16	–00:52:15.1	592.78	FOS	G160L	2440	Evolved donor. Magnetic, time-resolved observations but the white dwarf is not detected in the spectra.
EY Cyg	19:54:36.71	+32:21:55.1	661.43	STIS	G140L	1425	Evolved donor.
V442 Cen	11:24:51.87	–35:54:36.69	662.4	STIS	G140L	1425	This work.
NGC 6397-CV1	17:40:41.6	–53:40:19	678.53	FOS	G160L	2440	White dwarf not detected.

Table E1 – continued from previous page

System	α	δ	Period (min)	Instrument	Grating	Central wavelength	Comment
IGR J17014-4306	17:01:28.15	–43:06:12.2	768.97	COS	G140L	1105	Magnetic, time-resolved observations available but the white dwarf is not detected in the spectra.
DI Lac	22:35:48.58	+52:42:59.5	783.03	STIS	E140M	1425	Old nova.
CI Aql	18:52:03.59	–01:28:39.3	890.44	COS	G140L	1105	Recurrent nova, white dwarf not detected.
QR And	00:19:49.93	+21:56:52.1	951.05	STIS	E140M	1425	Super-Soft X-ray source.
U Sco	16:22:30.78	–17:52:42.8	1772.0	STIS	G140L	1425	Recurrent nova.
NOVA LMC 2000	05:25:01.60	–70:14:17.3	–	STIS	E140M	1425	Classical nova, white dwarf not detected.
V339 Del	20:23:30.68	+20:46:03.8	–	STIS	E140M	1425	Classical nova, white dwarf not detected.
QU Car	11:05:42.48	–68:37:58.3	–	STIS	E140M	1425	Nova-like, white dwarf not detected.
M31N 2008-12a	00:45:28.81	+41:54:09.9	–	STIS	G140L	1425	Classical nova, white dwarf not detected.
SDSS J074716.81+424849.0	07:47:16.80	+42:48:49.0	–	STIS	G140L	1425	Nova-like, white dwarf not detected.
V1369 Cen	13:54:45.35	–59:09:04.2	–	STIS	E140M	1425	Classical nova, white dwarf not detected.
V5668 Sgr	18:36:56.83	–28:55:40.0	–	STIS	E140M	1425	Classical nova, white dwarf not detected.
NOVA LMC 2012	04:54:56.84	–70:26:56.1	–	STIS	E140M	1425	Classical nova, white dwarf not detected.

This paper has been typeset from a TEX/LATEX file prepared by the author.